OPTIMIZATION OF COMPOSITE TUBES FOR A THERMAL OPTICAL LENS HOUSING DESIGN

A Thesis

by

HECTOR CAMERINO GARCIA GONZALEZ

Submitted to the Office of Graduate Studies of
Texas A&M University
in partial fulfillment of the requirements for the degree of

MASTER OF SCIENCE

August 2003

Major Subject: Aerospace Engineering

OPTIMIZATION OF COMPOSITE TUBES FOR A THERMAL OPTICAL LENS HOUSING DESIGN

A Thesis

by

HECTOR CAMERINO GARCIA GONZALEZ

Submitted to Texas A&M University
in partial fulfillment of the requirements
for the degree of

MASTER OF SCIENCE

Approved as to style and content by:

Thomas C. Pollock (Chair of Committee)	Dimitris C. Lagoudas (Member)
Ozden O. Ochoa (Member)	Walter E. Haisler (Head of Department)

August 2003

Major Subject: Aerospace Engineering

ABSTRACT

Optimization of Composite Tubes
for a Thermal Optical Lens Housing Design. (August 2003)
Hector Camerino Garcia Gonzalez, B.S., Instituto Politecnico Nacional
Chair of Advisory Committee: Dr. Thomas C. Pollock

This thesis describes the manufacturing, structural analysis and testing of a composite cylinder for space application. This work includes the design and fabrication of a reusable multicomponent mandrel made of aluminum and steel and the manufacturing of a carbon fiber reinforced tube in an epoxy resin matrix. This structure intends to serve as the optical lens housing onboard a spacecraft. In addition, some future work needs to be done before this component is certified.

The objective is to determine if the composite meets the stiffness and strength requirements for lens housing.

The structural analysis is made by means of a finite element model simulating the true boundary conditions and applied loads. The testing includes the design of a fixture to allow the composite cylinder to be mounted in one of the testing machines at the Department of Aerospace Engineering at Texas A&M University and the preparation for the actual test.

The response to the experimental analysis will be compared to the numerical simulation (Finite Element Model) to verify the results.

To my parents and my sister

TABLE OF CONTENTS

CHAPTER Page

Page

LIST OF TABLES

TABLE Page

LIST OF FIGURES

FIGURE Page

FIGURE Page

FIGURE Page

FIGURE Page

CHAPTER I

INTRODUCTION

A. Overview

One method of determining spacecraft attitude involves the use of star sensing cameras commonly called star trackers. Next generation trackers will have a mass of less than one Kg and will occupy a volume of less than 2000 cm^3. In general, any housing for optical devices onboard of a space vehicle must meet strict requirements such as dimensional stability, stiffness, strength, natural frequencies, etc. The success of the optical devices (acquisition of data) depends on the structural characteristics of the housing among some other factors.

The use of composite materials in the aerospace industry has increased during the last two decades giving as a result a large variety of components made of composites. The principal reason that composite have not been used extensively in the structure of star trackers is cost. The purpose of this investigation is to determine the suitability of low cost wet layups in the fabrication of highly precise optical components.

Specifically, this study investigates numerically and experimentally the application of the carbon-epoxy system to the manufacturing of composite tubes for an optical lens housing. The tube is a thin walled right circular cylinder with reinforced ends.

In the following chapters after a review of recent literature relevant to the problem of study, finite element models and the manufacturing of the test specimens will be described. Next the results of experiments and the numerical results will be presented and conclusions drawn.

The journal model is *IEEE Transactions on Automatic Control.*

B. Objectives

One objective is to determine the best lay-up and stacking sequence of a carbon/epoxy tube subjected to boundary and loading conditions simulating the maximum of a lens housing structure. This will be done by means of experimental testing and numerical simulation which will help to determine the influence of the different lay-ups on the bending behavior of the tubes. In order to perform the experimental part, it will be necessary to design and manufacture the tooling to build the test specimens and to test them. Therefore this project includes design and manufacturing of a reusable mold and manufacturing of the composite specimens for the actual test in addition to the design and manufacturing of the fixture. Mechanical properties will be obtained by experimental testing and validated by the numerical finite element model (FEM). In addition, a closed form solution using the laminated plate approach for determining the overall bending stiffness of the composite tube will be included.

A second objective is to demonstrate the repeatability of the manufacturing process by preparing and testing several tubes of identical layup and procedure.

C. Literature review

The review begins with a discussion of past studies of composite laminated shells in bending. The motivation of this search is to identify the appropriate tools to validate the results of the numerical model and the experiments.

Over the past several years there have been a number of theoretical formulations which provide a closed form or semi-analytical solution to the problem of composite laminated shells.

Laminated cylindrical shells are often modeled as equivalent single layer shells using classical shell theory [1] in which straight lines normal to the undeformed middle

surface remain straight, inextensible and normal to the deformed middle surface. Transverse normal strains are assumed to be zero and transverse shear deformations are neglected.

This classical assumption of non-deformable normals has to be abandoned for accurate analysis of laminated shell structures. Refinements to Love's first approximation theory of thin elastic shells [1] are meaningless unless the effects of transverse shear and normal stresses are taken into account in a refined theory [2].

Exact elasticity solutions for bending of laminated plates obtained by Pagano [3], have made possible the quantification of errors involved in the classical plate theory and assessment of the accuracy of refined plate theories. Such exact solutions for bending of laminated circular cylindrical shells are not available.

The effects of transverse shear and normal stresses in shells were considered by several authors. Exact solutions of the three dimensional equations and approximate solutions using a piecewise variation of the displacements through the thickness were presented by Srinivas [4], where significant discrepancies were found between the exact solution and the classical shell theory solutions. Barbero et al [2], made a generalization of the shear deformation theories of laminated composite shells. The theory is based on the idea that the thickness approximation of the displacement field can be accomplished via a piecewise approximation through each individual lamina. The use of polynomial expansion with compact support (i.e. finite element approximation) through the thickness proved to be convenient. The theory gives very good results for deflections, stresses and natural frequencies.

Ren [5] presented exact solutions for cross-ply laminated cylindrical shells in cylindrical bending undergoing plane strain. He compared these results with the analogous results from classical shell theory and Donnell shell theory. From this comparison he found that the classical shell theory leads to a very poor description

of a laminated shell at low curvature radius-to-depth ratios, but it converges to the exact solution as this ratio increases. He found also that Donnell shell theory does not converge to the exact solution as the ratio increases.

Varadan and Bhaskar [6], presented solutions based on three-dimensional elasticity for finite length, cross-ply cylindrical shells, simply supported at both ends and subjected to transverse sinusoidal loading using the method applied by Srinivas, who addressed the free vibration problem of simply supported shells. By assuming suitable displacement functions, the boundary value problem is reduced to a set of coupled ordinary differential equations and then solved by the method of Frobenius. They presented displacements and stresses for [90], [90/0], [90/0/90], $[90/0/90/0/90]_s$ shells. The deviations from laminated plate theory were also described. This method has shown to give results identical to those of a stress function approach for a plane strain problem.

The stress function approach introduced by Lekhnitskii [7] has been extended to layered cylinders by Jolicoeur and Cardou[8]; Chouchaoui and Ochoa [9]. Here the solution is straightforward, but due to the layered treatment, the problem consists in dealing with a very large system of equations for the undetermined constants in the stress and displacement expressions.

Chouchaoui and Ochoa [9] developed a general analytical model for the stresses and displacements of an assembly of several coaxial laminated hollow circular cylinders made of orthotropic layers, and subjected to internal and external pressure, tensile, torsion and bending loads and they compared the results to the experimental tensile test of a composite tube. Displacements and stresses were evaluated for different angle-ply layers and radius-to-thickness ratios. The cross-section of the assembly of n coaxial hollow circular cylinders is shown in Figure 1.

Studies like the ones above have been based on the Lekhnitskii [7] stress function

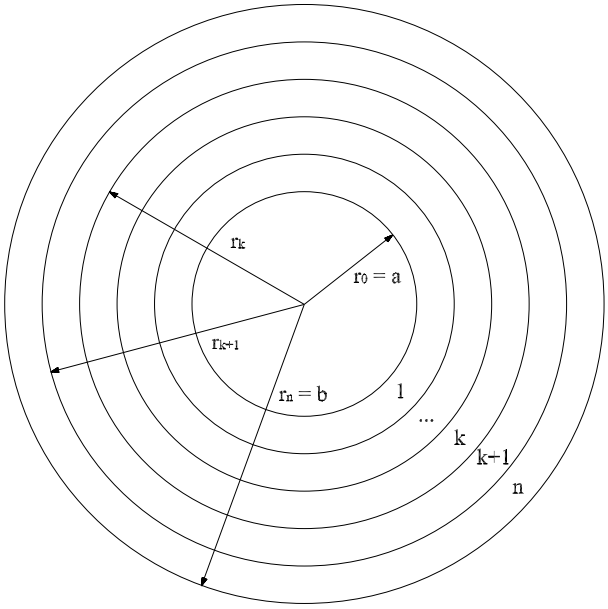

Fig. 1. Coaxial tubes

approach, but while the stresses can be determined from the stress functions by differentiation in Lekhnitskii's formalism, the displacements cannot be expressed by the stress functions in simple terms. In this way the formalism is not effective for problems of laminates in which the interfacial continuity requires the displacement and the tractions to be continuous.

The displacement approach could be used by deriving the governing equations in terms of displacements and look for the solution, but the stress expressions in terms of displacements become very complicated. For the study of a multi-layered system, one has to deal with a large system of equations leading to unwieldy stress expressions.

Because of the drawbacks of using the stress or the displacement alone as the primary variables it would be convenient to formulate the problem in a way in which the stresses as well as the displacements are the state variables. Then it is recommended to develop a state space approach for the case of multi-layered cylindrically

anisotropic tubes subjected to tractions that do not vary axially [10].

When a state space formulation is used it must express the field equations in a state equation in which the unknown is the state vector. Usually the displacements u_r, u_θ, u_z and the transverse stresses σ_r, σ_{rz}, $\sigma_{r\theta}$ are taken as the primary state variables for laminated tubes.

The field equations in cylindrical coordinates are more complicated than those in Cartesian coordinates, and if some arrangements are not made, the system matrix is r dependent, and then the state equation becomes unsolvable by means of matrix algebra. To resolve this problem, Tarn and Wang [10] suggested using $r\sigma_r$, $r\sigma_{rz}$, and $r\sigma_{r\theta}$ instead of σ_r, σ_{rz}, $\sigma_{r\theta}$ as the stress variables and cast the field equations into a first order matrix equation with respect to r. This system is independent of r so it is possible to determine the solution for a laminated tube using methods of matrix algebra and the transfer matrix. A transfer matrix transmits the state variable vector from the inner surface to the outer surface and takes into account the interfacial continuity and lateral boundary conditions in a simpler way.

Chan and Demirhan [11], presented recently a new approach based upon laminate plate theory to calculate the bending stiffness of fiber reinforced composite tubes. This closed form solution will be used in this study to validate the numerical and experimental results.

1. Bending stiffness closed-form solution

Accurate evaluation of bending stiffness is important for better prediction of deflection, buckling load and vibration response of structures. Two approaches based on a closed-form analytical solution for overall bending stiffness of a composite tube are presented.

a. Smear property approach

The overall bending stiffness of composite tubes can be obtained by using the smeared modulus of the laminated tube and multiplying the moment of inertia of the tube [11]:

$$EI = \frac{1}{4} E_x \pi \left({R_o}^4 - {R_i}^4 \right) \tag{1.1}$$

where E_x is the smeared modulus of the tube laminate and is obtained from lamination theory [12].

The strain-stress relations in terms of engineering constants are obtained as:

$$\begin{bmatrix} \epsilon_x \\ \epsilon_y \\ \gamma_s \end{bmatrix} = \begin{bmatrix} \frac{1}{E_x} & -\frac{\nu_{yx}}{E_y} & \frac{\eta_{sx}}{G_{xy}} \\ \frac{-\nu_{xy}}{E_x} & \frac{1}{E_y} & \frac{\eta_{sy}}{G_{xy}} \\ \frac{\eta_{xs}}{E_x} & \frac{\eta_{ys}}{E_y} & \frac{1}{G_{xy}} \end{bmatrix} \begin{bmatrix} \sigma_x \\ \sigma_y \\ \tau_s \end{bmatrix} \tag{1.2}$$

where:

E_x, E_y are the Young's moduli of a single lamina in the x- and y- directions respectively,

ν_{xy},ν_{yx} are the lamina Poison's ratios,

G_{xy} is the lamina shear modulus referred to the x- and y- axes, and

η_{xs},η_{ys},η_{sx},η_{sy} are the lamina shear coupling coefficients

The reference plane strains are related to the in-plane forces as follows:

$$\begin{bmatrix} \epsilon_x^0 \\ \epsilon_y^0 \\ \gamma_s^0 \end{bmatrix} = \begin{bmatrix} a_{xx} & a_{xy} & a_{xs} \\ a_{yx} & a_{yy} & a_{ys} \\ a_{sx} & a_{sy} & a_{ss} \end{bmatrix} \begin{bmatrix} N_x \\ N_y \\ N_s \end{bmatrix} \tag{1.3}$$

or, in brief,

$$[\epsilon^\circ] = [a][N] \tag{1.4}$$

where $[a]$ is the extensional laminate compliance matrix, which is the inverse of

the corresponding stiffness matrix $[A]$.

$$[a] = [A]^{-1} \tag{1.5}$$

Equation 1.3 can be written in terms of engineering constants by replacing the lamina constants in equation 1.2 with corresponding laminate moduli and noting that the average laminate stresses are:

$$\begin{bmatrix} \bar{\sigma}_x \\ \bar{\sigma}_y \\ \bar{\tau}_s \end{bmatrix} = \begin{bmatrix} N_x \\ N_y \\ N_s \end{bmatrix} \frac{1}{h} \tag{1.6}$$

Thus the strain-force relations for the laminate are written in terms of engineering constants as follows:

$$\begin{bmatrix} \epsilon_x^0 \\ \epsilon_y^0 \\ \gamma_s^0 \end{bmatrix} = \begin{bmatrix} \frac{1}{\bar{E}_x} & -\frac{\bar{\nu}_{yx}}{\bar{E}_y} & \frac{\bar{\eta}_{sx}}{\bar{G}_{xy}} \\ \frac{-\bar{\nu}_{xy}}{\bar{E}_x} & \frac{1}{\bar{E}_y} & \frac{\bar{\eta}_{sy}}{\bar{G}_{xy}} \\ \frac{\bar{\eta}_{xs}}{\bar{E}_x} & \frac{\bar{\eta}_{ys}}{\bar{E}_y} & \frac{1}{\bar{G}_{xy}} \end{bmatrix} \begin{bmatrix} N_x \\ N_y \\ N_s \end{bmatrix} \frac{1}{h} \tag{1.7}$$

where:

$\bar{E}_x$,$\bar{E}_y$ are the laminate effective Young's moduli in the x- and y- directions respectively,

$\bar{G}_{xy}$ is the laminate effective shear modulus,

$\bar{\nu}_{xy}$,$\bar{\nu}_{yx}$ are the laminate effective Poisson's ratios, and

$\bar{\eta}_{xs}$,$\bar{\eta}_{ys}$,$\bar{\eta}_{sx}$,$\bar{\eta}_{sy}$ are the laminated effective shear coupling coefficients.

By equating correspondent terms in the compliance matrices of equations 1.3 and 1.7, we obtain the following relation for $\bar{E}_x$

$$\bar{E}_x = \frac{1}{h a_{xx}} \tag{1.8}$$

where a_{xx} is defined as the $[1,1]$ term of the extensional laminate compliance matrix $[a]$.

b. Laminated plate approach

For the laminated plate approach, an infinitesimal plate section of the laminated tube is considered as shown in Figure 2. The infinitesimal section that inclines an angle θ with respect to the axis of the composite tube z'-axis, is rotated about the x-axis to the position parallel to the y'-axis. The stiffness of the plate calculated by lamination theory is translated to the axis y' according to the parallel axes theorem [13]. The overall stiffness of the tube is obtained by integrating over the entire θ domain.

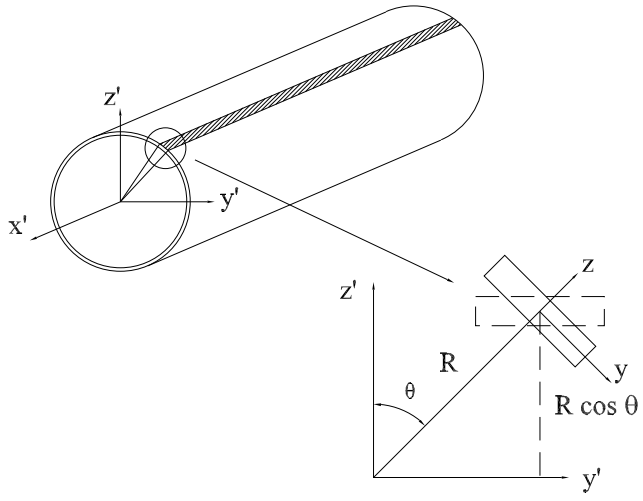

Fig. 2. Plate section of composite tube laminate

The overall stiffness matrices, $[\bar{A}]$, $[\bar{B}]$ and $[\bar{D}]$ of the tube can be expressed as:

$$[\bar{A}] = \int_0^{2\pi} [A'] R \mathrm{d}\theta \tag{1.9}$$

$$[\bar{B}] = \int_0^{2\pi} [B'] R \mathrm{d}\theta \tag{1.10}$$

$$[\bar{D}] = \int_0^{2\pi} [D'] R \mathrm{d}\theta \tag{1.11}$$

where:

$$\begin{aligned} [A'] &= [A] \\ [B'] &= [B] + R\,cos\,\theta[A] \\ [D'] &= [D] + 2\,R\,cos\,\theta[B] + (R\,cos\,\theta)^2[A] \end{aligned} \tag{1.12}$$

The universal [A], [B] and [D] matrices are the stiffness matrices per unit section of the composite plate with respect to the x-y-z coordinate system as shown in Figure 2.

Universal [A], [B] and [D] matrices [12] are defined as:

$$A_{ij} = \sum_{k=1}^{n} Q_{ij}^k \left(h_k - h_{k-1}\right) \tag{1.13}$$

$$B_{ij} = \frac{1}{2} \sum_{k=1}^{n} Q_{ij}^k \left(h_k^2 - h_{k-1}^2\right) \tag{1.14}$$

$$D_{ij} = \frac{1}{3} \sum_{k=1}^{n} Q_{ij}^k \left(h_k^3 - h_{k-1}^3\right) \tag{1.15}$$

where

A_{ij} are extensional stiffnesses, or in-plane laminate moduli, relating in-plane loads to in-plain strains.

B_{ij} are coupling stiffnesses, or in-plane/flexure coupling laminate moduli, relating

in-plane loads to curvatures and moments to in-plane strains. If $B_{ij} \neq 0$, in-plane forces produce flexural and twisting deformations; moments produce extension of the middle surface in addition to flexure and twisting.

D_{ij} are bending or flexural laminate stiffnesses relating moments to curvatures.

Q_{ij} are the reduced stiffness matrix components given by:

$$Q_{ij} = C_{ij} - \frac{C_{i3}C_{j3}}{C_{33}} \quad (i, j, = 1, 2, 6) \tag{1.16}$$

$$Q_{11} = \frac{E_1}{1 - \nu_{12}\,\nu_{21}} \tag{1.17}$$

$$Q_{22} = \frac{E_2}{1 - \nu_{12}\,\nu_{21}} \tag{1.18}$$

$$Q_{12} = \frac{\nu_{12}\,E_2}{1 - \nu_{12}\,\nu_{21}} \tag{1.19}$$

$$Q_{66} = G_{12} \tag{1.20}$$

C_{ij} are the components of the stiffness matrix, and in terms of engineering constants can be expressed as shown in appendix D.

Substituting equation 1.12 into equations 1.9, 1.10 and 1.11 and rearranging, the expressions for calculating the total extensional, coupling and bending stiffness matrices are obtained:

$$\bar{A}_{ij} = \int_0^{2\pi} \left(\sum_{k=1}^{n} \hat{Q}_{ij}^k (z_k - z_{k-1}) \right) R\,\mathrm{d}\theta = R \sum_{k=1}^{n} \left(\int_0^{2\pi} \hat{Q}_{ij}^k\,\mathrm{d}\theta \right) (z_k - z_{k-1}) \tag{1.21}$$

$$\bar{B}_{ij} = \frac{R}{2} \sum_{k=1}^{n} \left(\int_0^{2\pi} \hat{Q}_{ij}^k\,\mathrm{d}\theta \right) \left(z_k^2 - z_{k-1}^2 \right) \tag{1.22}$$

$$\bar{D}_{ij} = \frac{R}{3}\sum_{k=1}^{n}\left(\int_0^{2\pi}\hat{Q}_{ij}^k\,\mathrm{d}\theta\right)\left(z_k^3 - z_{k-1}^3\right) + R^3\sum_{k=1}^{n}\left(\int_0^{2\pi}\hat{Q}_{ij}^k\,cos^2\,\theta\,\mathrm{d}\theta\right)(z_k - z_{k-1}) \tag{1.23}$$

$\hat{Q}_{ij}^k$ is a function of rotation angle about x-axis θ, fiber orientation angle β, and the elastic material constants as shown in the next equations:

$$\begin{aligned}
\hat{Q}_{11} &= c_z^4 Q_{11} + 2s_z^2c_z^2(c_x^2Q_{12} + 2c_x^2Q_{66}) + s_z^4c_x^4Q_{22}\\
\hat{Q}_{12} &= s_z^2c_z^2(Q_{11} + c_x^4Q_{22} - 4c_x^2Q_{66}) + (s_z^4 + c_z^4)c_x^2Q_{12}\\
\hat{Q}_{22} &= s_z^4Q_{11} + 2s_z^2c_z^2(c_x^2Q_{12} + 2c_x^2Q_{66}) + c_z^4c_x^4Q_{22}\\
\hat{Q}_{16} &= s_zc_z^3(Q_{11} - c_x^2Q_{12} - 2c_x^2Q_{66}) + s_z^3c_z(c_x^2Q_{12} - c_x^4Q_{22} + 2c_x^2Q_{66})\\
\hat{Q}_{26} &= s_z^3c_z(Q_{11} - c_x^2Q_{12} - 2c_x^2Q_{66}) + s_zc_z^3(c_x^2Q_{12} - c_x^4Q_{22} + 2c_x^2Q_{66})\\
\hat{Q}_{66} &= s_z^2c_z^2(Q_{11} + c_x^4Q_{22} - 2c_x^2Q_{12} - 2c_x^2Q_{66}) + (s_z^4 + c_z^4)c_x^2Q_{66}
\end{aligned} \tag{1.24}$$

where $s_z = \sin\beta$, $c_z = \cos\beta$, $s_x = \sin\theta$, and $c_x = \cos\theta$ and

E_1 and E_2 are Young's moduli in the 1- and 2-directions, respectively, G_{12} is shear modulus in 1-2 plane, ν_{12} the Poisson's ratio.

The effective bending stiffness of the composite tube can be expressed as:

$$D_x = \frac{1}{d_{11}} \tag{1.25}$$

where d_{11} is the [4,4] entry of the inverse of the $[\bar{A}\bar{B}\bar{D}]$ matrix.

c. Effective bending stiffness

To get the effective bending stiffness of any cylinder from the FEA result, the curvature due to the applied moment is required. The curvature of the deformed cylinder can be calculated from the displacements of any three points on the same axis along the z-direction. If we connect these three points by two lines and draw bisecting

lines through them, the center point of the curve can be found at the intersection. The distance from this point to any of the other three points gives the radius of curvature.

Finally, the load applied at the midspan is known, the corresponding moment can be calculated from:

$$M = \frac{\bar{E}_x I}{\rho} \tag{1.26}$$

where:

M is the bending moment at the midspan,

ρ is the radius of curvature of the tube, and

$\bar{E}_x$I is the effective bending stiffness of the tube.

In this way, the previous equation can be solved for $\bar{E}_x$I. The obtained value represents the effective bending stiffness from finite element and can be calculated for each of the configurations under study.

CHAPTER II

FINITE ELEMENT ANALYSIS

Numerical finite element models of the problem were created to perform a convergence study. The finite element analysis of the structure was performed using the commercial code FEMAP 8.1 as preprocessor and postprocessor and CAEFEM 7.1 as the solver.

The FE model consists of a multi-layered carbon-epoxy tube simply supported with a 20 lbs load applied at the midspan. This FE model reproduces the geometry of the test articles. Several models were generated according to the stacking sequences of the specimens tested ($[0/90]_4$, $[0/90]_3$, $[0/90]_2$, $[0/90/45/\text{-}45]_s$). The load configuration was chosen to simulate the bending of the cylinder due to the loads generated when used as a lens housing.

In the sections that follow, description of the model is given and the results of the cases are presented and discussed.

A. FE model

In this section, the model generation is described and a simplified problem of an isotropic tube in bending is compared to the closed form solution for displacement. A convergence study is performed to determine the number of elements required to provide convergence in displacements solutions.

1. Element selection

The element used for modeling the composite shell is the FEMAP laminate element. In general, shell elements are used to model structures where the in-plane dimensions are large compared to the thickness and where through the thickness

stresses are negligible. In this research the tube thickness for the eight layer composite is small enough to use the previous assumption. A short calculation shows this:

$$R_m = \frac{R_o + R_i}{2} = \frac{1.03 + 0.993}{2} = 1.0115in$$

and the laminate thickness

$$t = 0.037in$$

for that reason:

$$\frac{R_m}{t} = \frac{1.0115}{0.037} = 27.34$$

Shell elements are defined over the mid-plane surface of the tube where only one element is used through the thickness. If three-dimensional solid elements were used, multiple elements would be required through the thickness and this would depend upon the number of plies. In addition, in-plane and out-of-plane properties of the element must be specified. Because of the reduction in the number of nodes and elements when using shell elements, the complexity of the model is reduced. On the other hand, shell elements require only in-plane lamina material properties which are easy to find from literature or from known experimental data. The element coordinate system corresponding to this element is shown in Figure 3.

a. Laminate element properties

When modeling the composite tube, a material ID number, thickness and orientation angle for each layer or ply in the laminate are provided as input. The layers are specified relative to the material axes which were defined for the element. Because we did not specify a material orientation angle, these angles were set by FEMAP relative to the first edge of the element (edge from the first to the second node) as shown in

Figure 4.

The property selected is that of a 2D-orthotropic material which is commonly used for plane and some axisymmetric elements.

b. Orthotropic material formulation

The stress-strain relationship used is:

$$\begin{bmatrix} \epsilon_1 \\ \epsilon_2 \\ \epsilon_3 \\ \gamma_{12} \\ \gamma_{23} \\ \gamma_{13} \end{bmatrix} = \begin{bmatrix} \frac{1}{E_1} & -\frac{\nu_{21}}{E_2} & -\frac{\nu_{31}}{E_3} & 0 & 0 & 0 \\ -\frac{\nu_{12}}{E_1} & \frac{1}{E_2} & -\frac{\nu_{32}}{E_3} & 0 & 0 & 0 \\ -\frac{\nu_{13}}{E_1} & -\frac{\nu_{23}}{E_2} & \frac{1}{E_3} & 0 & 0 & 0 \\ 0 & 0 & 0 & \frac{1}{G_{12}} & 0 & 0 \\ 0 & 0 & 0 & 0 & \frac{1}{G_{23}} & 0 \\ 0 & 0 & 0 & 0 & 0 & \frac{1}{G_{13}} \end{bmatrix} \begin{bmatrix} \sigma_1 \\ \sigma_2 \\ \sigma_3 \\ \sigma_{12} \\ \sigma_{23} \\ \sigma_{13} \end{bmatrix} \tag{2.1}$$

2. Model generation

The method for modeling the composite tube in flexure is described in this section. The geometry and FE mesh are generated in FEMAP 8.1. Orientation and number of plies, lamina material properties and boundary and loading conditions are also applied inside the FEMAP 8.1 environment. In the manufacturing process, a bidirectional plain weave was utilized, but for purposes of modeling, each bidirectional layer was modeled as two unidirectional layers. In this way, the thickness of each layer is one half the one of the woven cloth plus the thickness added when the matrix is present. t_{woven}=0.007", t_{ply} = 0.0035" + thickness of matrix = 0.00462".

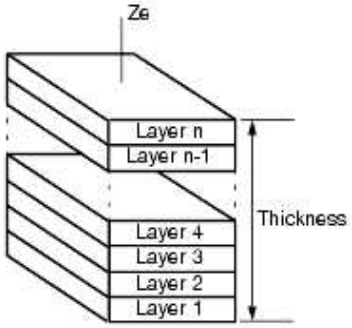

Fig. 3. FEMAP laminate element

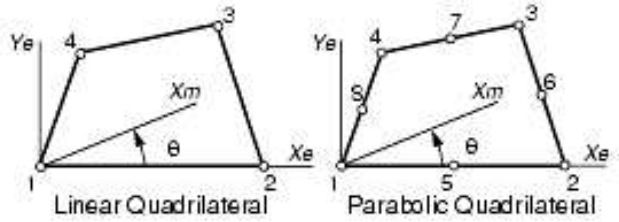

Fig. 4. FEMAP plane quadrilateral elements

a. Geometry and mesh creation

The model is composed of four elements. The carbon/epoxy tube, two aluminum end-caps which allow to support the specimen on a steel rod and an aluminum ring for load application. This geometry is chosen to closely simulate the structure and loading of the star tracker optical tube assembly. The mid-plane surface information was used to create laminated shells. The geometric construction process started with the definition of several working layers which contained the different items conforming the model. Five layers were created: cylinder, ring, end-caps, loads and constraints. The tube was constructed by creating a cylindrical surface in the layer cylinder. This cylindrical surface had a radius of 1.00923" and length of 9.0". The midplane radius corresponds to the average of inner and outer tube radii R_i and R_o respectively. This geometry is presented in Figure 5.

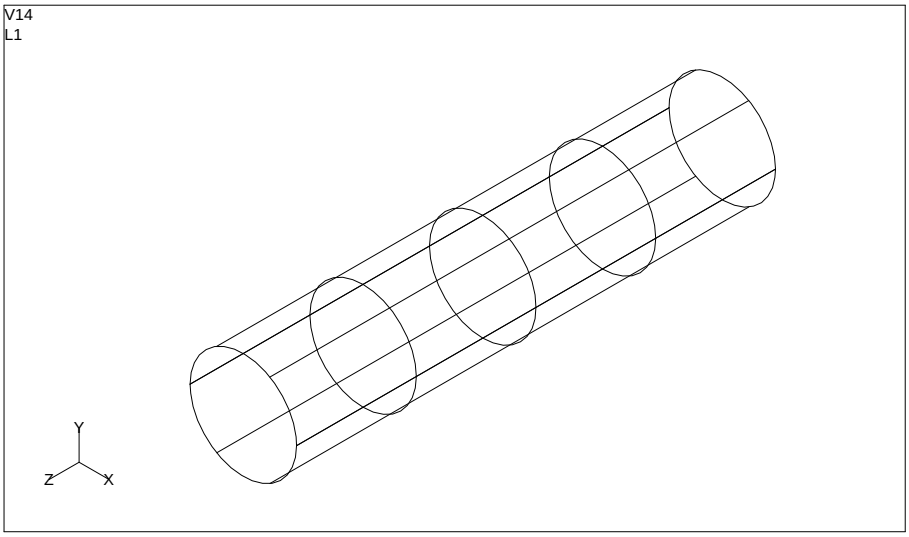

Fig. 5. Carbon/epoxy tube geometry

After the tube surface is created, the material and property are defined. The elastic constants corresponding to the carbon-epoxy system are calculated from the

properties of the constituents and are presented in Table III. The property selected for the cylinder is the 2-D orthotropic laminate, and at this stage, orientation and thickness of each layer are defined.

The carbon fiber properties are presented in Table I.

Table I. AS4 carbon fiber mechanical properties

Units	E_{1f}	E_{2f}	G_{12f}	ν_{12f}
Msi	32.488	2.030	2.030	0.2
GPa	224	14	14	0.2

The carbon/epoxy system mechanical properties were estimated using the rule of mixtures:

$$E_1 = V_f E_{1f} + V_m E_m \tag{2.2}$$

$$E_2 = \frac{E_{2f} E_m}{V_f E_m + V_m E_{2f}} \tag{2.3}$$

$$G_{12} = \frac{G_{12f} G_m}{V_f G_m + V_m G_{12f}} \tag{2.4}$$

Where:

E_{1f} = longitudinal modulus of the fiber

E_{1m} = longitudinal modulus of the matrix

E_1 = longitudinal modulus of the lamina

E_{2f} = transverse modulus of the fiber

E_{2m} = transverse modulus of the matrix

E_2 = transverse modulus of the lamina

G_{12f} = in-plane shear modulus of the fiber

G_{12m} = in-plane shear modulus of the matrix

G_{12} = in-plane shear modulus of the lamina

ν_{12f} = major Poisson's ratio of the fiber

ν_{12m} = major Poisson's ratio of the matrix

ν_{12} = major Poisson's ratio of the lamina

V_f=fiber volume ratio

V_m=matrix volume ratio

The carbon/epoxy mechanical properties were calculated assuming a fiber volume ratio of 0.50, a matrix volume ratio of 0.3, and a void volume ratio of 0.2. The void volume term includes both internal voids and surface roughness. The ply thickness used for each ply is 0.00462 in.

It will be shown later that this ply thickness gives a calculated weight of the composite which agrees with the measured weight of the manufactured specimens.

Table II contains the properties of the epoxy resin used for the manufacturing of the composite tubes and for the FEA model.

Table III contains the calculated mechanical properties for the lamina from constituents.

The number of elements around of the circumference forming the surface of the cylinder was initially chosen to be 20. The node spacing was set to equal and parametric. Along the longitudinal axis direction of the tube 45 elements were specified and the nodes were equally spaced. With the mesh/surface option the mesh in cylindrical coordinates was generated as seen in Figure 6.

The loading ring was generated as a 3-D isotropic solid in FEMAP 8.1. A rectangle and a circle were created. With the command extrude, a solid was generated

Table II. Physical properties of epoxy, Gougeon West 105/206

Mix ratio(by weight)	5.0:1
Pot life (100g @ 72F)	21.5 min%
Specific gravity of cured resin	1.18
Tensile modulus(psi)	4.60E5
Flexural modulus(psi)	4.50E5
Shear modulus(psi)	9.23E4
Poisson's ratio	0.24
Onset of Tg by DSC (F)	126
Ultimate Tg (F)	139
Coefficient of thermal expansion (x axis)	63.1
Coefficient of thermal expansion (y axis)	101

Table III. Carbon/Epoxy mechanical properties, as calculated using equations 2.2, 2.3 and 2.4

Units	E_1	E_2	G_{12}	ν_{12}
Msi	16.382	1.113	0.286	0.172
GPa	112.950	7.674	1.972	0.172

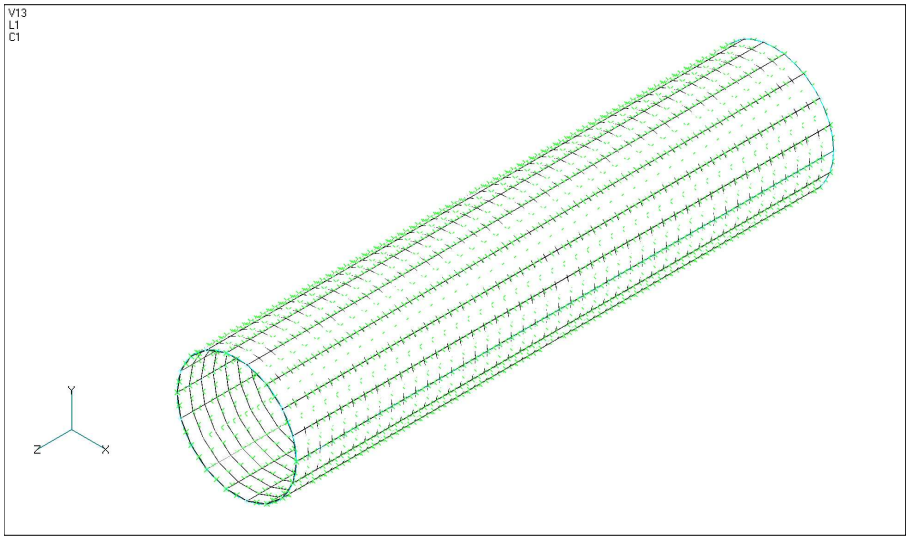

Fig. 6. Carbon/epoxy cylinder meshed

and the circular solid was subtracted from the rectangular solid. The material was chosen to be aluminum 6061. The mesh was controlled with mesh control/size along the cylindrical surface. In this case 20 elements were given to the eight longest edges of the solid square and 2 elements were given to the line defining the thickness dimension. The nodes forming the perimeter were uniformly spaced.

For the generation of the mesh of the ring, the number of elements on each curve forming the ring is defined, then by means of the -size on solid- option the -hexmesh- option was selected and finally the -mesh/geometry/hexmesh solids- command was applied. The resulting mesh is shown in Figure 7.

The aluminum end caps were created by extruding two pairs of circles located at the two ends of the tube. The same material and property used for the loading ring was chosen for the end caps. The end cap mesh is presented in Figure 9. Here the layer capability of the model allowed a view of the cylinder and the end caps at one time and a combination of all the items if required. This is shown in Figure 8.

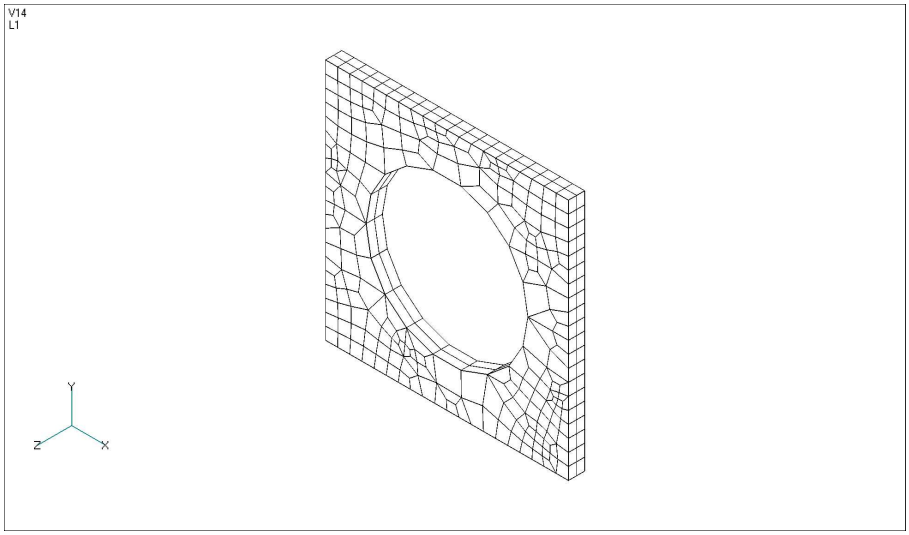

Fig. 7. Loading ring mesh

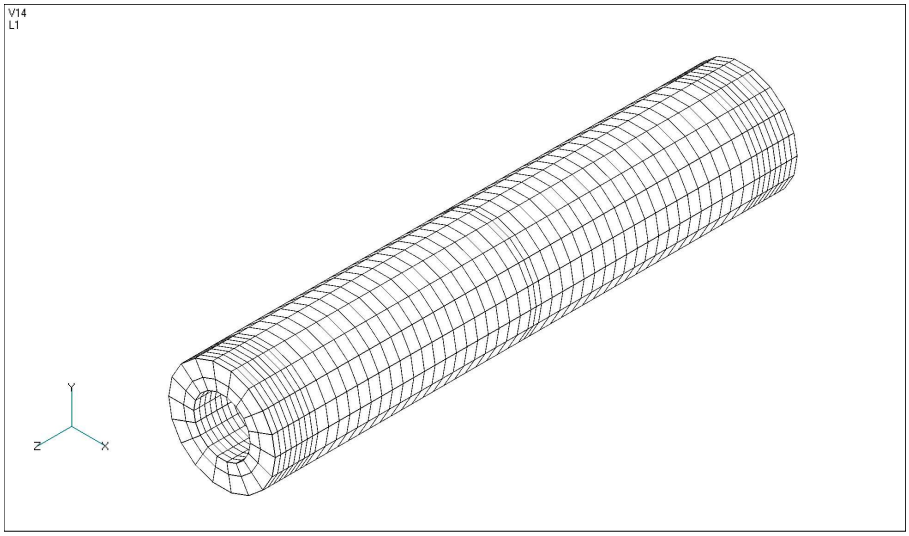

Fig. 8. Cylinder and end caps activated

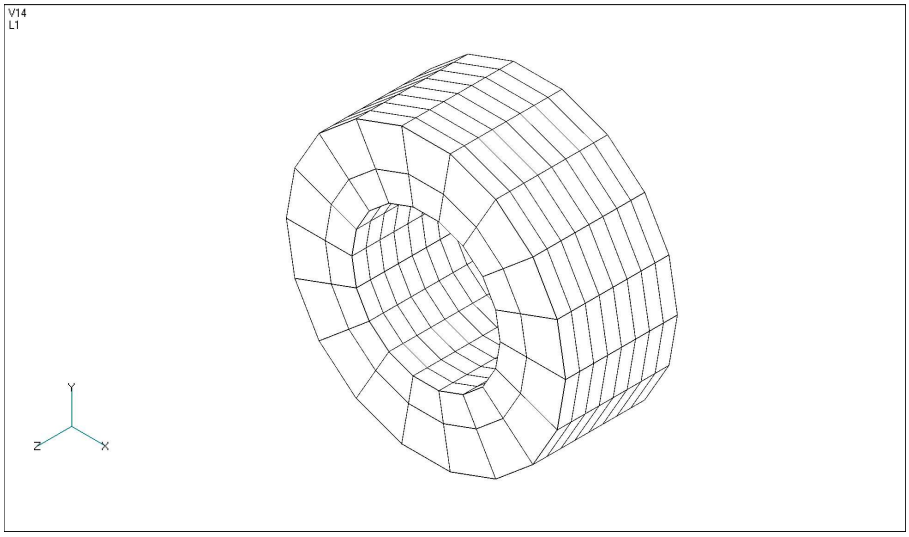

Fig. 9. End cap mesh

The properties of the aluminum used for the ring and end caps are presented in Table IV.

Table IV. 6061-T6 Aluminum mechanical properties, www.matweb.com

Units	E_1	G_{12}	ν_{12}
Msi	10	3.77	0.33
GPa	69	26	0.33

After adding the loading ring to the model it was seen that a refinement in the mesh had to be done around the circumference of the tube in the place where it touches the ring, then by using the split mesh command the mesh of the cylinder was modified as shown in Figure 10.

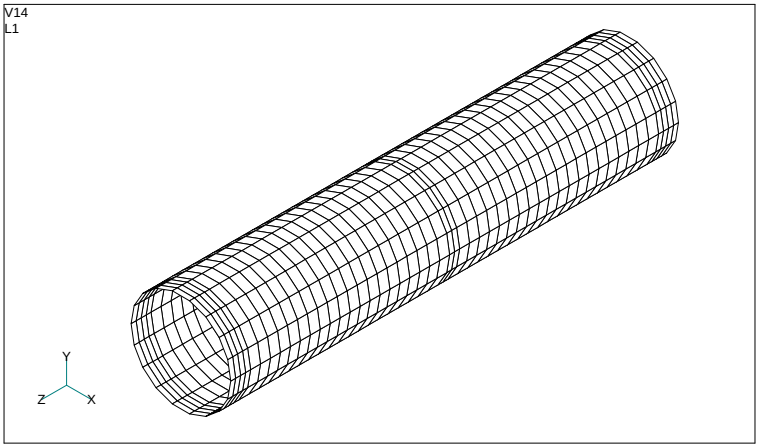

Fig. 10. Composite tube refined mesh

b. Boundary and loading conditions

The test articles and model geometry simulate the response of two lens assemblies acting as a beam with fixed/free boundary condition, as seen in Figure 11. To maintain the symmetry of the load frame and for ease of applying the load, the three point bend geometry was used. The experimental flexure scenario is shown in Figure 12

The ends of the tube were free to rotate in R_x, R_y, R_z and to translate in u_z (T_z). In the experiments this was done by means of two plain spherical bearings located inside the end-caps which allow for R_x, R_y and R_z rotations and u_z (T_z) translation of the specimen as deflection increases, simulating the free boundary condition. These bearings were modeled in the FEA by applying restrictions in $u_x(T_x)$ and u_y (T_y) at two nodes located on the internal face of the end-caps and lying on the xz plane as shown in Figure 13.

On the other hand, certain nodes at the top face of the loading ring were restricted in u_z (T_z), R_x, R_y, and R_z on its top surface. These constraints on the experimental

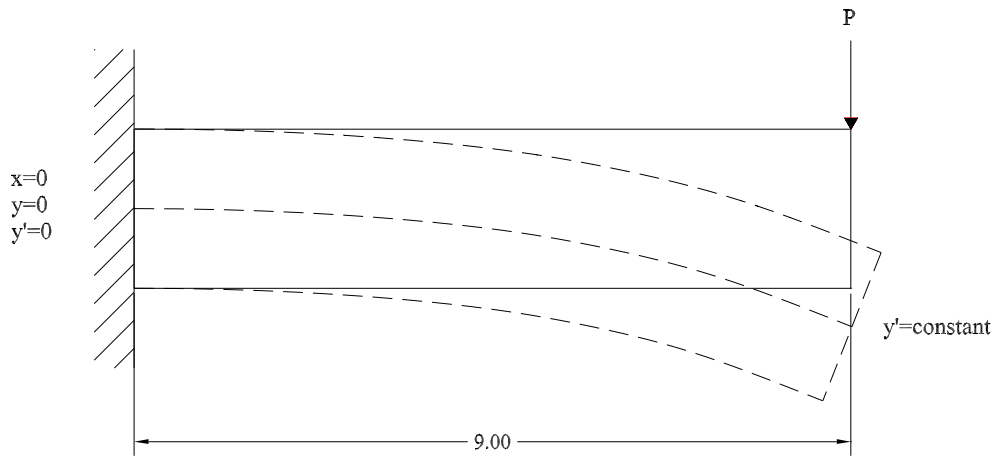

Fig. 11. The desired boundary conditions above, were obtained by doubling the length of the tube, applying the load to the center, and allowing rotation at both ends

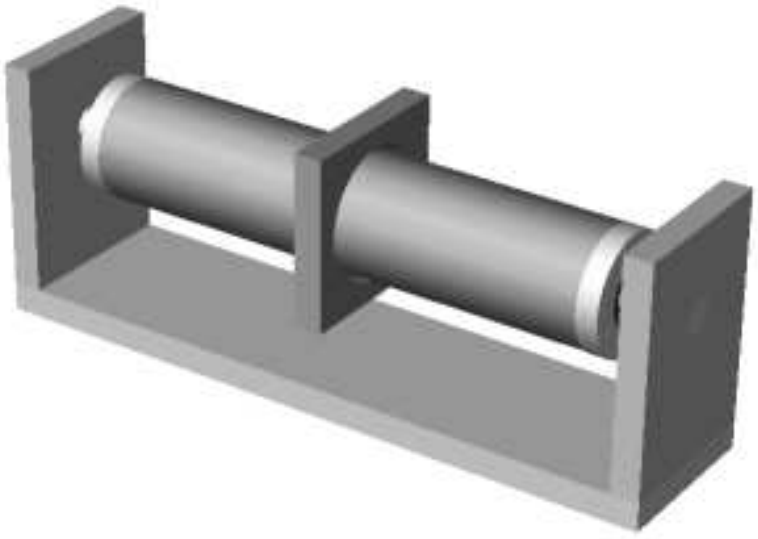

Fig. 12. Experimental fixture

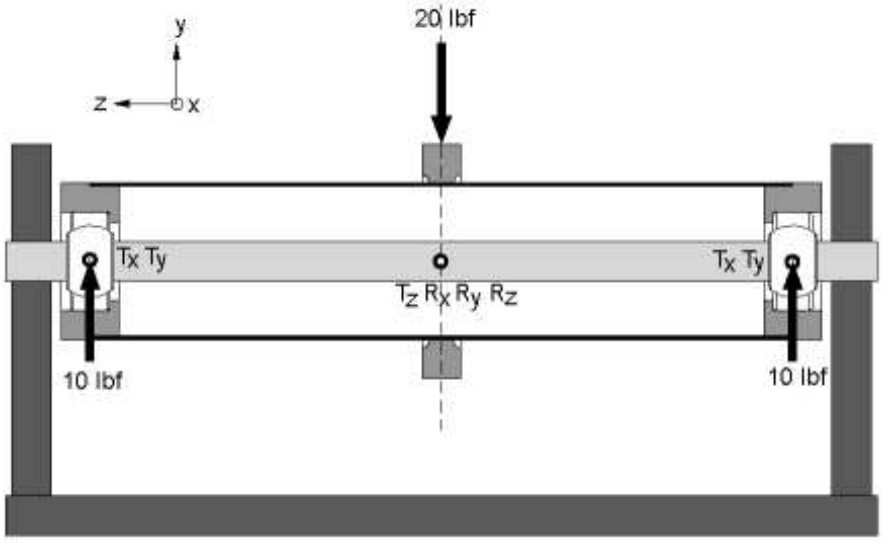

Fig. 13. Boundary conditions

geometry and on the FEA model are presented in Figures 13 and 14.

By means of the fixture used, the actual support conditions are simplified by taking a simply supported cylinder and adding the loading ring to the model to apply a bending load. This system will produce a zero slope at the midspan of the tube substituting the zero slope at the fixed end of a cantilever cylinder. We are modeling two cylinders by applying two times a load P = 10 lbs.

3. Convergence study

A convergence study was conducted to determine the number of elements necessary to model the composite tube in flexure. The study was based on the $[0/90]_4$ carbon-epoxy lay-up.

Several mesh sizes were investigated to determine the most suitable according to computational effort and time in model construction. 18, 28 and 36 elements were used around the circumference of the cylinder and the number of elements along the

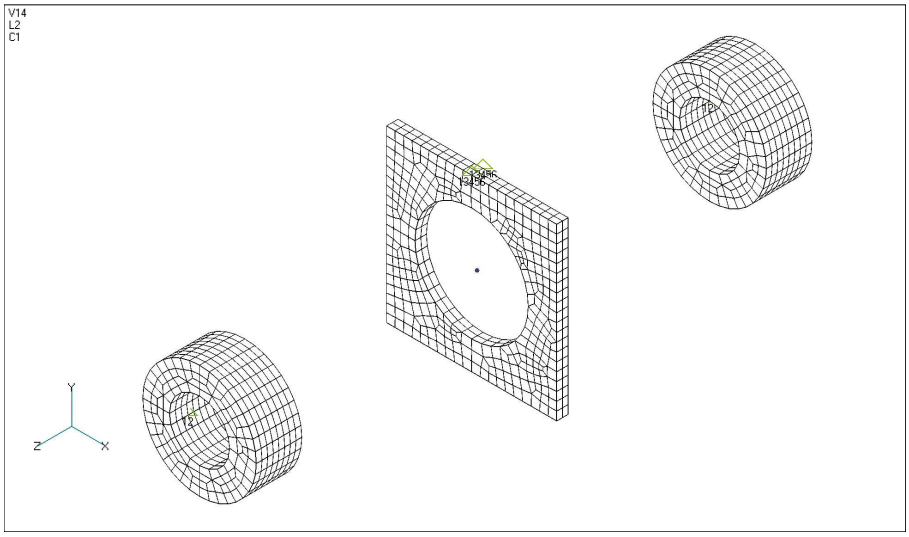

Fig. 14. Loading ring and end caps define the boundary conditions in FEA model

longitudinal axis direction was kept in 45. The mesh was refined in the area surrounding the loading ring and the aluminum end-caps. Figure 15 shows the geometry of the test article in the test fixture. The load is applied at the midspan of the tube.

The load acting on the loading ring was distributed on an area corresponding to the contact area of the load cell extension. A load of 20 lbs was distributed among 8 of the elements on the top face of the ring. The pressure load applied on them was 166.66 psi.

Maximum and minimum u_y (T_y) translation for the different models investigated in the convergence study were obtained and compared in Table V.

B. Results

For each model, loads, nodal displacements and ply by ply element stress and strain were provided in the output.

A computer with an Intel Pentium 4 processor at 1700 MHz running under

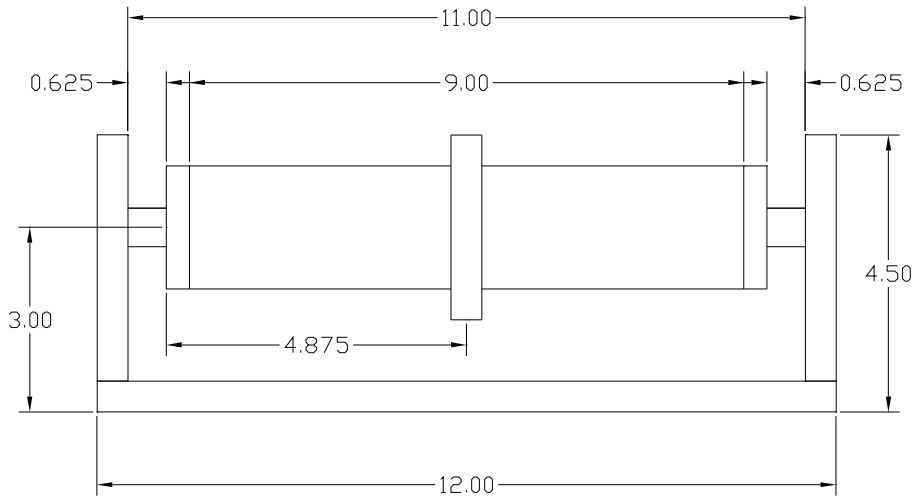

Fig. 15. Test article and fixture dimensions

Table V. Convergence study

# of Elements	**# of Elements along z-axis**	**# of Elements circumference**	**w (in)**	**CPU time (secs)**
1936	45	18	0.00072017	11.8
3282	45	28	0.00071647	19.4
4184	45	36	0.00071442	38.7
1846	45	18	0.00073368	32.2
3142	45	28	0.00072839	64.1
4004	45	36	0.00072428	65.2

Microsoft Windows 2000 Professional was used to perform the finite element analyzes.

After this study, the 45x36 mesh was considered best for the analysis and the four stacking sequences were modeled using this mesh size. Because we are interested in small displacements we need a finer mesh to account for small variations. The use of quadratic elements was chosen. Fig. 16 shows the final mesh.

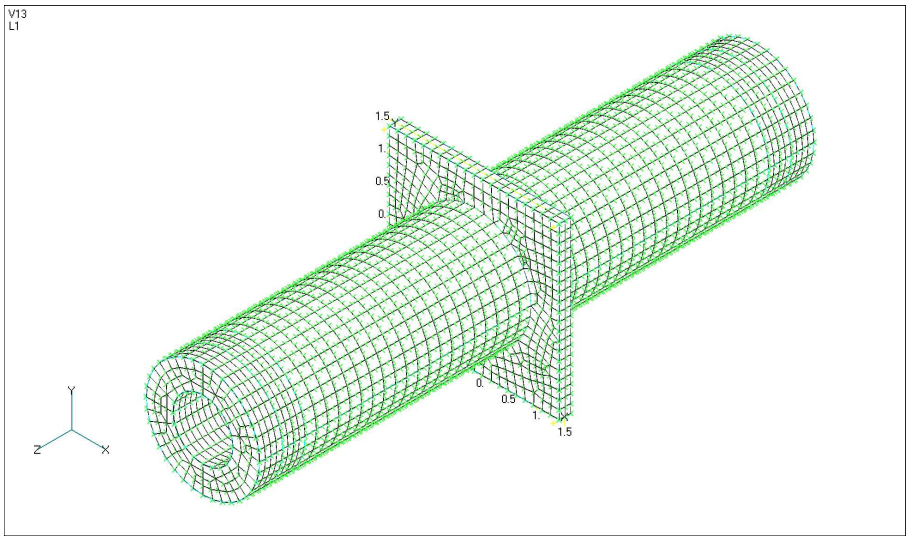

Fig. 16. Final mesh

The postprocessor is able to express the resulting displacements and stresses in the material coordinate system in which the x-axis is aligned with the direction of the fibers in each layer. Several plots were obtained from the FE analysis and they are presented in the section of results.

Because no large deformations were observed in the experiments, the non-linear effects due to large deformations were not modeled. No progressive damage analysis and no failure criteria were included in the analysis.

1. $[0/90]_4$ carbon-epoxy tubes

Figure 17 shows the u_y translation of the $[0/90]_4$ specimen.

a. Stresses through the thickness for the $[0/90]_4$ specimen

Table VI shows the maximum values corresponding to stresses σ_x, σ_y and τ_{xy} ply by ply in the material coordinates system (Mcs) for the $[0/90]_4$ specimen.

Figure 18 shows the contour corresponding to the stress σ_x for ply 8 and the element carrying the maximum stress.

Figure 19 shows the contour corresponding to the stress σ_y for ply 8 and the element carrying the maximum stress.

Table VI. Maximum values of stress ply by ply $[0/90]_4$ specimen

Ply #	σ_x **Mcs (psi)**	σ_y **Mcs (psi)**	τ_{xy} **Mcs (psi)**
1	705.27	-44.408	86.874
2	-683.78	46.422	-86.793
3	662.94	-46.911	86.752
4	-729.98	49.539	-86.712
5	743.52	-51.474	86.671
6	-816.2	52.551	-86.671
7	835.12	-57.795	86.59
8	-902.44	61.644	-86.55

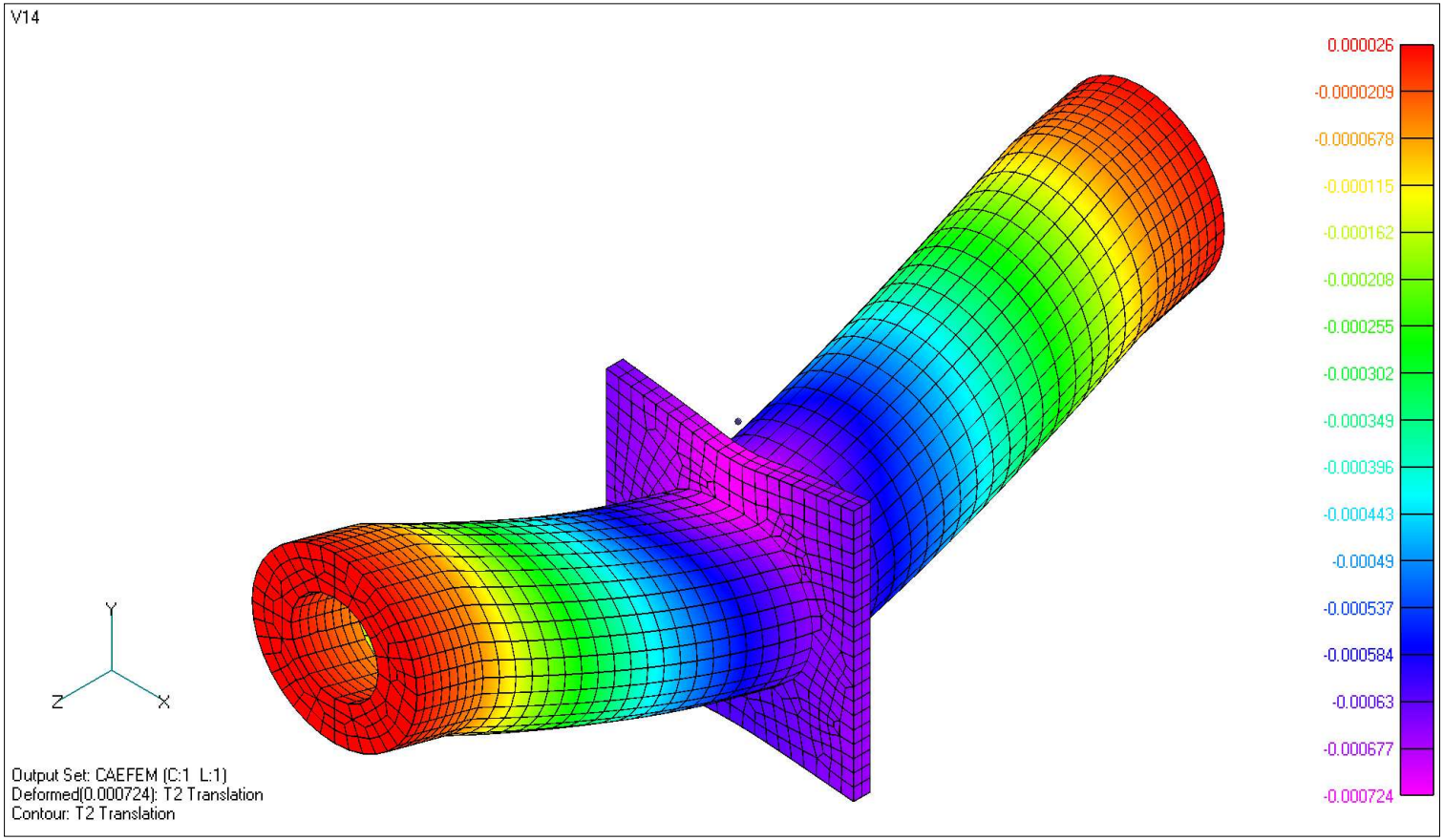

Fig. 17. $[0/90]_4$ u_y (T_y) translation

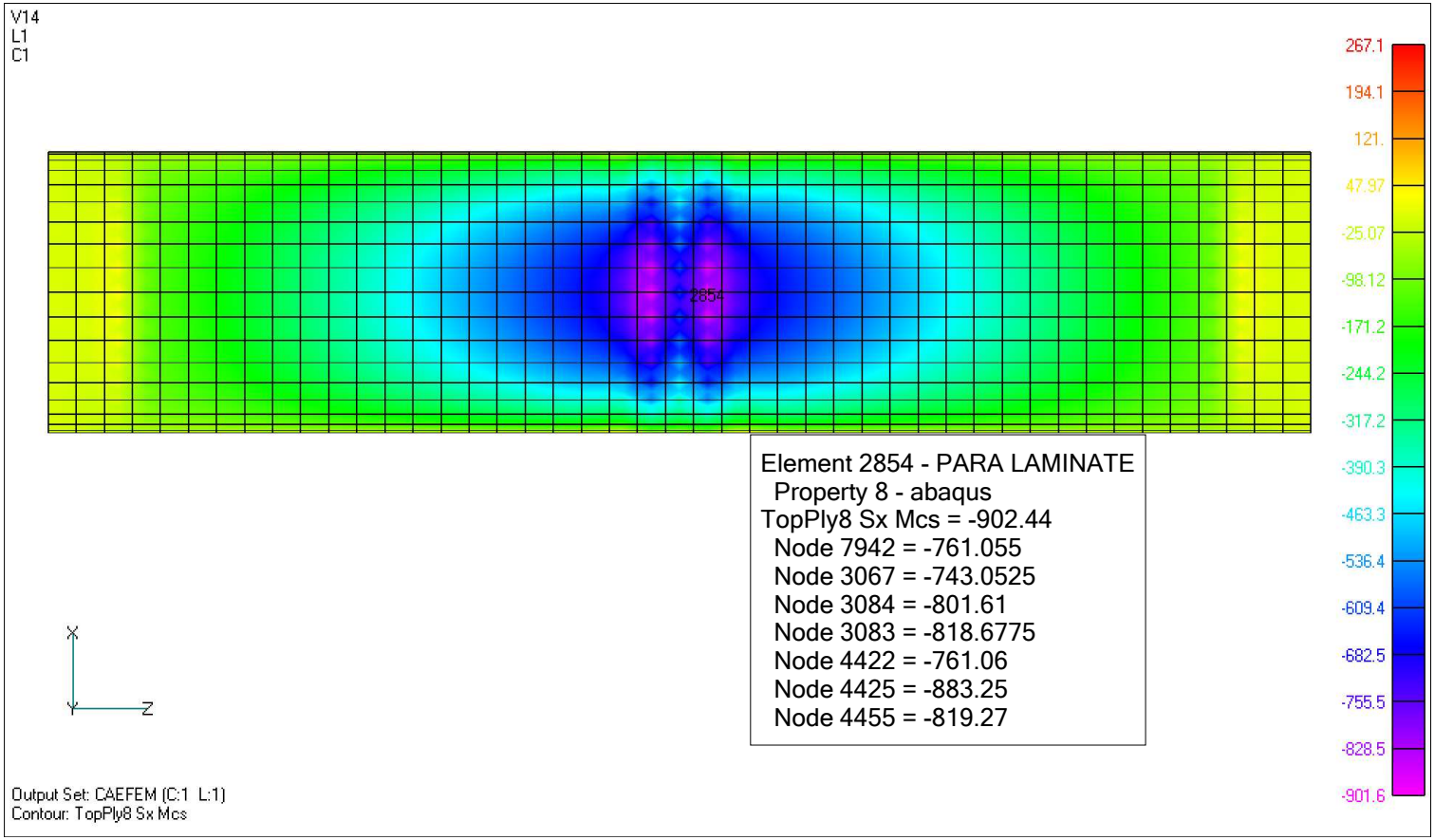

Fig. 18. Maximum stress σ_x ply 8 $[0/90]_4$

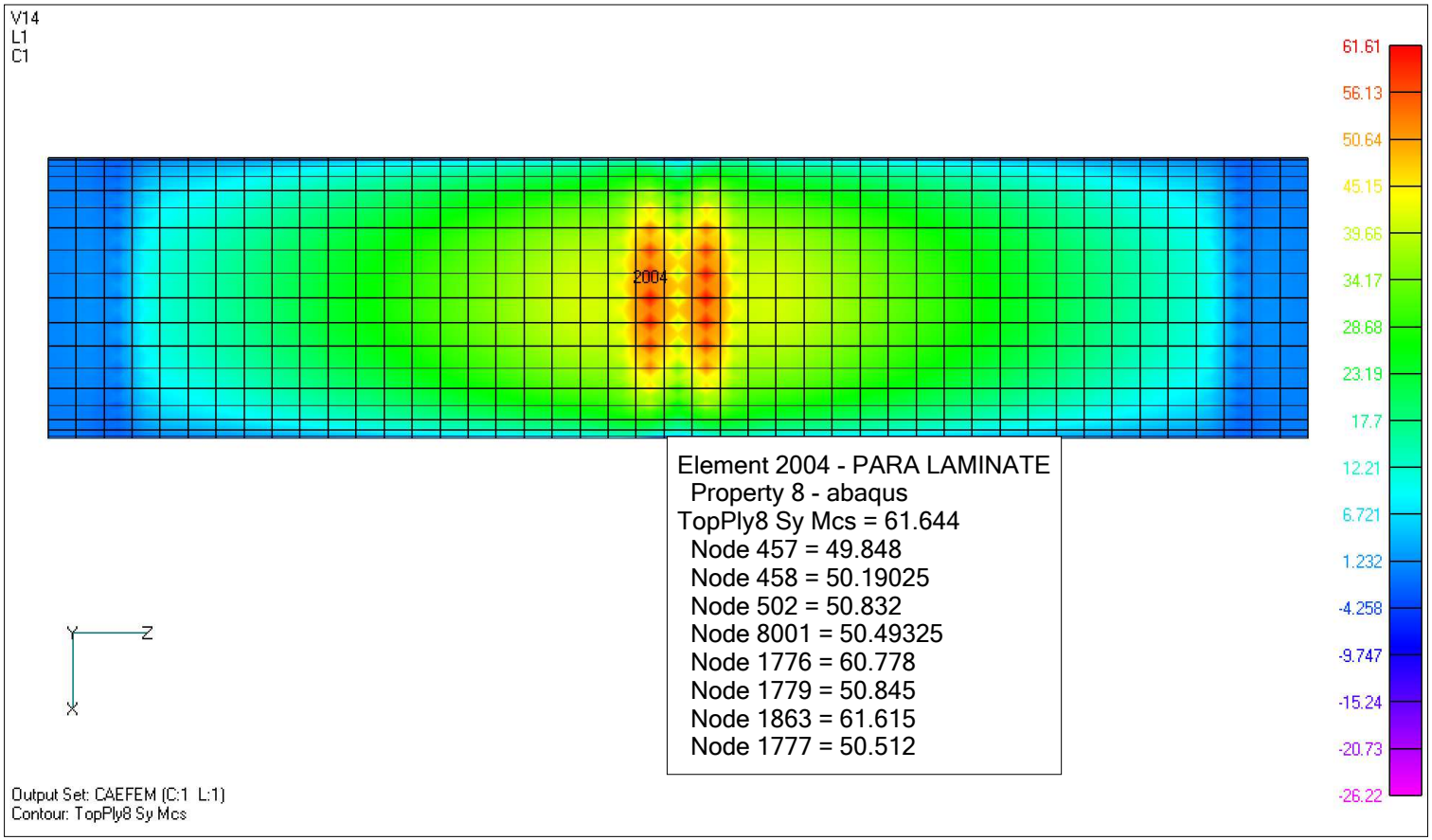

Fig. 19. Maximum stress σ_y ply 8 $[0/90]_4$

b. Strains through the thickness for the $[0/90]_4$ specimen

Table VII shows the maximum values of ϵ_x, ϵ_y and γ_{xy} ply by ply in the material coordinates system (Mcs) for the $[0/90]_4$ specimen.

Contours showing the maximum strains for certain layers of the $[0/90]_4$ specimen are presented in appendix A.

Table VII. Maximum values of strain ply by ply $[0/90]_4$ specimen

Ply #	ϵ_x **Mcs**	ϵ_y **Mcs**	γ_{xy} **Mcs**
1	4.2924E-5	-4.0649E-5	8.518E-5
2	-4.1681E-5	4.1218E-5	-8.5101E-5
3	4.0365E-5	-4.2196E-5	8.5062E-5
4	-4.4554E-5	4.2377E-5	-8.5022E-5
5	4.5162E-5	-4.7165E-5	8.4982E-5
6	-4.9777E-5	4.7953E-5	-8.4943E-5
7	5.0753E-5	-5.2388E-5	8.4903E-5
8	-5.5E-5	5.3554E-5	-8.4863E-5

Figure 20 shows the variation of strain through the thickness for one element of the $[0/90]_4$ specimen.

2. $[0/90]_3$ carbon epoxy tube

Figure 21 shows the u_y (T_y) translation for the $[0/90]_3$ specimen.

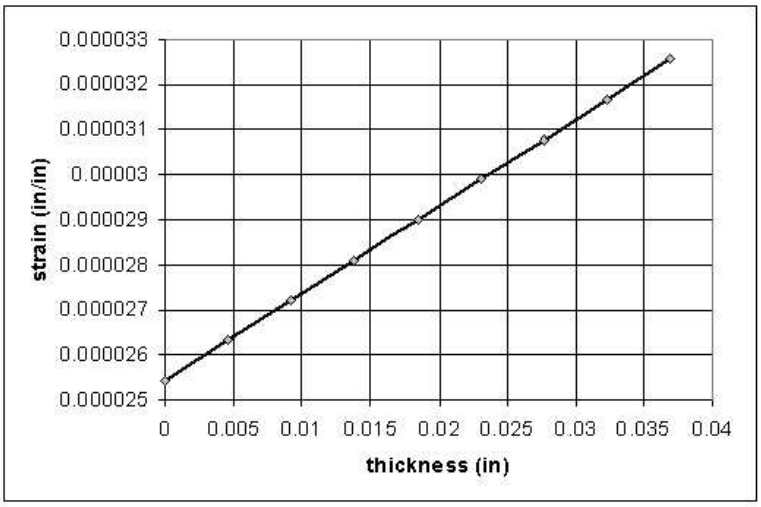

Fig. 20. Strain vs thickness in element 2048, $[0/90]_4$ specimen

a. Stresses through the thickness for the $[0/90]_3$ specimen

Table VIII shows the maximum values corresponding to stresses σ_x, σ_y and τ_{xy} ply by ply in the material coordinates system (Mcs) for the $[0/90]_3$ specimen.

b. Strains through the thickness for the $[0/90]_3$ specimen

Figure 22 shows the variation of strain through the thickness for one element of the $[0/90]_3$ specimen.

Table IX shows the maximum values of strains ϵ_x, ϵ_y and γ_{xy} ply by ply in the material coordinates system (Mcs) for the $[0/90]_3$ specimen.

3. $[0/90]_2$ carbon epoxy tube

Figure 23 shows the u_y (T_y) translation for the $[0/90]_2$ specimen.

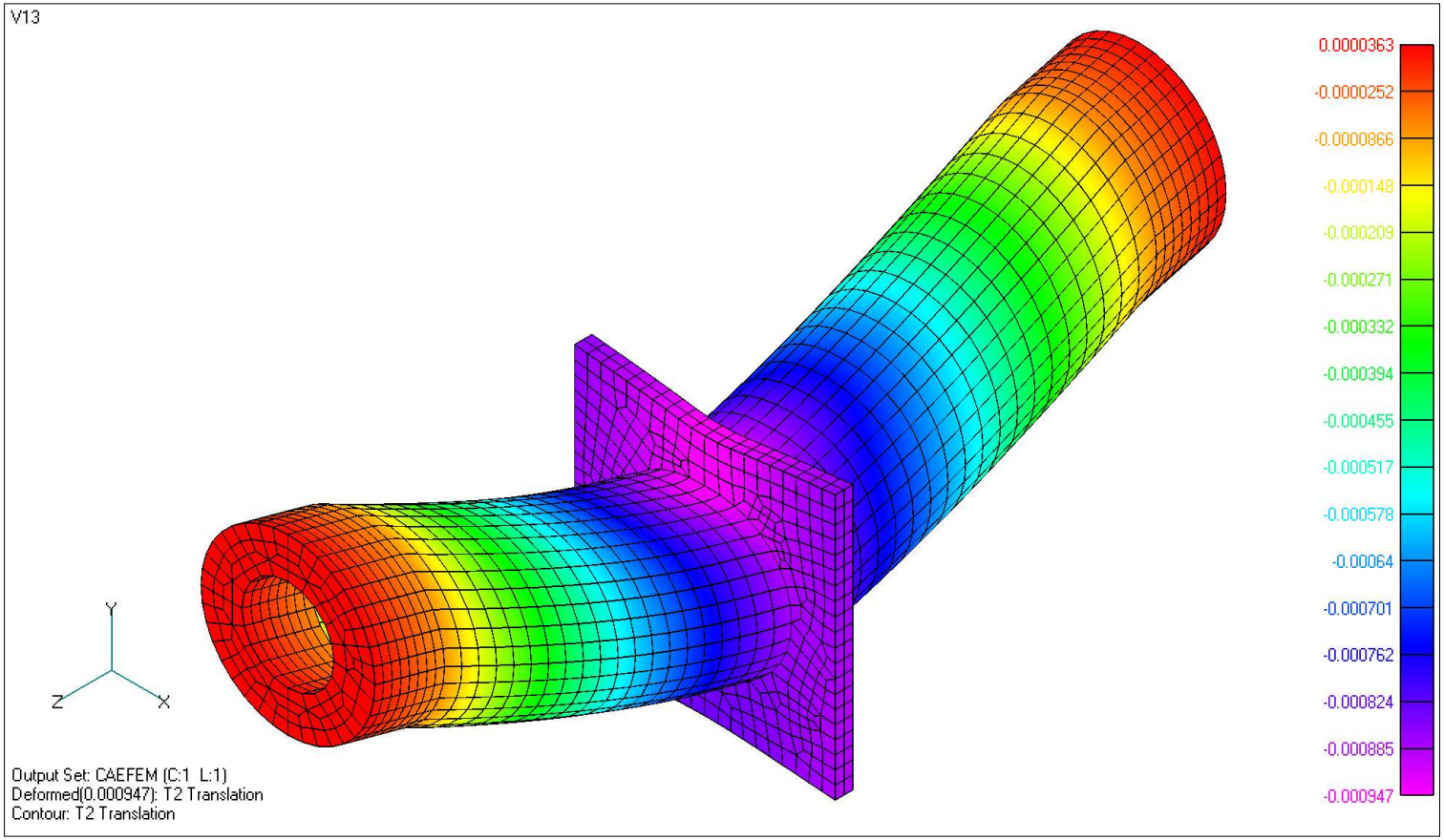

Fig. 21. $[0/90]_3$ u_y (T_y) translation

Table VIII. Maximum values of stress ply by ply $[0/90]_3$ specimen

Ply #	σ_x **Mcs (psi)**	σ_y **Mcs (psi)**	τ_{xy} **Mcs (psi)**
1	935.41	-60.82	115.92
2	-922.39	61.927	-115.38
3	940.12	-63.905	115.32
4	-1020.2	70.642	-115.3
5	1071.5	-72.42	115.29
6	-1138.1	79.404	-115.27

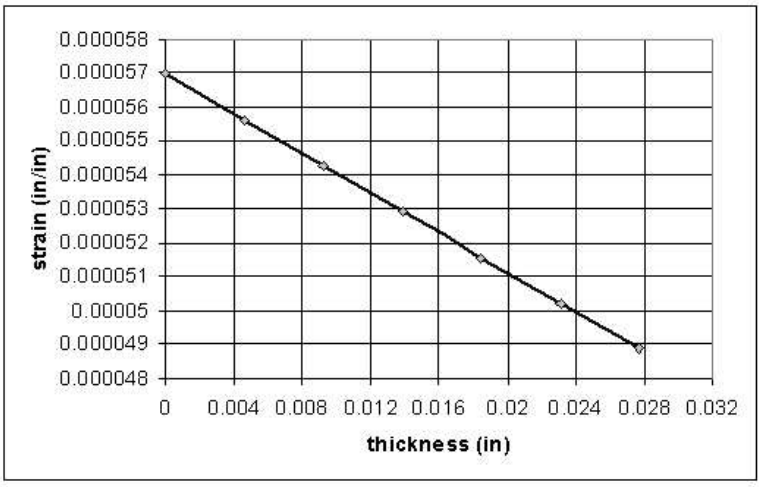

Fig. 22. Strain vs thickness in element 2050, $[0/90]_3$ specimen

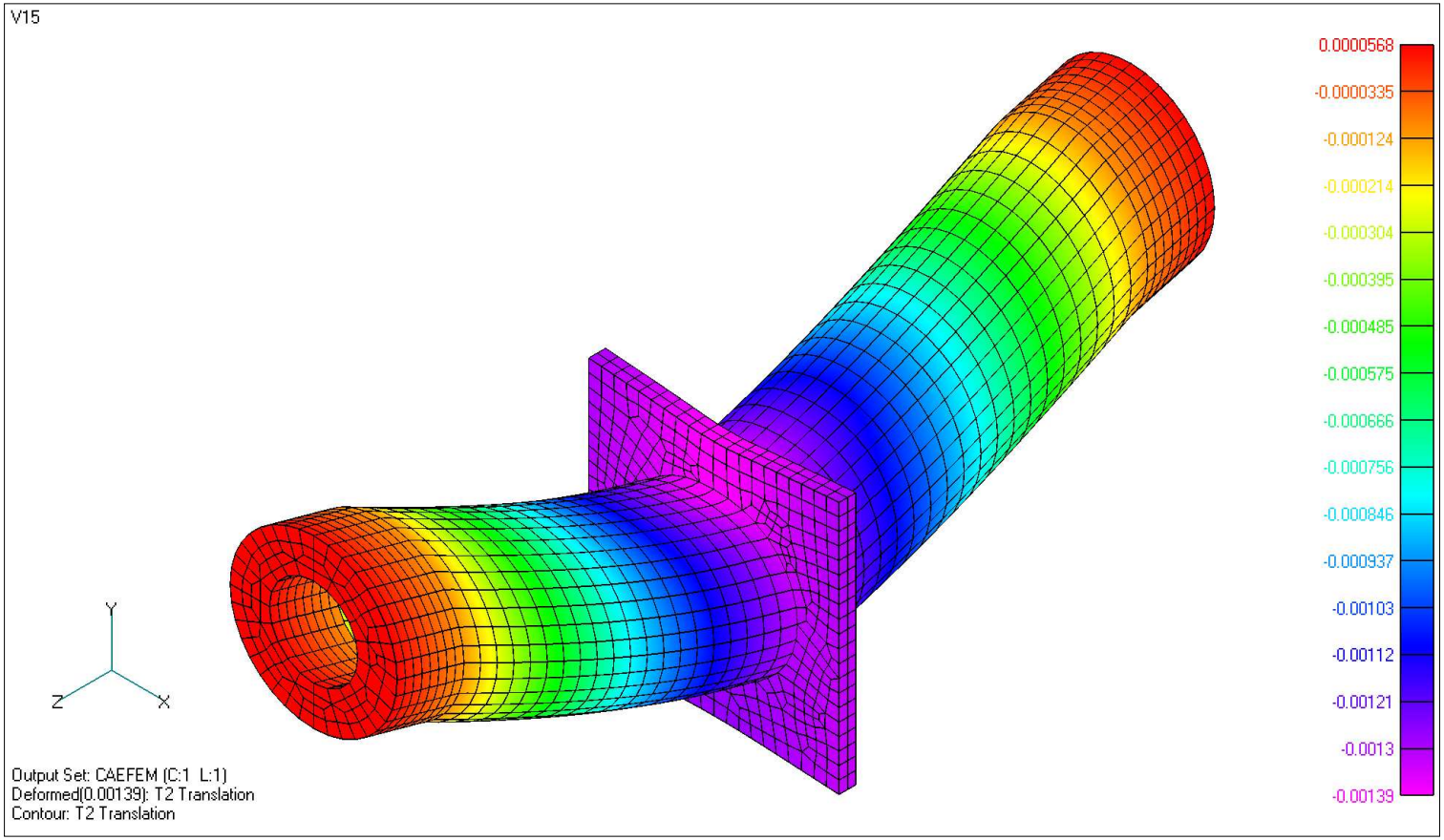

Fig. 23. $[0/90]_2$ u_y (T_y) translation

Table IX. Maximum values of strain ply by ply $[0/90]_3$ specimen

Ply #	ϵ_x **Mcs**	ϵ_y **Mcs**	γ_{xy} **Mcs**
1	5.6961E-5	-5.5294E-5	1.1367E-4
2	-5.6206E-5	5.4265E-5	-1.1313E-4
3	5.7115E-5	-5.8648E-5	1.1308E-4
4	-6.2225E-5	6.1112E-5	-1.1306E-4
5	6.5128E-5	-6.5801E-5	1.1304E-4
6	-6.9378E-5	6.9148E-5	-1.1302E-4

a. Stresses through the thickness for the $[0/90]_2$ specimen

Table X shows the maximum values of stresses σ_x, σ_y and τ_{xy} ply by ply in the material coordinates system (Mcs) for the $[0/90]_2$ specimen.

Table X. Maximum values of stress ply by ply $[0/90]_2$ specimen

Ply #	σ_x **Mcs (psi)**	σ_y **Mcs (psi)**	τ_{xy} **Mcs (psi)**
1	1374.1	-93.981	173.54
2	-1420.3	92.825	-173.2
3	1519.4	-101.79	172.71
4	-1609.8	112.32	-172.67

b. Strains through the thickness for the $[0/90]_2$ specimen

Figure 24 shows the variation of strain through the thickness for one element of the $[0/90]_2$ specimen.

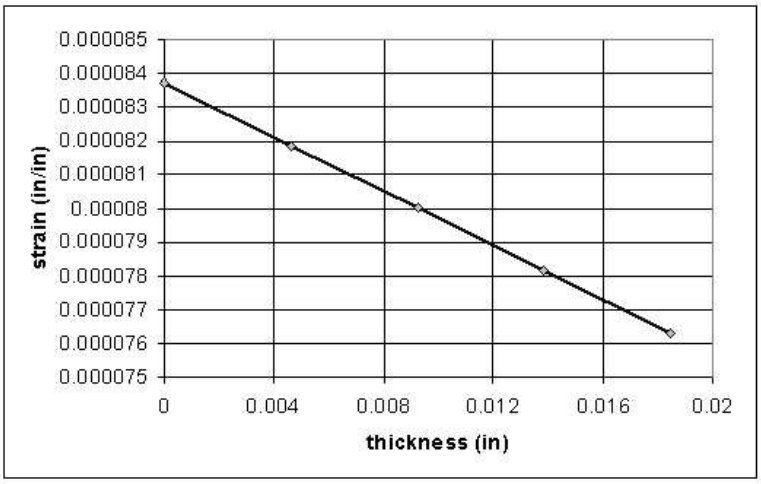

Fig. 24. Strain vs thickness in element 2050 $[0/90]_2$ specimen

Table XI shows the maximum values of strains ϵ_x, ϵ_y and γ_{xy} ply by ply in the material coordinates system (Mcs) for the $[0/90]_2$ specimen.

Table XI. Maximum values of strain ply by ply $[0/90]_2$ specimen

Ply #	ϵ_x **Mcs**	ϵ_y **Mcs**	γ_{xy} **Mcs**
1	8.3716E-5	-8.5017E-5	1.7016E-4
2	-8.662E-5	8.6475E-5	-1.6948E-4
3	9.2395E-5	-9.2372E-5	1.6935E-4
4	-9.8125E-5	9.8342E-5	-1.6931E-4

4. $[0/90/45/\text{-}45]_s$ carbon epoxy tube

Figure 25 shows the u_y (T_y) translation for the $[0/90/45/-45]_s$ specimen.

a. Stresses through the thickness for the $[0/90/45/-45]_s$ specimen

Table XII shows the maximum values of stresses σ_x, σ_y and τ_{xy} ply by ply in the material coordinates system (Mcs) for the $[0/90/45/-45]_s$ specimen.

Table XII. Maximum values of stress ply by ply $[0/90/45/-45]_s$ specimen

Ply #	σ_x **Mcs**	σ_y **Mcs**	τ_{xy} **Mcs**
1	949.34	-58.204	-33.774
2	-917.79	59.49	33.596
3	-565.88	-40.101	-79.502
4	-591.3	-41.753	80.288
5	-616.29	-43.435	81.075
6	-693.03	-45.297	-81.879
7	-1097.9	63.936	33.626
8	963.24	-74.789	-33.858

b. Strains through the thickness for the $[0/90/45/-45]_s$ specimen

Table XIII shows the maximum values of strains ϵ_x, ϵ_y and γ_{xy} ply by ply in the material coordinates system (Mcs) for $[0/90/45/-45]_s$ the specimen.

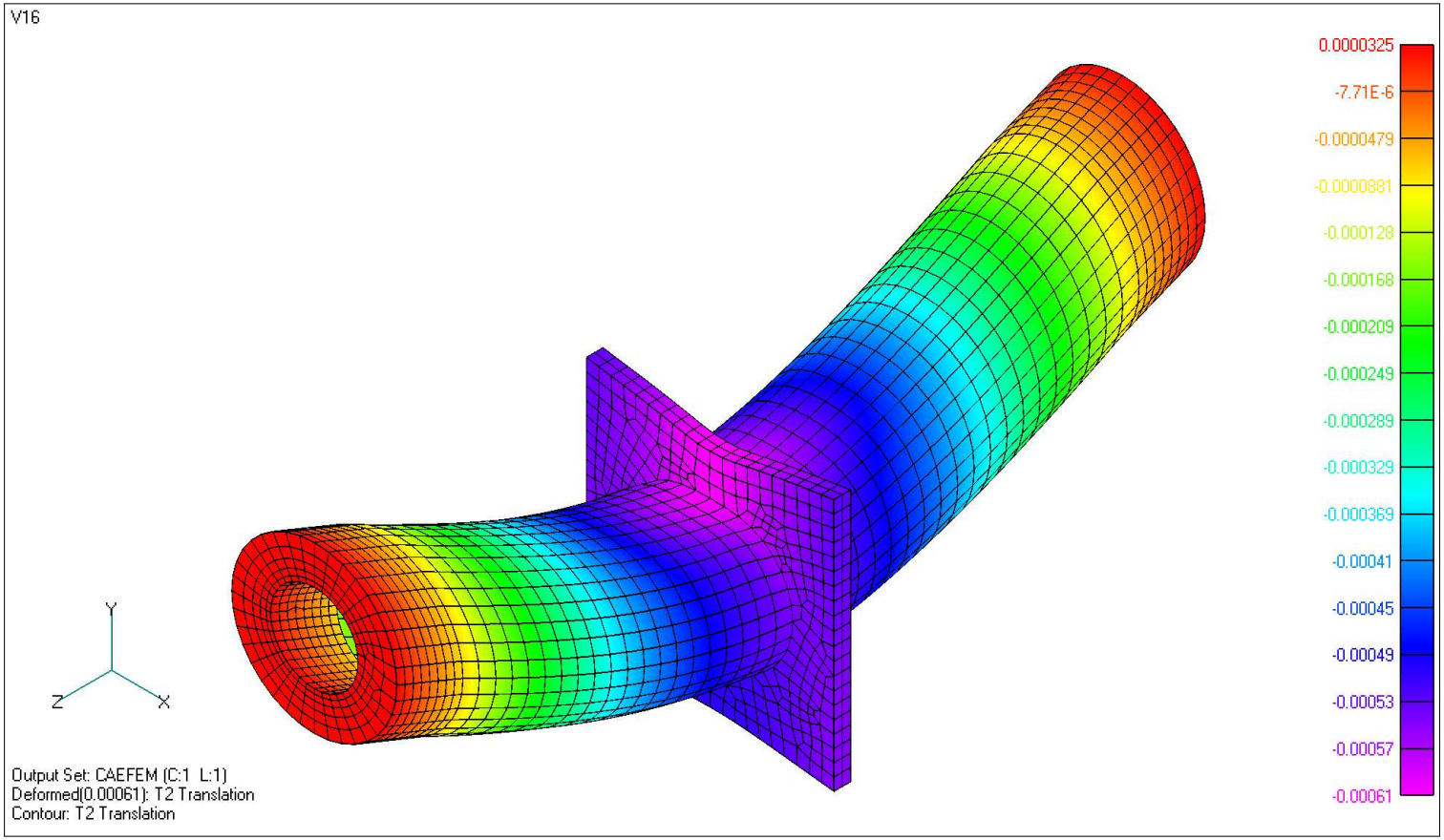

Fig. 25. $[0/90/45/-45]_s$ u_y (T_y) translation

Table XIII. Maximum values of strain ply by ply $[0/90/45/-45]_s$ specimen

Ply #	ϵ_x **Mcs**	ϵ_y **Mcs**	γ_{xy} **Mcs**
1	5.7915E-5	-5.558E-5	-3.3116E-5
2	-5.6157E-5	5.4762E-5	3.2941E-5
3	-3.4367E-5	-3.4393E-5	-7.7953E-5
4	-3.5914E-5	-3.5851E-5	7.8724E-5
5	-3.7434E-5	-3.7335E-5	7.9495E-5
6	-3.8818E-5	-3.8954E-5	-8.0284E-5
7	-6.7047E-5	5.6176E-5	3.297E-5
8	5.8607E-5	-6.9237E-5	-3.3198E-5

CHAPTER III

EXPERIMENTAL PROCEDURE

In this chapter the required tools for the experimental testing of the composite tube are described. This includes the design and manufacturing of the mold, design and manufacturing of the test articles and fixture, as well as the testing procedure.

A. Mold manufacturing

1. Overview of manufacturing processes

There are a variety of manufacturing processes applicable to the production of composite tubes [14]. The choice of process is influenced by the properties required, quantity, costs, etc.

a. Rolling

Layers of material are rolled around a mandrel, by hand or machine, prior to consolidation and cure. Once cured, the outside diameter can be machined if required. Ideal for smaller quantities and smaller tubes where increased material costs are less significant.

b. Pultrusion

A continuous process in which fibers in the form of rovings, mat or fabric are impregnated with resin and pulled through a heated die of the required shape, molding both the inside and outside diameters. Uses raw materials in their most basic and lowest cost form, however large quantities need to be produced to justify the high tooling and set-up costs. The choice of fiber angle is limited.

c. Filament winding

After impregnating with resin the fiber is wound onto a mandrel at the angle required to produce the mechanical properties. Conventionally, tubes produced in this way have a molded inside diameter, the outside diameter can be machined if required, after curing.

As described above, the pultrusion and filament winding processes require special and expensive equipment and qualified technicians. For that reason the rolling technique using a wet layup of bidirectional woven cloth was chosen. Because the tubes were to be thin-walled, a multicomponent mandrel was designed and fabricated so that it could be removed with minimal force. The mandrel fixed the inside diameter of the tube. The outside diameter was minimized by spiral wrapping the lay-up with heat shrink tape and applying heat.

2. Mold fabrication

The multicomponent mold is composed of 9 pieces: a central bar (steel), four blades (steel) and four cylindrical segments (aluminum). Detailed drawings of each piece and assembly drawings of the mold are presented in Appendix B.

Starting from a solid cylinder of 6061 aluminum, the ends were machined and then fixed into two 5C collet fixtures. By using a slitting saw mounted in the milling machine, four segments were obtained. They are shown in Figure 26. Four steel rectangular bars were cut from their original size to match the length of the circular segments obtained before. Figure 26.

The mold was assembled around a central rod of square section exceeding the length of the 8 pieces in about 4 inches (2 inches were used at each side) with the purpose of mounting this assembly in the 5C collet fixtures. Two circular clamps hold

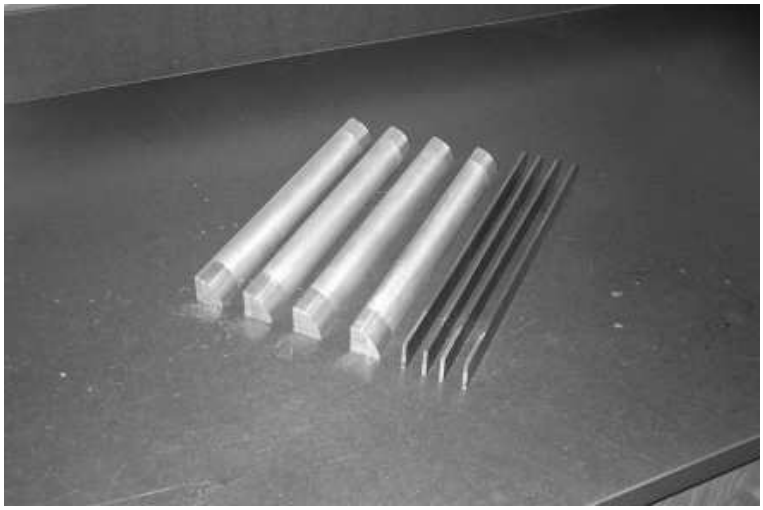

Fig. 26. Aluminum circular segments and steel blades

the assembled cylinder by both ends as shown in Figure 27.

The mold was fabricated in the Aerospace Engineering Department/Texas A&M University machine shop by the author and Dr. Tom Pollock.

The mold was supported in the two 5C square collets which were at the same time attached to the collet fixtures letting the whole assembly to rotate about its longitudinal axis. This allowed the carbon fiber and the matrix resin to be applied by spinning the assembly.

B. Test articles manufacturing

This part describes the manufacturing process of the carbon-epoxy tubes used as test articles. The initial lay-up chosen for the analysis and manufacturing was $[0/90/45/\text{-}45]_s$. For simplicity it was decided to start with a $[0/90]_4$ layup, since the 45/-45 layers are difficult to align due to the nature of the bidirectional woven carbon cloth chosen to build the specimens.

Four specimens with stacking sequence $[0/90]_4$ and three specimens with stack-

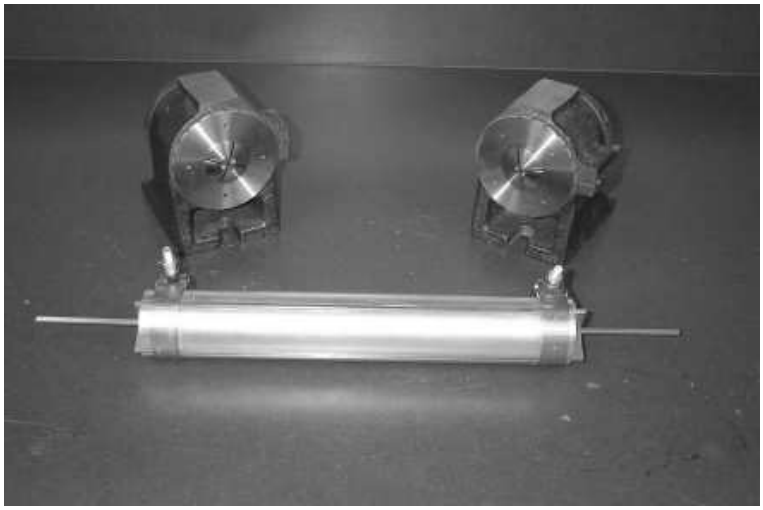

Fig. 27. Assembled mold and collet fixtures

ing sequences $[0/90]_3$, $[0/90]_2$ and $[0/90/45/\text{-}45]_s$ respectively were manufactured as described later. Detailed images of the most important steps are provided as a guide for future manufacturing.

1. Materials

The quantities of the raw materials are based on a single specimen. Adjustments must be made according to the number of specimens desired. Table XIV presents a list of the materials required in the manufacturing of the carbon/epoxy tubes.

The properties of the bidirectional woven carbon graphite cloth used for the manufacturing are given in Table XV.

105 Westsystem resin is a clear light amber, low-viscosity liquid. It can be cured in a wide temperature range (60°F-120°F). The temperature used was 68°F. 206 slow hardener is a low-viscosity mixture of polyamines. It is normally used when extended time is needed for large coating and bonding applications. Partial cure time is 9 hours at 70°F.

Table XIV. Materials for manufacturing of the carbon/epoxy tubes

1 10”x25”x0.007” plain weave bidirectional carbon fiber piece supplied by Aircraft Spruce Co.
1 roll of paper towels for cleaning purposes
1 16 oz can of PTFE release agent dry lubricant MS-122DF by Miller-Stephenson
1 set of Allen wrenches, 1 long nose locking pliers, 1 flat screwdriver
1 drive ratchet and one 3/8” drive 12 point deep socket
1 rotary cutter
1 cutting mat
1 precision ruler
1 sealing iron
1 12”x25” thin polyethylene piece
1 pair of disposable latex gloves
1 disposable respirator
2 flat brushes
1 pack of paper mini-cups
1 roll of heat shrinkable polyester tape/release coated supplied by Dunstone Hi-shrink tape
WestSystem 105-A epoxy resin 32 fl oz container
1 WestSystem 206-A slow hardener 7 fl oz container
1 WestSystem set of 301-A mini-pumps 5:1 ratio for use with WestSystem 105 resin and 205 or 206 hardeners in group size A containers
1 pack of wood mixing sticks
1 heat gun
1 balance able to register 0.01 g

Table XV. Bidirectional woven carbon graphite, www.aircraftspruce.com

Style	**Oz/Sq.Yd**	**Thickness**	**W X F**	**Weave**
282	5.7	0.007”	12.5x12.5	Plain

Using calibrated mini-pumps supplied by the resin manufacturer helped ensure accurate metering of resin/hardener mixture. These pumps are directly mounted on resin and hardener containers. The resin/hardener ratio is 5:1.

2. Manufacturing process

The manufacturing process consisted of 19 steps:

1. Cleaning of all the components of the mold using paper towels. To begin, we cleaned the nine pieces forming the mold to avoid grease and dust. This was done by using paper towels. Each time we reused the mold, we made sure that no left-overs of epoxy resin are attached to the surfaces of the pieces.

2. Applying release agent to each piece (PTFE release agent dry lubricant). A PTFE release agent and dry lubricant coat will be applied to the mold. All the surfaces (including the internal faces) must be sprayed with a thin coat.

3. Letting them dry. Allow at least 15 minutes for the PTFE coat to dry.

4. Assembling mold and attaching it to the work table. The nine pieces conforming the mold have marks at one of the ends to make them fit accurately. By looking at these ends we can make coincide the blades marked as I, II, III and IIII with the corresponding circular segments marked as ., .., ..., and .... (small indentations have been placed on these pieces). See Figure 28.

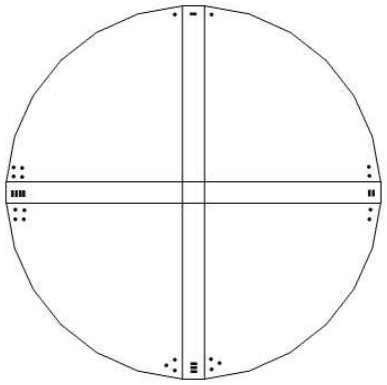

Fig. 28. Cross sectional area of mold showing assembly sequence

5. Cutting the bidirectional woven carbon cloth. We produce an 8-layered laminated tube, but the material we are working with is a bidirectional plain weave. The way we account for the number of layers is by considering one layer of bidirectional cloth as two layers of unidirectional carbon fibers, so according to the dimensions of the mold, we can calculate how long the carbon fiber piece must be in order to complete four layers around the circumference. This calculation is presented here:

$$\pi * D * 4 = 25.13\, in \tag{3.1}$$

6. Attaching a piece of polyethylene film to the carbon cloth at one of the ends by means of a hot sealing iron. The next step is to cut a piece of polyethylene long enough to cover the mold during two rotations and with the same width as the carbon fiber cloth (10"x12"). In this way, the sharp edges that the steel blades mark in the interior surface of the finished tube are attenuated. See Figure 29.

7. Loosening the assembly by means of the clamps at the ends in such a way that the pieces separate slightly. Introducing one end of the polyethylene in one of the slots made between the circular segments and the blades. It is recommended

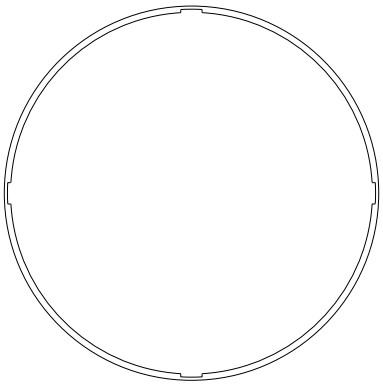

Fig. 29. Exaggerated view of effect of steel blades on internal surface of finished specimen

to mark a line on the polyethylene to act as a guide to align it properly with one of the iron blades at the moment of clamping the assembly. This is shown in Figure 30.

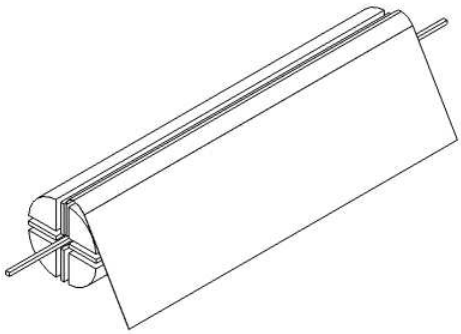

Fig. 30. Slot between circular segment and steel blade

8. Completing the mold assembly. Using the drive ratchet and the corresponding socket to clamp the assembly.

9. Placing a weight at the free end of the carbon cloth with some clips to stretch the fibers and get a better fit between mold and plain weave. This is shown in Figure 31. The amount of resin to be used based on the required wall thickness and

assuming a fiber volume ratio of 50% was calculated. The calculation of the resin volume fraction V_m is obtained based on the properties of the matrix. (specific gravity of the mixture per full stroke of resin and full stroke of hardener). This calculations are shown in the next equations.

V_f=0.5,

V_m=0.3,

V_v=0.2,

where V_f, V_m and V_v have been defined in equations 2.2 to 2.4 in Chapter 2.

The wall thickness of the composite considering just the carbon fiber should be 0.028 inches according to the desired tube dimensions (four layers of the bidirectional carbon cloth) and the plain weave thickness of 0.007 inches as shown:

$$ri = 0.99075\, in$$

is the inner radius of the tube given by mold dimensions, and

$$ro = 0.99075 + 0.028 = 1.01875\, in$$

represents the outer radius.

The volume of the composite just made up of fibers would be:

$$V_f = \pi \left({r_o}^2 - {r_i}^2 \right) l \tag{3.2}$$

where l is the length of the tube, and equals 9.0 inches.

The volume just calculated is the fiber volume ratio of 50%, then:

$$V_f = 0.5\, V_{total} \tag{3.3}$$

and the total volume of the composite should be:

$$V_{total} = V_f/0.5 = 3.1818\, in^3$$

from which 20% are voids and surface irregularities, therefore the volume of required resin is:

$$V_r = 0.3 * V_{total} = 0.9545\, in^3$$

This is the volume we need to apply to the composite tube. Because it is easy for us to weight the mixture, we will work with just that mass of resin when doing the hand-layup.

The specific gravity of the mixture according with manufacturer's data is :

$$\rho_{mixture} = 1.18\, g/cm^3$$

Now because

$$\rho_r = \frac{m_r}{V_r} \tag{3.4}$$

$$m_r = 1.18\, g/cm^3 * 0.9545\, in^3 * (2.54\, cm/in)^3 = 18.46\ grams$$

Then by using the pair of mini-pumps we get as many full strokes of resin and hardener as needed until completing 18.46 grams. Just the previous amount is placed in a new paper cup. We then apply the resin to the carbon fiber.

10. Applying some PTFE release agent to the polyethylene before applying the resin as indicated in Figure 32.

11. Mixing resin and hardener in a small cup. The exothermic reaction produced when mixing resin and hardener will heat up the mixing cup, so a paper cup is

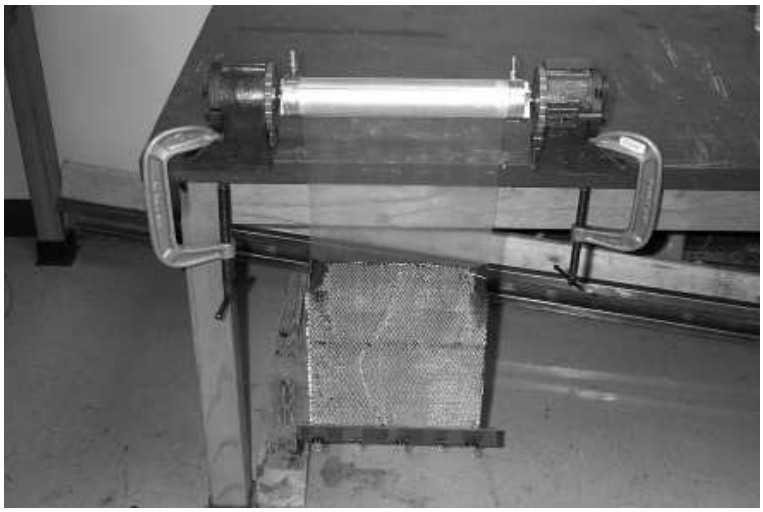

Fig. 31. Mold, polyethylene, woven carbon fiber and weight

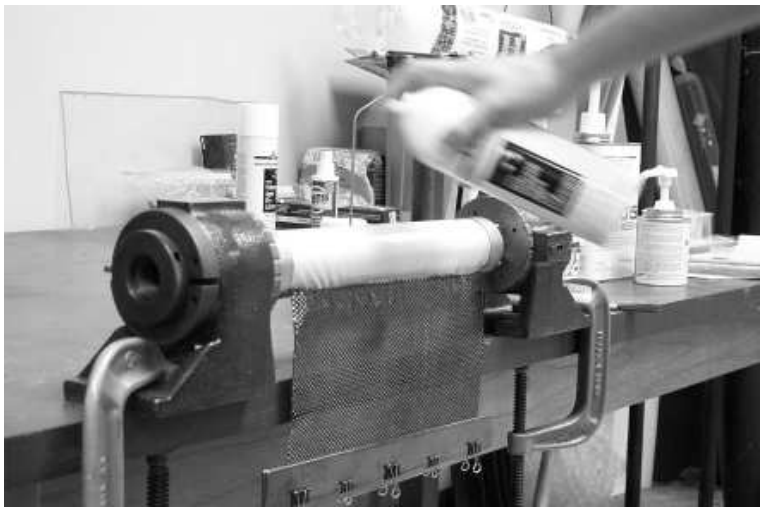

Fig. 32. Application of PTFE

recommended for this stage.

12. Using the collet fixtures, spin the assembly two complete turns in such a way that the polyethylene covers the whole cylinder hiding the edges of the central blades of the mold.

13. Starting the application of resin to the mold by means of a 3/4" width clean flat brush. The application of the resin will start directly on the polyethylene surface. Spinning the mold slowly and applying resin onto the polyethylene is equivalent to precoating the surface of the mold until wrapping the polyethylene completely. This is shown in Figure 33. The portion of polyethylene coated must be that which will touch the carbon cloth.

Fig. 33. Application of resin to polyethylene

14. Wrapping the carbon cloth slowly at the same time that the resin is applied (trying to avoid excess). See Figure 34. The mold is rotated and the resin is applied to the bidirectional woven carbon cloth. Once we have wrapped almost

the entire length of the bidirectional cloth, the attached weight is removed carefully.

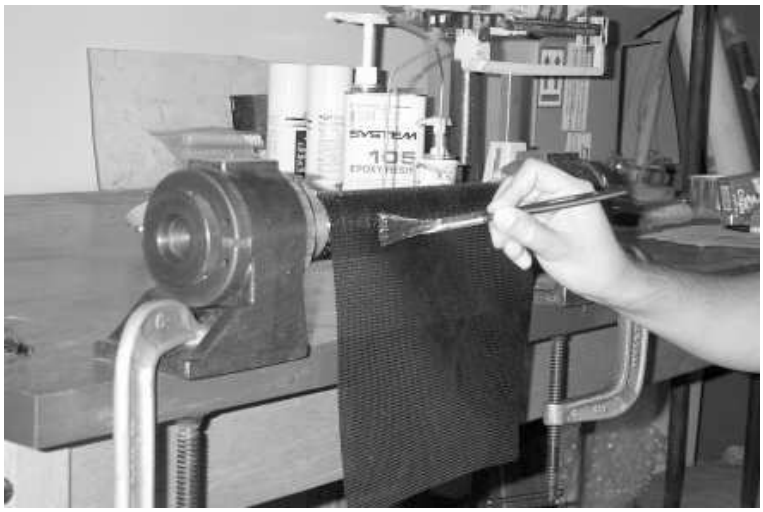

Fig. 34. Application of resin to fibers

15. Completing four layers and finishing the application of resin. Figure 35 shows the completed layup.

16. Applying a heat shrinkable tape. Excess resin must be removed and voids must be collapsed to improve the quality of the finished specimen. A release coated heat shrinkable polyester tape is used to accomplish this. Tape characteristics are presented in Table XVI.

    Wrapping the shrinkable tape around all the external surface of the piece. Using the release coated side of the tape directly on the resin. This is shown in Figure 36.

17. Using a heat gun. Heat the tape uniformly as possible to make it shrink and force the excess of resin to leave the specimen. This is illustrated in Figure 37.

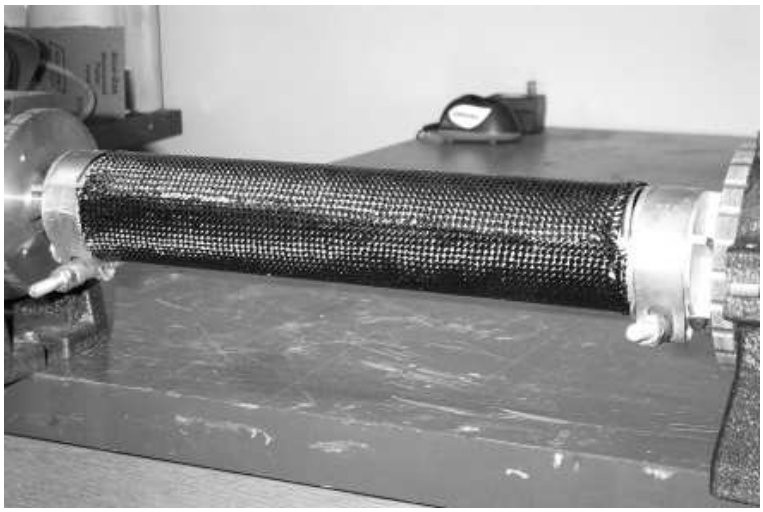

Fig. 35. Resin application finished

Table XVI. Shrink tape characteristics

Nominal thickness x width	0.002" x 1/2"
Nominal shrinkage (lengthwise) at 300F	20%
Maximum shrink force (lengthwise)	2500 PSI
Starts to shrink	175F
Temperature range for practical use	200-400F
Approx. time to reach full shrink after exposure to temp.	Minutes

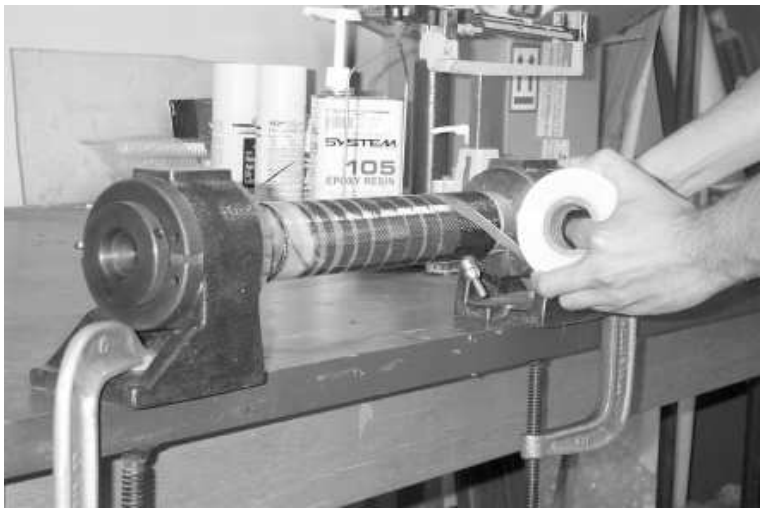

Fig. 36. Tape application

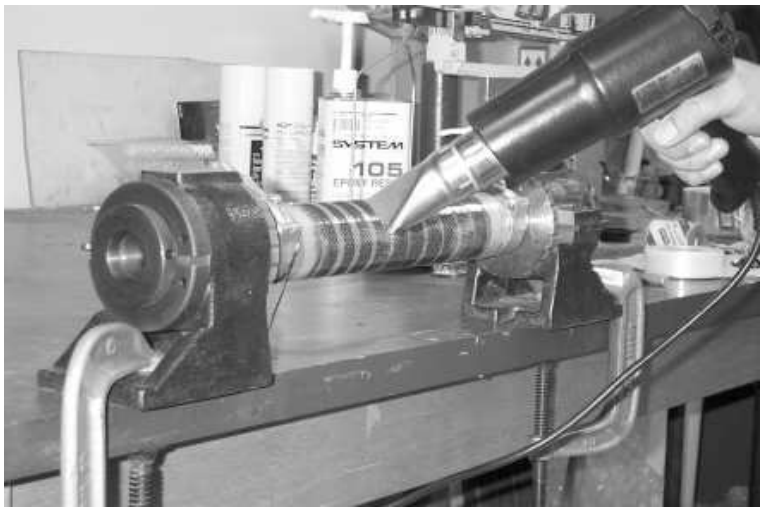

Fig. 37. Heating of tape

18. Allowing at least 12 hrs of curing at room temperature. Maximum strength is reached after cure at 72°F for two weeks.

19. Disassembling the set to take the hollow piece out. Figure 38 and Figure 39. The disassembly procedure uses the central rod to loose the assembly. Once this piece has been removed, the others get space to move and they are taken out easily.

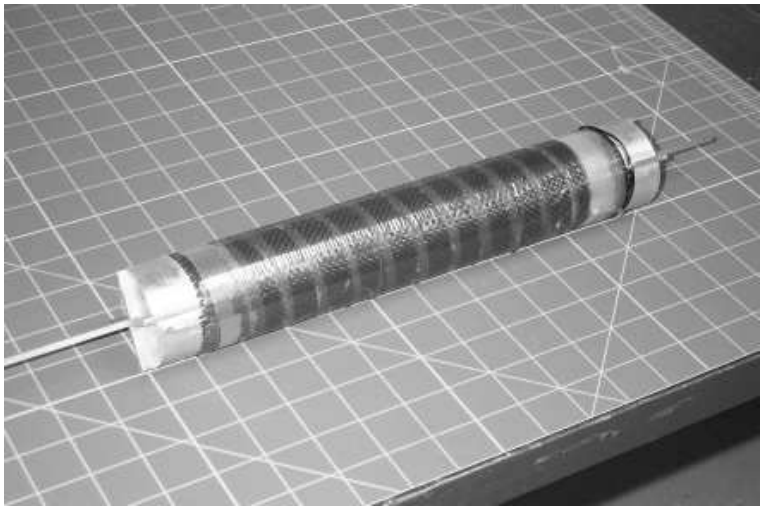

Fig. 38. Supports removed

3. Tube trimming

The seven tubes for testing were trimmed to a length of 9 inches.

They were mounted into the trimming device shown in Figure 40.

The trimming device consists of an aluminum angle screwed to a hinge. The hinge is fastened to a working table using screws. Each tube is placed on this angle and then restricted to move in the longitudinal direction by means of a small clamp and an aluminum cap as shown in Figure 41.

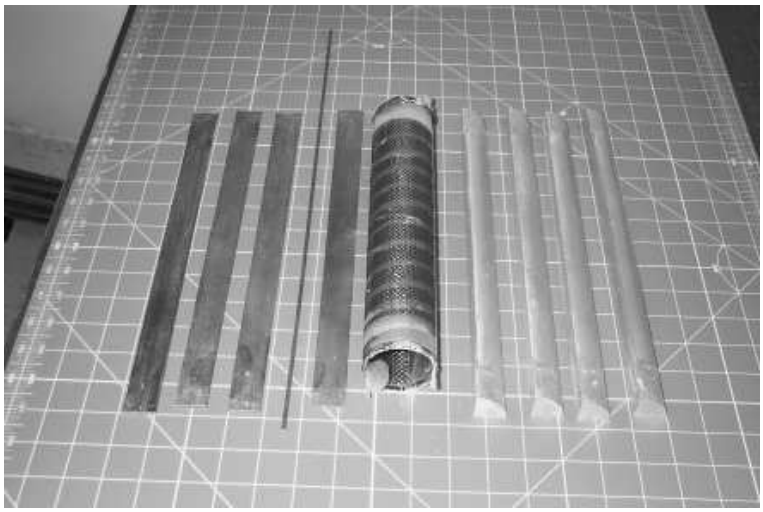

Fig. 39. Mold disassembled

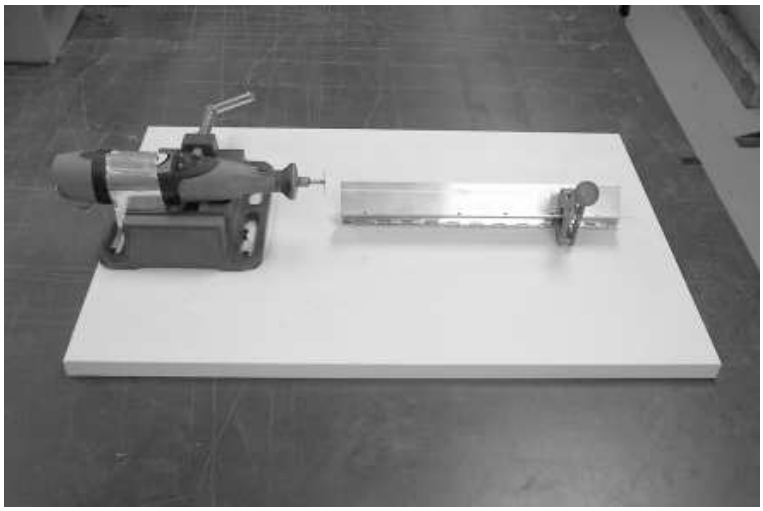

Fig. 40. Trimming set

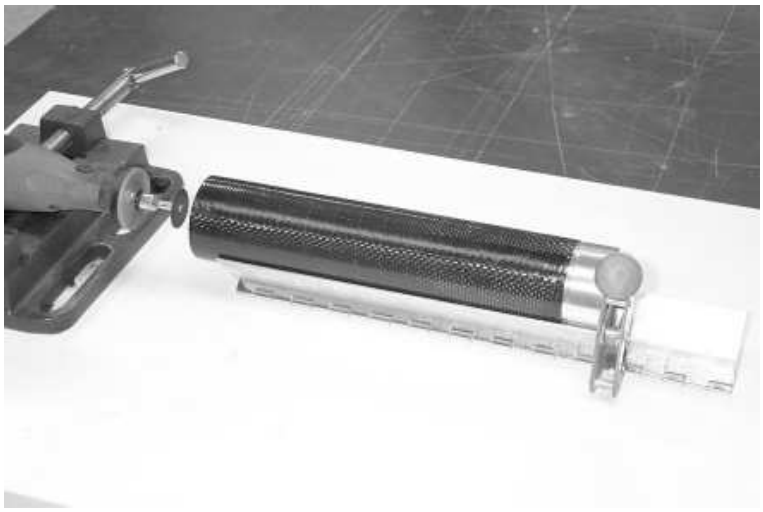

Fig. 41. Tube in trimming set

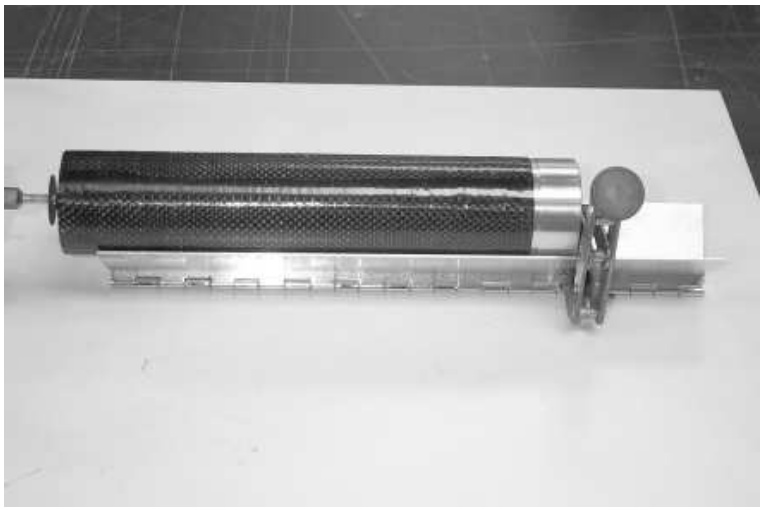

Fig. 42. Tube mounted in trimming set

Only rotation of the tube about its longitudinal axis is allowed. A Dremel 780 cordless rotary tool is mounted on an aluminum block to restrict its motion completely and is fixed into a small vise. The next step is to switch the tool on and rotate the angle with the tube inside at the same time that the tube is rotated by hand about its longitudinal axis. The cutting tool is a 15/16"x0.025" emery wheel. At the right end of the tubes, an aluminum end cap with a small step is inserted in order to restrict the longitudinal motion and get a straight cut at the opposite side. See Figure 42. A finished specimen is shown in Figure 43.

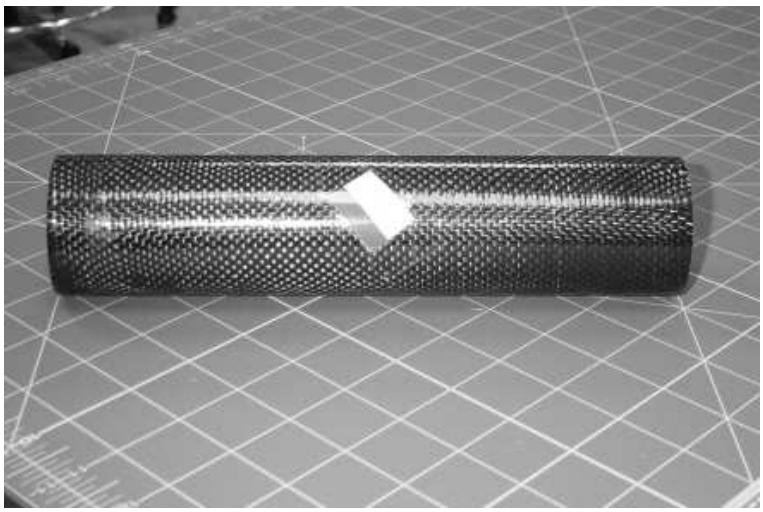

Fig. 43. Trimmed tube

Following these techniques, a total of 7 specimens were manufactured and trimmed. Figure 44 shows the finished specimens.

C. Specimen testing

The fiber angle theta was defined as the angle between the tube axis and fiber direction as shown in Figure 45.

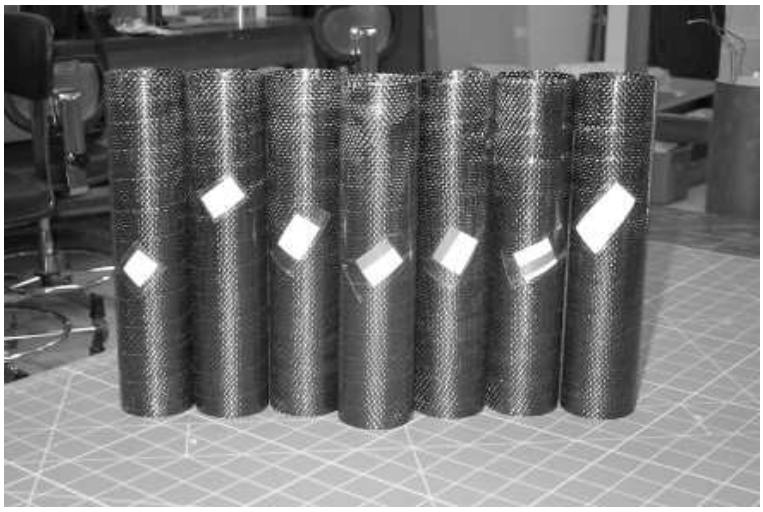

Fig. 44. Seven specimens

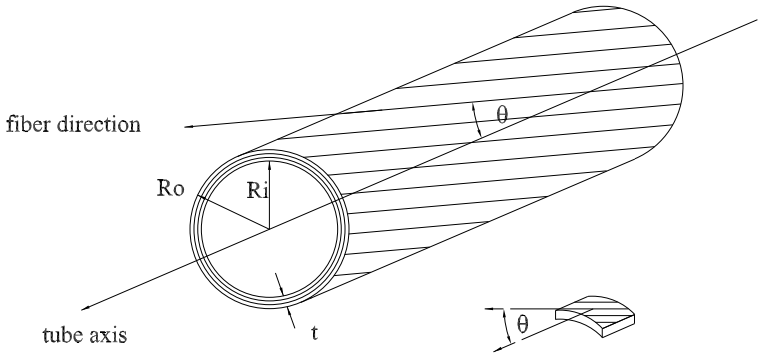

Fig. 45. Fiber angle

The dimensions of each specimen are presented in Table XVII, internal and external diameters, thickness and weights are listed. The tube diameters and thicknesses were measured with a caliper. The length of all specimens is 9.0".

Table XVII. Tube dimensions

Specimen IN	**Lay-up**	**Weight (grams)**	**Inner diameter (in)**	**Outer diameter (in)**
1	$[0/90]_4$	44.43	1.986	2.060
2	$[0/90]_4$	45.325	1.982	2.040
3	$[0/90]_4$	42.37	1.976	2.044
4	$[0/90]_4$	45.17	1.982	2.055
5	$[0/90]_3$	34.54	1.985	2.035
6	$[0/90]_2$	22.4	1.995	2.015
7	$[0/90/45/\text{-}45]_s$	46.95	1.991	2.060

In order to perform the testing it was necessary to design and manufacture a special fixture to provide boundary conditions similar to the real structure (a cantilever laminated tube). In an ideal case, the tube should be subjected to a pure bending moment to avoid localized deformation which do not simulate the response of the actual lens assembly. As illustrated previously, arrangement of spherical and linear bearings was devised to provide realistic constraints.

1. Test article and fixture design

The test article was composed of 2 end caps, one tube and one loading ring. The fixture was an assembly of two supporting arms, a base, a rod and two plain spherical

bearings. Detail drawings are provided in appendix A. To avoid local crushing at the point where the load is applied, the loading ring was used to distribute the load in a more realistic way. As mentioned in chapter 2, part A.2.b, the ends of the tube have free rotations R_x, R_y, R_z, and free translation u_z due to the use of spherical bearings which will provide the simply supported boundary condition. The spherical bearings were free to slide along the central shaft. This allowed the ends to have longitudinal movement as the deflection increases.

The fixture and test article are presented in Figure 46.

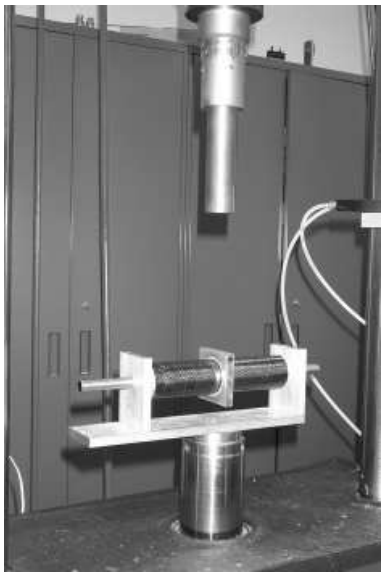

Fig. 46. Specimen mounted for testing

Because of small variations in the diameter of the tubes it was necessary to machine each pair of end-caps for each tube tested. The inner diameters are different by a few thousands of an inch for each specimen as can be seen in Table XVII and the end-caps must fit the internal diameters accurately.

The end-caps and the loading rings for each specimen were attached to the carbon-epoxy tubes by using a quick setting epoxy resin. This bonded the com-

ponents of the test articles securely and filled any possible gaps between pieces.

The seven specimens ready for testing are shown in Figure 47.

Fig. 47. Specimens ready for testing

2. Testing procedure

The testing of the 7 specimens was performed in the Structures Laboratory in the Department of Aerospace Engineering at TAMU. An MTS machine with a reversible load cell of 200 lbs capacity was utilized. The MTS machine is shown in Figure 48.

a. Load application

The cross-head of the machine was displaced at constant speed. A speed of 0.002 in/min was selected and a load cell of 200 lbs capacity was used. The load applied to all the specimens was 20 lbs. For the 2-layered specimen, a starting load of 10 lbs was selected, after which the 20 lb load was applied.

Fig. 48. MTS used for testing

b. Data acquisition

The software TestStar IIs version 2.4 by MTS was used to get the output from the load cell.

c. Experiment performing

The experiments were performed in the following way:

The specimen mounted on its test fixture was placed on the MTS machine as previously shown in Figure 46. The whole assembly was then properly aligned to allow the load to be applied perpendicular to the loading ring upper face. The cross-head of the machine was displaced at 0.002 in/min until the load value reached 20 lbf. The unloading procedure was then performed automatically.

Four tests per specimen were performed. The faces of the aluminum rings on each tube were marked as A, B, C and D as shown in Figure 49, and 20 lbs at constant

speed were applied on each ring face for the $[0/90]_4$, $[0/90]_3$ and $[0/90/45/-45]_s$ specimens. 10 lbf were applied initially to the $[0/90]_2$ specimen, followed by a second test at 20 lbf.

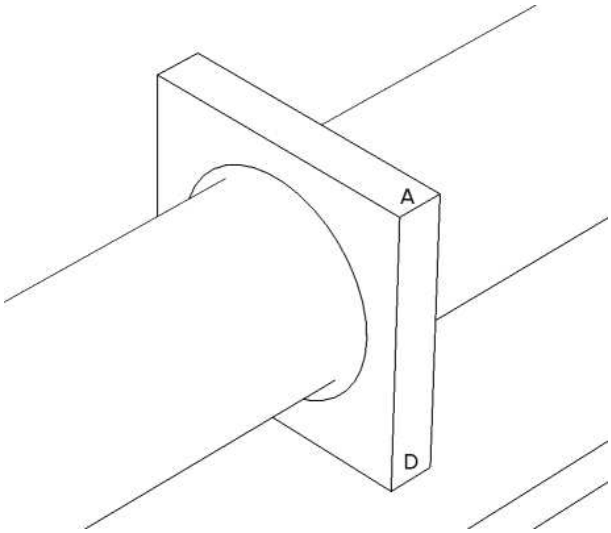

Fig. 49. Faces of the loading ring

This sequence was utilized for the seven specimens.

The raw data of one of these tests is presented in Appendix C.

3. Aluminum specimen

In order to determine the machine compliance, an eighth specimen was conditioned and tested. This last specimen was a tube extruded from 3003 aluminum alloy and the loading ring and end caps made up of 6061 aluminum alloy were bonded to it as done for the carbon/epoxy specimens, as shown in Figure 50. When using aluminum as the base material for the cylinder we can be sure about the mechanical properties and no error due to this calculation can be introduced. Also, the use of aluminum facilitates the comparison between a closed form solution for the maximum

displacement at the midspan and the finite element results.

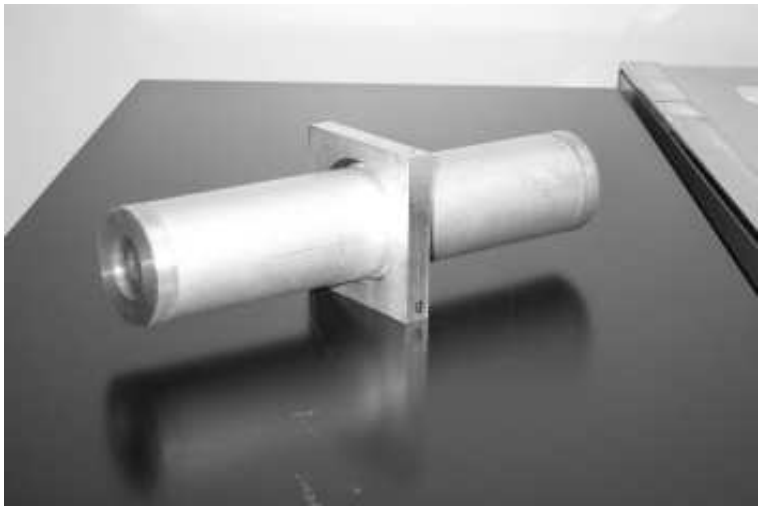

Fig. 50. 3003 aluminum specimen

CHAPTER IV

RESULTS

In this chapter we present the results of the experimental testing of the seven composite tubes.

A. Experimental results

1. Midspan deflections

The load cell output was automatically converted to axial load and axial displacement by the testing machine software. The load is expressed in Newtons and the displacement in inches. A conversion factor is used to get the load values in lbf.

The crosshead speed used for the testing was 0.002 in/min. Before the beginning of each test the load values oscillate around zero and they grow when the load application is started, so in order to identify the beginning of the test, careful examination of the load readings are made. Figure 51 shows the raw data including the initial oscillations.

Plots of load vs displacement for each test were generated up to a total of twenty four. A typical load vs displacement plot is presented in Figure 52.

Linear trend lines for each of these plots were inserted to determine the slope of the load vs displacement curve. Because data for tests performed using each face (A, B, C and D) of the loading ring were recorded for each specimen, a total of four plots per specimen were generated.

These data turned out to be reasonably consistent, no significant difference exists among the flexural behavior of the three $[0/90]_4$ specimens.

The stiffness to weight ratio for all the specimens was calculated. The heaviest

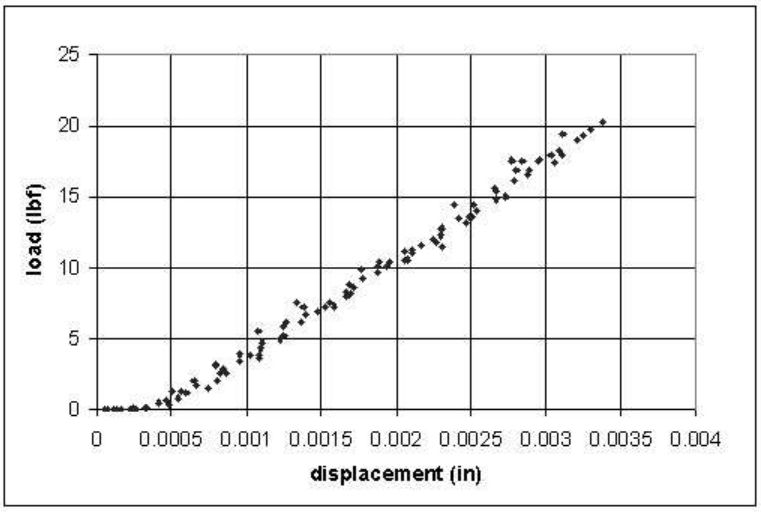

Fig. 51. Load vs displacement plot to identify test starting

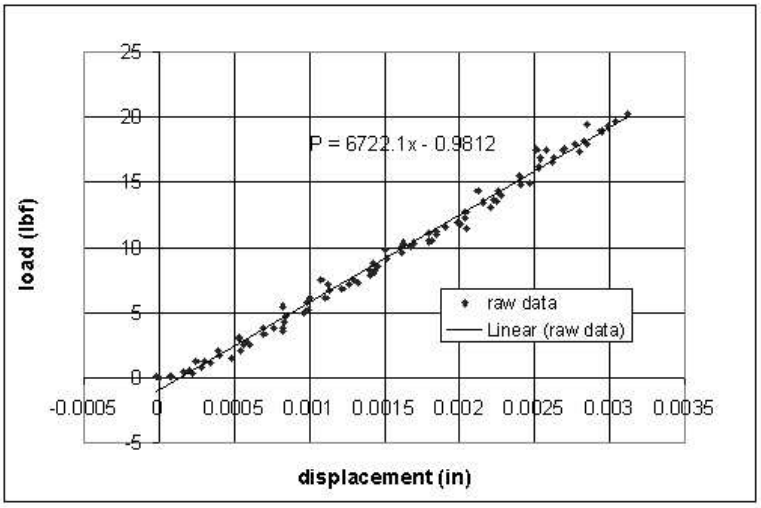

Fig. 52. Load vs displacement for raw data specimen 2 [0/90]4 face D

specimen was the $[0/90/45/-45]_s$. This agrees well with the experiments because this specimen turned out to be the stiffest one too. Table XVIII presents the specific stiffness for all the specimens tested.

Table XVIII. Specific stiffness from experimental results

ID #	**Layup**	**Mass (lbs)**	**Stiffness (lbf/in)**	**specific stiffness (lbf/(lb-in))**
2	$[0/90]_4$	0.0999	7208.375	72156
3	$[0/90]_4$	0.0934	7194.4	77028
4	$[0/90]_4$	0.0996	7527.35	75576
5	$[0/90]_3$	0.0761	6883.2	90450
6	$[0/90]_2$	0.0493	5373.2	108990
7	$[0/90/45/-45]_s$	0.103	7856.9	76280

Figure 53 shows the load vs displacement curves for the three $[0/90]_4$ and the $[0/90/45/-45]_s$ specimens and Figure 54 shows the load vs displacement curves corresponding to the $[0/90]_2$ and $[0/90]_3$ specimens. The highest slope value corresponds to the $[0/90/45/-45]_s$ specimen and the smallest one is for the $[0/90]_2$ specimen. Figure 55 shows the data from the four tests performed to specimen #2 $[0/90]_4$.

The $[0/90]_2$ specimen was tested at 10 lbs and 20 lbs.

2. Noise filtering

Some noise has been identified in the raw data. To improve this situation and minimize the error in the load readings taken from the load cell, a lowpass filter was applied during postprocessing. For each value of load at a specific time step, the next

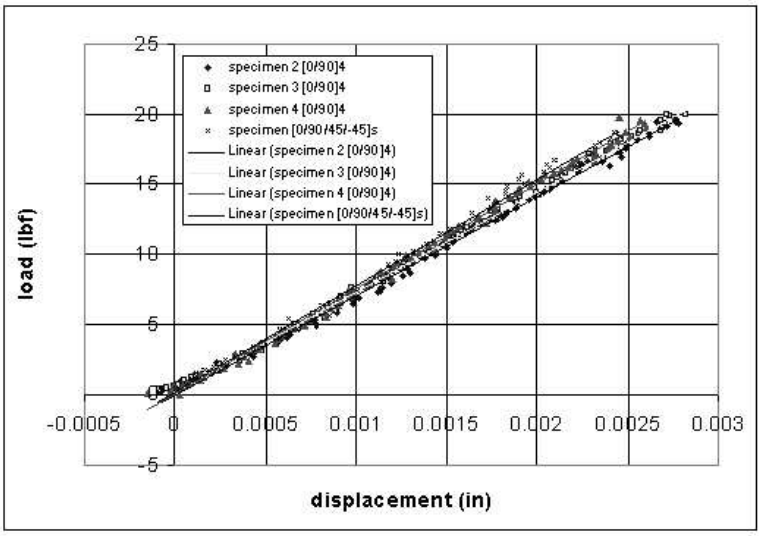

Fig. 53. Load vs displacement curves for $[0/90]_4$ and $[0/90/45/-45]_s$ specimens

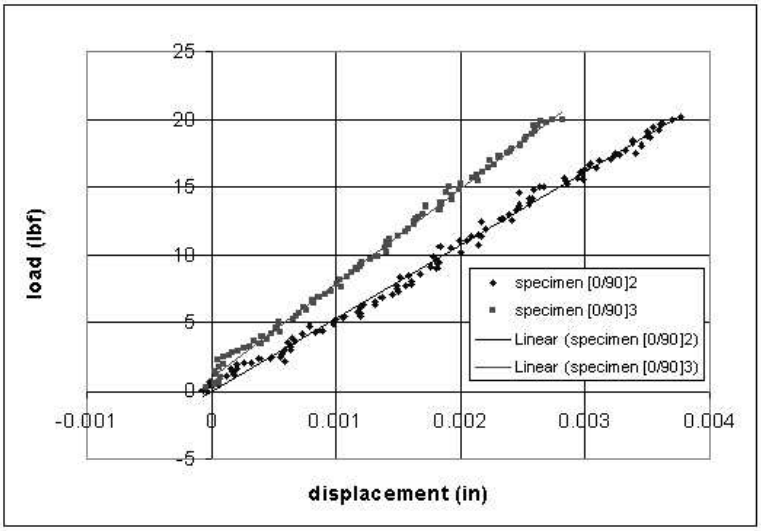

Fig. 54. Load vs displacement curves for $[0/90]_2$ and $[0/90]_3$ specimens

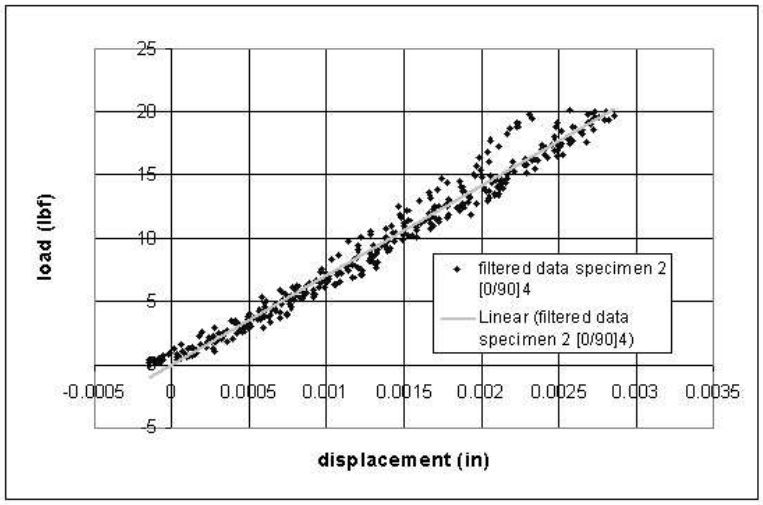

Fig. 55. All tests performed on specimen 2 $[0/90]_4$

equation was applied to get a filtered value:

$$\bar{P}_i = \frac{\sum_{i=1}^{i+3} P_i}{4} \tag{4.1}$$

where: $\bar{P}_i$ is the filtered load value, and P_i is the load value before filtering

New values of load were calculated. With these new values of load, a new load vs displacement plot was created. This is plotted in the same graph as the load values containing noise to see the difference. See Figure 56. We can appreciate that the error is reduced.

The toe region in a typical load vs displacement curve that does not represent a property of the material and which is caused by a take up of slack and alignment can be removed as shown in Figure 57.

Once the toe region has been removed from the load vs displacement plot we must find out the intersection of the linear portion of the load vs displacement curve with the zero-load axis. This intersection is the corrected zero deflection point from which all deflections must be measured. For this purpose a linear least squares solution is

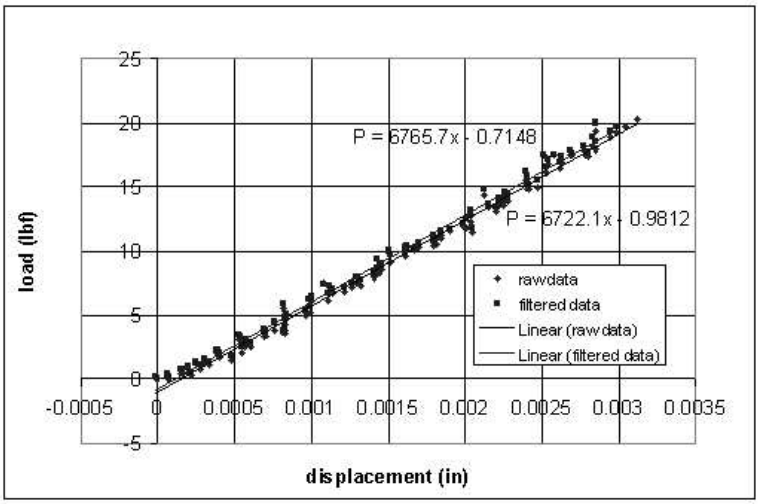

Fig. 56. Load vs displacement for raw and filtered data specimen 2 $[0/90]_4$ face D

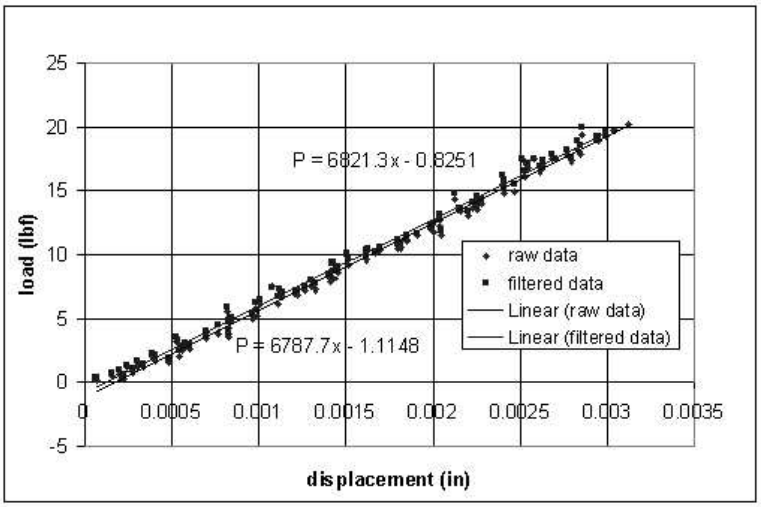

Fig. 57. Toe region removed for specimen 2 $[0/90]_4$ face D

superimposed and the intersection of each plot with the zero-load axis is found. The correction just made brings the data near to a line that passes through the origin, in this way a displacement of zero value corresponds to not load applied. This is shown in Figure 58 and Figure 59.

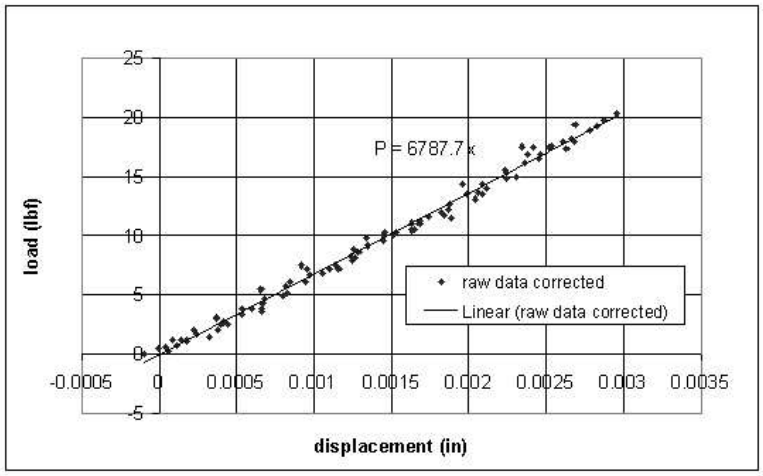

Fig. 58. Raw data corrected for specimen 2 $[0/90]_4$ face D

Once this has been done, a plot showing the difference between corrected filtered data and corrected raw data is constructed and shown in Figure 60.

We can appreciate that the slopes of these two lines are very close. This demonstrates the validity of applying a low pass filter to get rid of the noise and minimize the error in the readings.

This analysis has been performed for each one of the 24 tests, and in particular, Figure 61 shows the comparison among the corrected filtered data resulting from the twelve tests (faces A, B, C and D of each $[0/90]_4$ specimen) performed to the three $[0/90]_4$ specimens.

It is important to mention that this model, in which the linear least squares solution is used to approximate the slope of the load vs displacement curve, is only

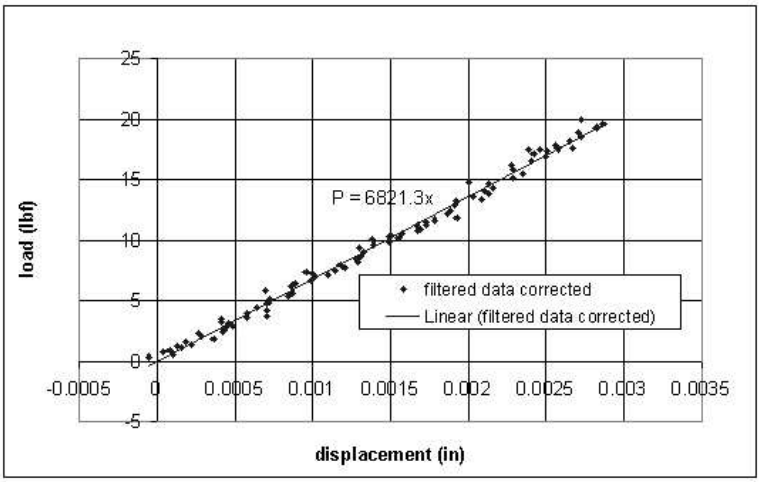

Fig. 59. Filtered data corrected for specimen 2 $[0/90]_4$ face D

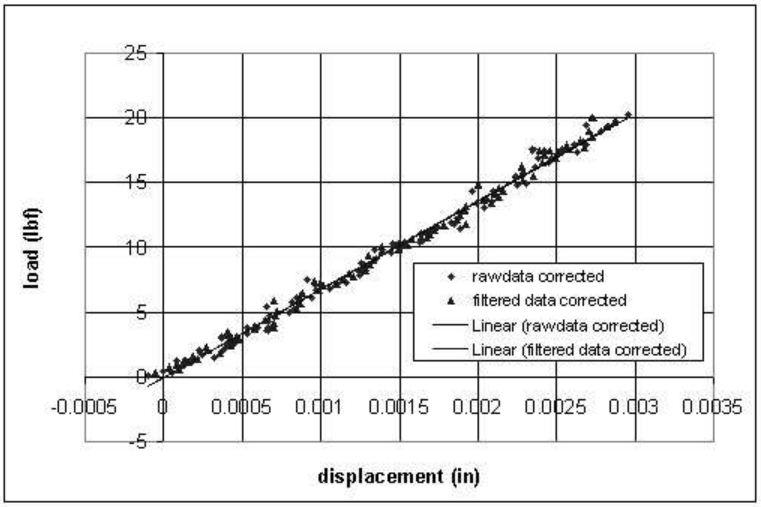

Fig. 60. Load vs displacement plots comparison between raw and filtered data corrected for specimen 2 $[0/90]_4$ face D

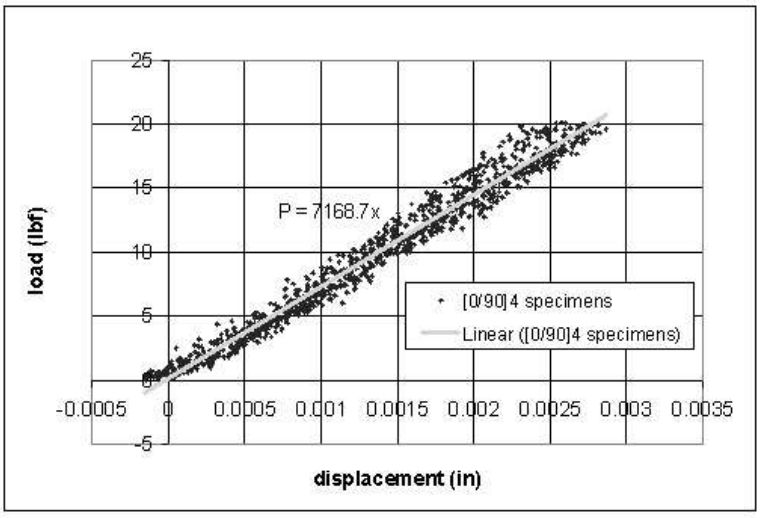

Fig. 61. All tests performed to the three $[0/90]_4$ specimens

valid for small loads. 10 lbs and 20 lbs were used for these tests.

3. Statistical analysis of $[0/90]_4$ specimens

With the data from the twelve tests performed to the three $[0/90]_4$ specimens, two of the most common sample statistics have been computed: the sample mean and the sample standard deviation.

As a central tendency measure, the mean determines where the middle of the data is.

The mean is calculated by using the next formula:

$$\bar{x} = \frac{\sum x}{n} \tag{4.2}$$

where:

$\bar{x}$ is the arithmetic mean of the sample,

x is the value of a single observation, and

n is the number of observations in the sample

On the other hand, to measure how scattered the data are, we use the standard deviation, which can be calculated from:

$$s = \sqrt{\frac{\sum(x - \bar{x})^2}{n - 1}} \tag{4.3}$$

where:

s is the sample standard deviation,

$\bar{x}$ is the arithmetic mean of the sample,

x is the value of a single observation, and

n is the number of observations in the sample

The corresponding values of arithmetic mean and standard deviation of the sample of twelve stiffness values taken from the testing of the three $[0/90]_4$ specimens turned out to be 7310.042 lbf/in and 432.47 lbf/in respectively.

We can perform an additional analysis of the data by doing an estimation of the population parameters. This is done by using the central limit theorem, which states the following:

If large random samples of a fixed size (n$\geq$30) are taken from a numerical population, and if a sample mean $\bar{x}$ is computed for each sample, the distribution of sample means $\bar{x}$ is closely approximated by a normal curve whose mean is the mean of the population itself:

$$\mu_{\bar{x}} = \mu \tag{4.4}$$

and whose standard deviation (denoted $\sigma_{\bar{x}}$) is the population standard deviation σ divided by the square root of the sample size [15].

$$\sigma_{\bar{x}} = \frac{\sigma}{\sqrt{n}} \tag{4.5}$$

The above theorem is true when dealing with large samples.

A small sample as ours (n≤30), n=16 for our case can be analyzed but not with the usual normal curve approach. With (n≤30), sample means $\bar{x}$ are not guaranteed to be normally distributed. The curve which approximates the behavior of small samples is known as the t-curve or the t-student's distribution. Figure 62 shows a t-student distribution with 10 degrees of freedom. The left portion of the curve represents the probability P(t>1.812) = 0.05, and the right portion of the curve represents the probability P(t<-1.812) = 0.05

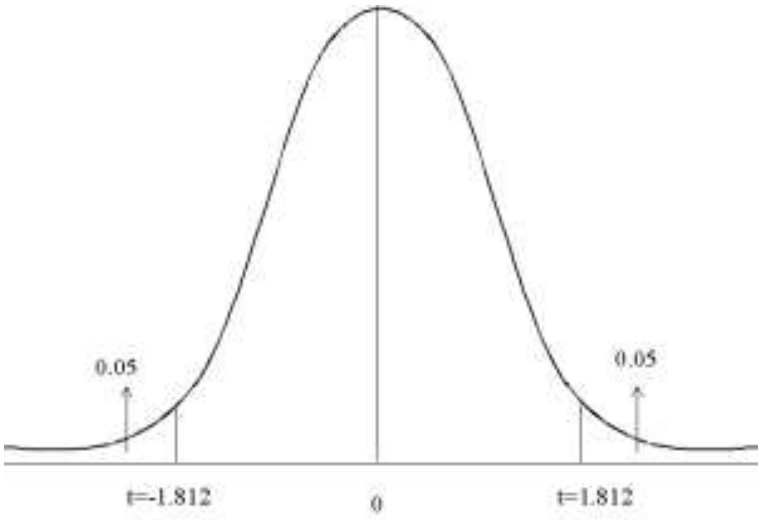

Fig. 62. The t-student distribution with 10 degrees of freedom

Figure 63 shows the $[0/90]_4$ specimens stiffness data from testing approximated by a t-student distribution.

The numbers in the horizontal axis of the plot above correspond to stiffness intervals as shown in table XIX.

The procedure is as follows: with a small sample size we construct a confidence

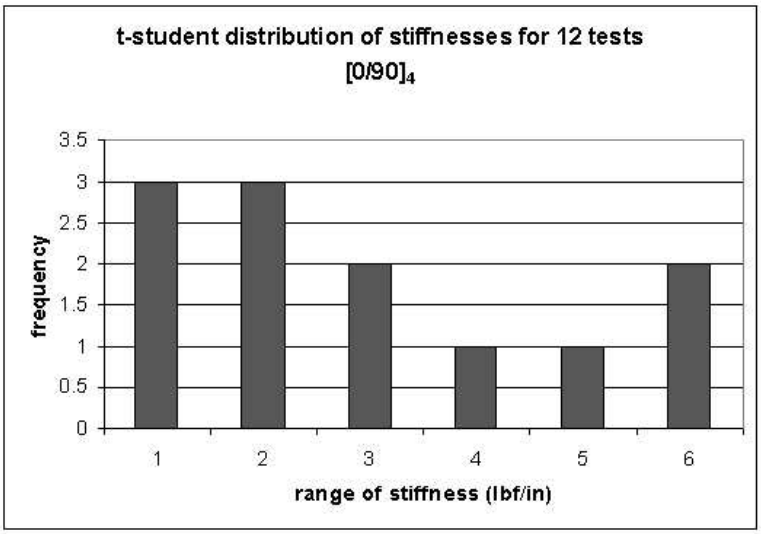

Fig. 63. $[0/90]_4$ specimens stiffness data from testing approximated by the t-student distribution

Table XIX. Stiffness intervals for the t-student distribution

ID #	**Interval of stiffness (lbf/in)**
1	up to 7029.52
2	7029.52 - 7237.73
3	7237.73 - 7445.95
4	7445.95 - 7654.17
5	7654.17 - 7862.38
6	7862.38 - 8070.6

interval for μ using the equation:

$$\bar{x} - (t - value)\frac{s}{\sqrt{n}} < \mu < \bar{x} + (t - value)\frac{s}{\sqrt{n}} \tag{4.6}$$

and we get a t-value from tables for the computations. The t-value depends on the the sample size and the confidence level desired. A confidence interval of 95% is desired.

The confidence interval is which we can feel is 95% likely to contain the true value of μ. To do so, first we note that under the t-curve, 95% of the area lies within z=2.201 and z=-2.201, or 2.201 standard deviations of the mean [15]. The area beyond these values (right or left) is 0.0250. We should remember that, because of the theoretical nature of the normal and t-curve, the total area under these curves is one square unit.

Then we use the calculated mean value of 7310.042 lbf/in as the midpoint of the interval to be constructed, and obtain the right and left endpoints of the interval by adding and subtracting 2.201 standard deviations, where the appropriate standard deviation was given by equation 4.3.

To retrieve the required t-value from tables we made use of the degrees of freedom, defined as:

$$d.f. = (sample\ size) - 1 \tag{4.7}$$

Then with the d.f. value of 11 and using the column $t_{0.025}$ to get 95% confidence in the t-distribution table (see Appendix D) we get a t-value of 2.201 as listed above.

The confidence interval desired will have:

left endpoint=$\bar{x}$-274.7801=7035.2618

right endpoint=$\bar{x}$+274.7801=7584.8222

so that (before round-off) we have:

$$7035.2618 < \mu < 7584.8222$$

and rounding these points to three places (in such a way as to widen the interval), the final result is

$$7035.262 < \mu < 7584.822 \tag{4.8}$$

which is the interval 95% likely to contain the population mean μ.

B. Analytical results

Table XX shows the effective modulus of elasticity $\bar{E}_x$ calculated using lamination theory for each of the studied layups. This table includes also the moment of inertia of the cross-sectional area for each configuration, the corresponding tube thickness, as well as the extensional compliances a_{xx} used in equation 1.8 to get the effective moduli $\bar{E}_x$.

Table XXI shows the resulting bending stiffnesses using the smear property approach and the laminated plate approach for the four different layups under study.

Table XX. Effective moduli from lamination theory

Layup	**thickness (in)**	a_{xx}	**Effective** $\bar{E}_x$ **(psi)**	**I** (in^4)
$[0/90]_4$	0.037	3.20E-06	8.438E6	0.1194
$[0/90]_3$	0.02772	4.397E-6	8.2045E6	0.08752
$[0/90]_2$	0.01848	7.21E-6	7.5094E6	0.05802
$[0/90/45/-45]_s$	0.037	4.47E-6	6.0477E6	0.1194

Table XXI. Bending stiffness from closed form solution

Bending stiffness ($lb - in^2$)			
Layup	**Smear property approach**	**Plate approach**	**% difference**
$[0/90]_4$	1007888.305	1021156.270	1.29
$[0/90]_3$	718025.394	755325.568	4.94
$[0/90]_2$	435666.25	496600.866	12.27
$[0/90/45/-45]_s$	722368.816	699998.341	3.09

C. Discussion

In order to compare the model with the test articles, it was necessary to correct for machine compliance, including that associated with the test fixture.

After performing the comparison between finite element results and a simple hand calculation based on engineering beam theory for the $[0/90]_4$ specimen, it was seen that the numerical values were in the same order of magnitude for both approaches, but a considerable difference was still present.

Then, due to the variety of components in the test article and the testing fixture, after an examination of all these components, it was decided to make a rough calculation of the deflection of the fixture and the attachments of the tube. It was seen that all the parts made of aluminum alloy 6061 defomed a few tenths of a thousand of an inch, therefore suggesting to perform a closer examination of the spherical bearings.

The spherical bearings used in the test fixture have their outer rings fractured axially in one place parallel to their axes to permit assembly of the bearing spheres. This gap can be easily opened when a small force is applied. A special sub-fixture

to test the spherical bearing was designed and then screwed to the testing fixture. Figure 64 shows the spherical bearing mounted for testing.

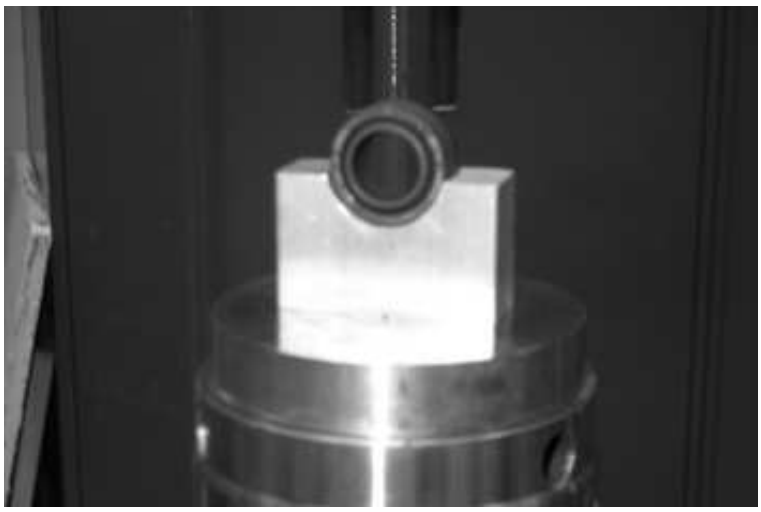

Fig. 64. Spherical bearing in testing fixture

The bearing was tested in compression and a load of 10 lbs was applied. Because the total load applied at the midspan is 20 lbs, each support is subjected to half this value. The results from testing showed that the overall u_y deflection of the bearing was approximately 0.001375", a number large enough to deviate the results from the bending test of the 3003 aluminum alloy tube or the six composite specimens.

With this result, and based on the $[0/90]_4$ specimens tested, a correction factor between the experimental results and the FEA results was determined. This correction factor included the deflection of the spherical bearing as well as the deflection of the remainder fixture. This factor was calculated to be 0.00187172".

If we subtract this constant factor from each one of the experimental results we obtain deflection values which are within a 10% of difference from the FEA prediction for all the specimens. The maximum u_y displacements of the top face of the loading ring at the midspan predicted by the FEA model and the ones from the experimental

results, as well as the corrected values are presented in Table XXII.

Table XXII. Comparison of midspan maximum deflection between experiment and finite element results

Lay-up	**Experimental (in)**	**Corrected (in)**	**FEA (in)**	**% difference**
$[0/90]_4$	0.002596	0.000725	0.0007248	0.02
$[0/90]_3$	0.002738	0.000867	0.000947	8.44
$[0/90]_2$	0.0034	0.001528	0.0013882	10.01
$[0/90/45/\text{-}45]_s$	0.002484	0.00061228	0.0006105	0.29
Al 3003	0.002298	0.00042628	0.00044	3.12

By looking at this table we can conclude that the stiffest of all the carbon/epoxy specimens has been the $[0/90/45/-45]_s$. With an applied load of 20 lbs it has just reached a maximum deflection on the top face of the ring of 0.00061".

The specimen showing the largest deflection is the $[0/90]_2$ with a maximum u_y deflection of 0.0015". Because this table has been based on the $[0/90]_4$ configuration, what means that the correction factor has been determined by subtracting the deflection from the FEA results from the deflection from the experimental testing in the $[0/90]_4$ specimens, the best correlation between results corresponds to this layup.

For comparison purposes, table XXIII showing the results from the bending stiffness calculation including specific stiffness is repeated here.

From the previous table, we can see that specimens $[0/90]_4$ and $[0/90]_2$ have the best specific stiffness among all composite tubes. Because the application requires high specific stiffness, we can decide which of these configurations is more desirable depending upon the allowable deflection for a lens housing structure. If that allowable

Table XXIII. Comparison of effective bending stiffnesses from analytical solution including specific stiffnesses

	Bending stiffness ($lb - in^2$)				
Layup	**Smear property approach**	**Plate approach**	**% diff.**	**Mass (lbs)**	**specific stiffness**
$[0/90]_4$	1007888.305	1021156.270	1.29	0.0976	10.463E6
$[0/90]_3$	718025.394	755325.568	4.94	0.0761	9.925E6
$[0/90]_2$	435666.25	496600.866	12.27	0.0493	10.073E6
$[0/90/45/-45]_s$	722368.816	699998.341	3.09	0.103	6.796E6

deflection is above 0.0016", which is the corrected experimental value for the deflection of a $[0/90]_2$ specimen, we would choose this configuration because of the high specific stiffness (high stiffness and low mass); approximately half that of the $[0/90]_4$ specimen.

On the other hand, the two closed form approaches followed here produced different results. The smeared property approach does not take into account the geometry of the tube. It considers the composite as a plate, and because the resultant bending stiffness depends upon the first entry of the inverse of the [A] matrix, a_{xx}, it does not matter where the plies are located with respect to the reference plane. Let's take the case of the $[0/90/45/-45]_s$ specimen. If we change the stacking sequence to a $[45/-45/0/90]_s$, the resultant [A] and [a] matrices would be exactly the same, then a better analytical approach es desired. The laminated plate approach fits well our requirements.

The laminated plate approach takes into account the effect of the stacking sequence as well as the cylindrical geometry, so it has proved to give more accurate results without underestimating the bending stiffness as in the case of the smeared

property approach.

CHAPTER V

CONCLUSIONS

The testing fixture has several components whose individual deflection is added to the overall deflection given by the experimental result.

The specimen has some attachments bonded which also contribute to the overall deflection given by the experiments.

This tells us that an experiment in which the source of compliances is large is more difficult to correlate than one in which the source of compliances is small.

Once the source of compliances has been identified it is necessary to find the main contribution and isolate it. In this case, the bearing deflection was the main contribution to the overall deformation in the experimental scenario. A minor contribution was the deflection of the testing fixture. A hand calculation has been performed and the approximate fixture deflection turned out to be 0.0005 inches.

The FE model shows a stiffer behavior than the experimental analysis. Attention has been paid in reproducing the test boundary conditions and specimen geometry. The load has been applied taking into account the cross sectional area of the cross-head extension and the corresponding area of the aluminum ring where the load has been applied. The load has been distributed on those elements inside the contact area between loading ring and cross-head extension.

The material properties of the constituents have been investigated and care has been taken to use these constants to get a good approach of the mechanical properties of the composite system. These calculated properties have been used to develop the FE models for all carbon/epoxy specimens.

The errors introduced in the experiment could be enough to produce different results if we take into account that the displacements we are measuring are very small,

varying from 0.0007" for the $[0/90]_4$ specimens to 0.0013" for the $[0/90]_2$ specimens.

On the other hand, a manufacturing process has been investigated giving satisfactory results in quality. The seven specimens for testing were better than expected. They matched well in density and dimensions. In future research, improvement of this technique can be done to obtain more realistic flight structures.

By means of a well structured procedure and adequate facilities, the objective of producing composite tubes of aerospace quality by means of the wet hand-layup technique can be reached gradually.

CHAPTER VI

RECOMMENDATIONS

In this chapter we make some recommendations for future research.

The results presented in this study should not be taken as a standard. The reader can use them as a reference for similar specimens in dimensions and mechanical constituents.

When trying to determine mechanical properties from testing, a way of reducing the error is to follow one of the standard tests already created for the kind of material from which we try to get characteristics [16]. Unfortunately, when looking for correlation between the real structure and a model as unique as the one investigated in this work, the mentioned standards are not able to produce the desired results.

The calculation of equivalent mechanical properties for the composite system used here has been based on the approach of mechanics of materials. The point of view under which this study has been conducted is the macromechanics approach, for that reason, the effective mechanical properties obtained here are good enough for our purposes. If the analysis were performed at a very small scale, micromechanics approaches and measurements would be required to produce accurate results.

When designing a mechanical test, the experimentalist engineer should try to avoid a large number of compliance sources. This is done by reducing the number of additional components to the structure we are trying to test.

The researcher must obtain accurate values of the mechanical properties of the materials chosen for manufacture. He should get these properties directly from the supplier or the manufacturer.

REFERENCES

[1] A. E. H. Love,"On the small free vibrations and deformations of the elastic shells," *Philosophical Transactions of the Royal Society of London*, Ser. A, vol. 17, pp. 491–546, 1988.

[2] E. J. Barbero, J. N. Reddy, and J. L. Teply, "General two dimensional theory of laminated cylindrical shells," *AIAA Journal*, vol. 28, no. 3, pp. 544–553, 1988.

[3] N. J. Pagano, "Exact solutions for composite laminates in cylindrical bending," *Journal of Composite Materials*, vol. 3, pp. 398–411, 1969.

[4] S. Srinivas, "Analysis of laminated composite circular cylindrical shells with general boundary conditions," *NASA TR*, R412, 1974.

[5] J. G. Ren, "Exact solutions for laminated cylindrical shells in cylindrical bending," *Composite Science and Technology*, vol. 29, pp. 169–187, 1987.

[6] T. K. Varadan and K. Bhaskar, "Bending of laminated orthotropic cylindrical shells -An elasticity approach," *Composite Structures*, vol. 17, pp. 141–156, 1991.

[7] S. G. Lekhnitskii, *Theory of Elasticity of an Anisotropic Elastic Body*. San Francisco, CA: Holden-Day, Inc., 1963.

[8] C. Jolicoeur and A. Cardou, "Analytical solution for bending of coaxial orthotropic cylinders," *Journal of Engineering Mechanics*, vol. 120, no. 12, pp. 2556–2574, 1994.

[9] C. S. Chouchaoui and O. O. Ochoa, "Similitude study for a laminated cylindrical tube under tensile, torsion, bending, internal and external pressure. Part I: governing equations," *Composite Structures*, vol. 44, pp. 221–229, 1999.

[10] J. Q. Tarn and Y. M. Wang, "Laminated composite tubes under extension, torsion, bending, shearing and pressuring: A state space approach," *International Journal of Solids and Structures*, vol. 38, pp. 9053–9075, 2001.

[11] W. S. Chan and K. Z. Demirhan, "A simple closed-form solution of bending stiffness for laminated composite tubes," *Journal of Reinforced Plastics and Composites*, vol. 19, no. 4, pp. 278–291, 2000.

[12] I. M. Daniel and O. Ishai, *Engineering Mechanics of Composite Materials*. Oxford; New York: Oxford University Press, 1994.

[13] S. W. Tsai, *Composites Design-1986*. Dayton, OH: Think Composites, 1986.

[14] B. C. Hoskin and A. A. Baker, *Composite Materials for Aircraft Structures*. New York: American Institute of Aeronautics and Astronautics, 1986.

[15] D. R. Burleson, *Elementary Statistics*. Cambridge, MA: Winthrop Publishers, Inc, 1980.

[16] ASTM D-790, "Standard test methods for flexural properties of unreinforced and reinforced plastics and electrical insulating materials," *ASTM International*, 2000.

Supplemental Sources Consulted

FEMAP Version 8.1, *Commands*. Exton, PA: Structural Dynamics Research Corp, 2001.

FEMAP Version 8.1, *User Guide*. Exton, PA: Structural Dynamics Research Corp, 2001.

H. S. Jing and K. G. Tzeng, "Elasticity solution for laminated anisotropic cylindrical panels in cylindrical bending," *Composite Structures*, vol. 30, pp. 307–317, 1995.

H. Kopka and P. W. Daly, *A Guide to LATEX*. Harlow, England: Pearson Education, 1999.

O. O. Ochoa and J. N. Reddy, *Finite Element Analysis of Composite Laminates*. Dordrecht, Boston: Kluwer Academic Publishers, 1992.

D. E. Rodriguez, "Influence of material, lay-up and geometry on the radius of curvature of spoolable composite tubulars," Master's thesis, Texas A&M University, College Station, May 2002.

APPENDIX A

FINITE ELEMENT CONTOURS

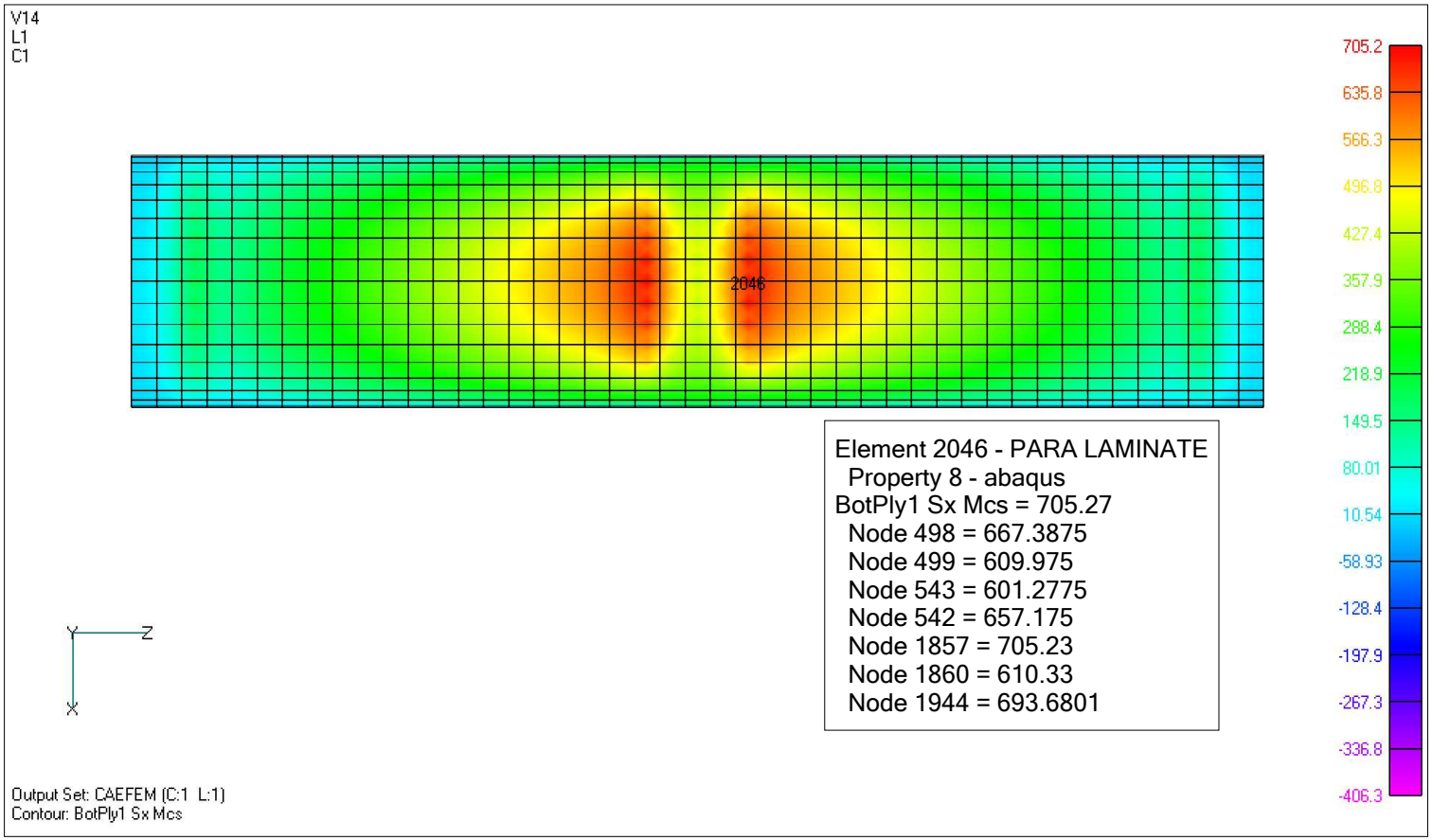

Fig. 65. Maximum stress σ_x ply 1 $[0/90]_4$

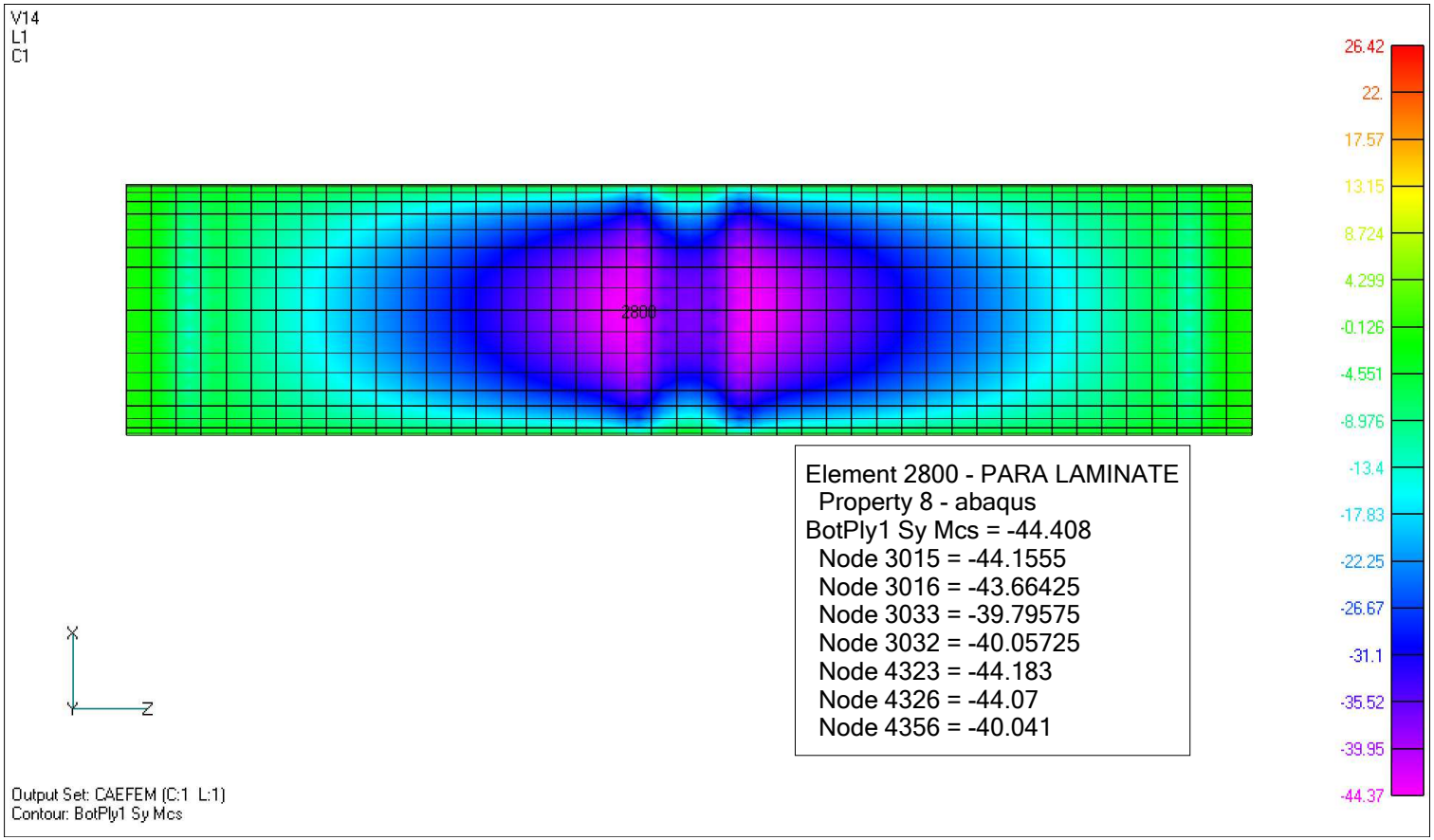

Fig. 66. Maximum stress σ_y ply 1 $[0/90]_4$

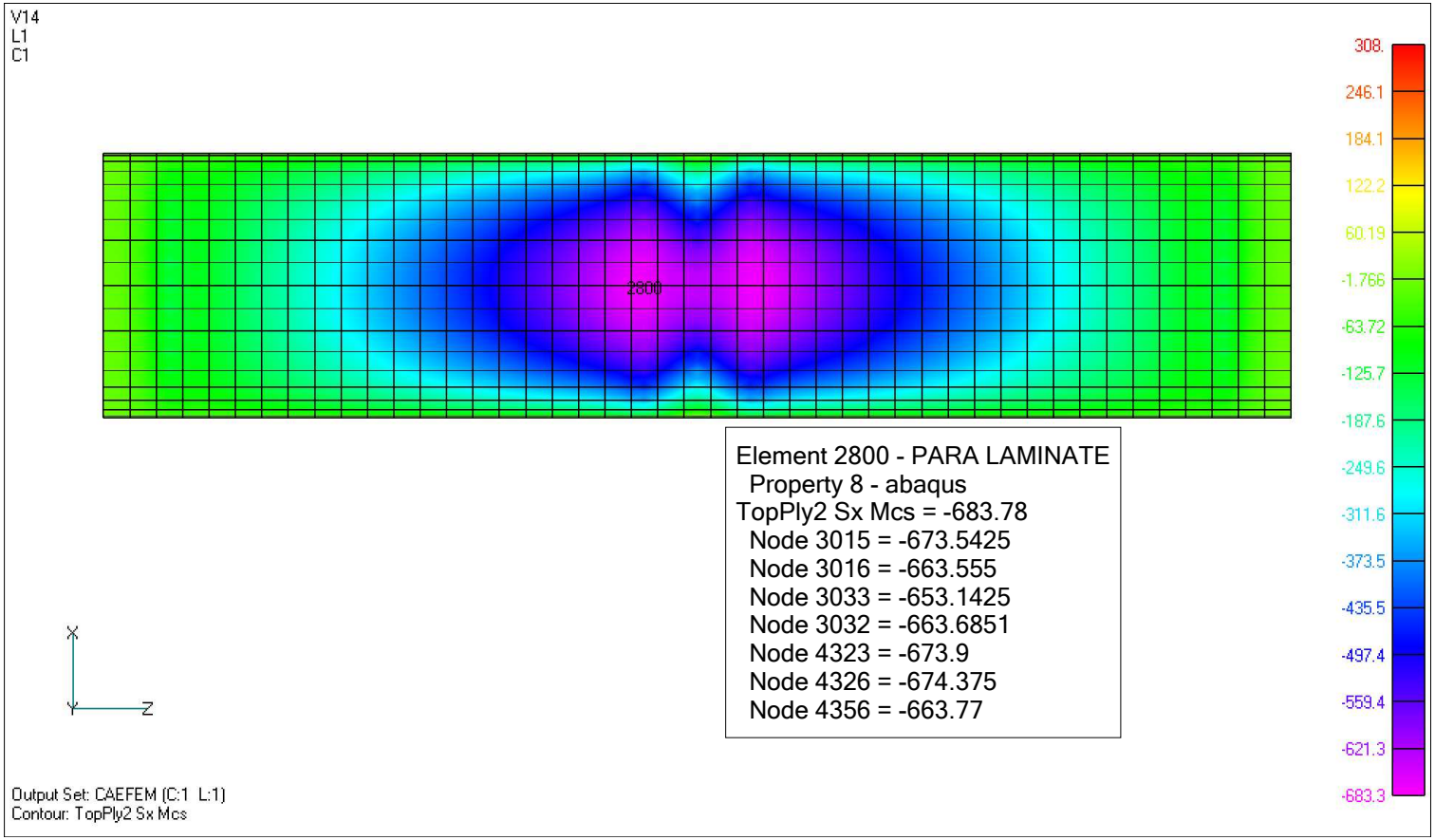

Fig. 67. Maximum stress σ_x ply 2 $[0/90]_4$

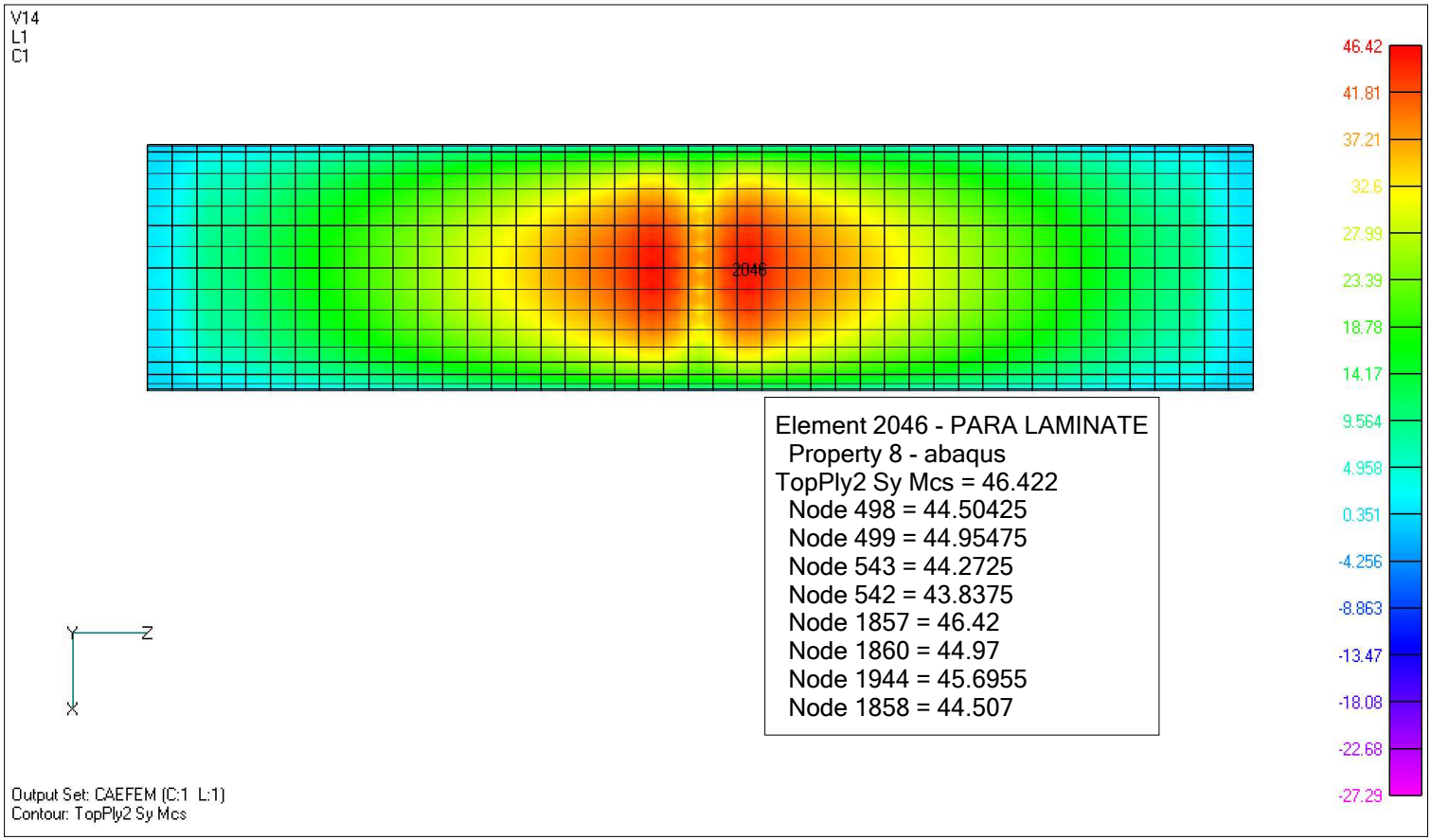

Fig. 68. Maximum stress σ_y ply 2 $[0/90]_4$

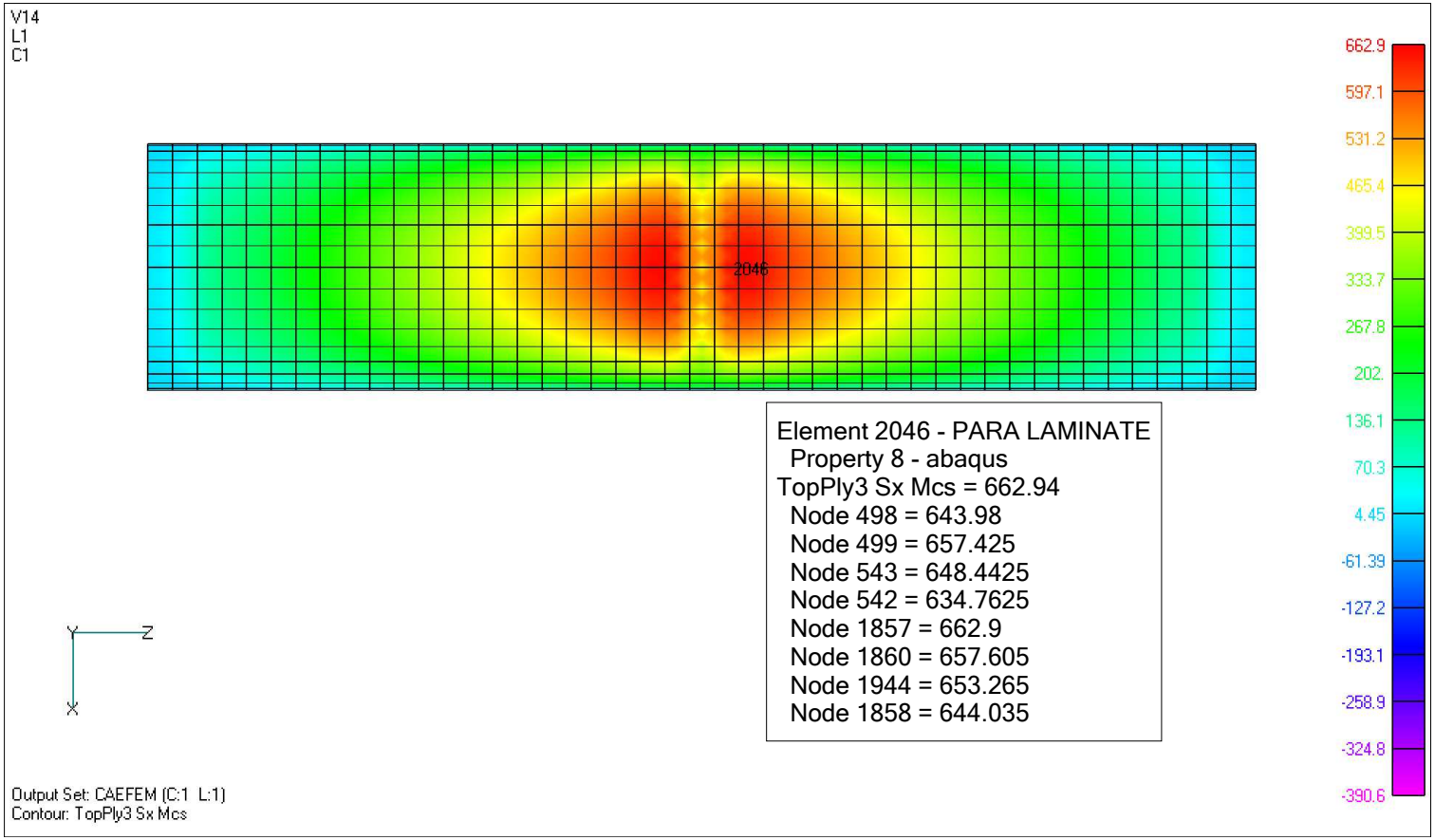

Fig. 69. Maximum stress σ_x ply 3 $[0/90]_4$

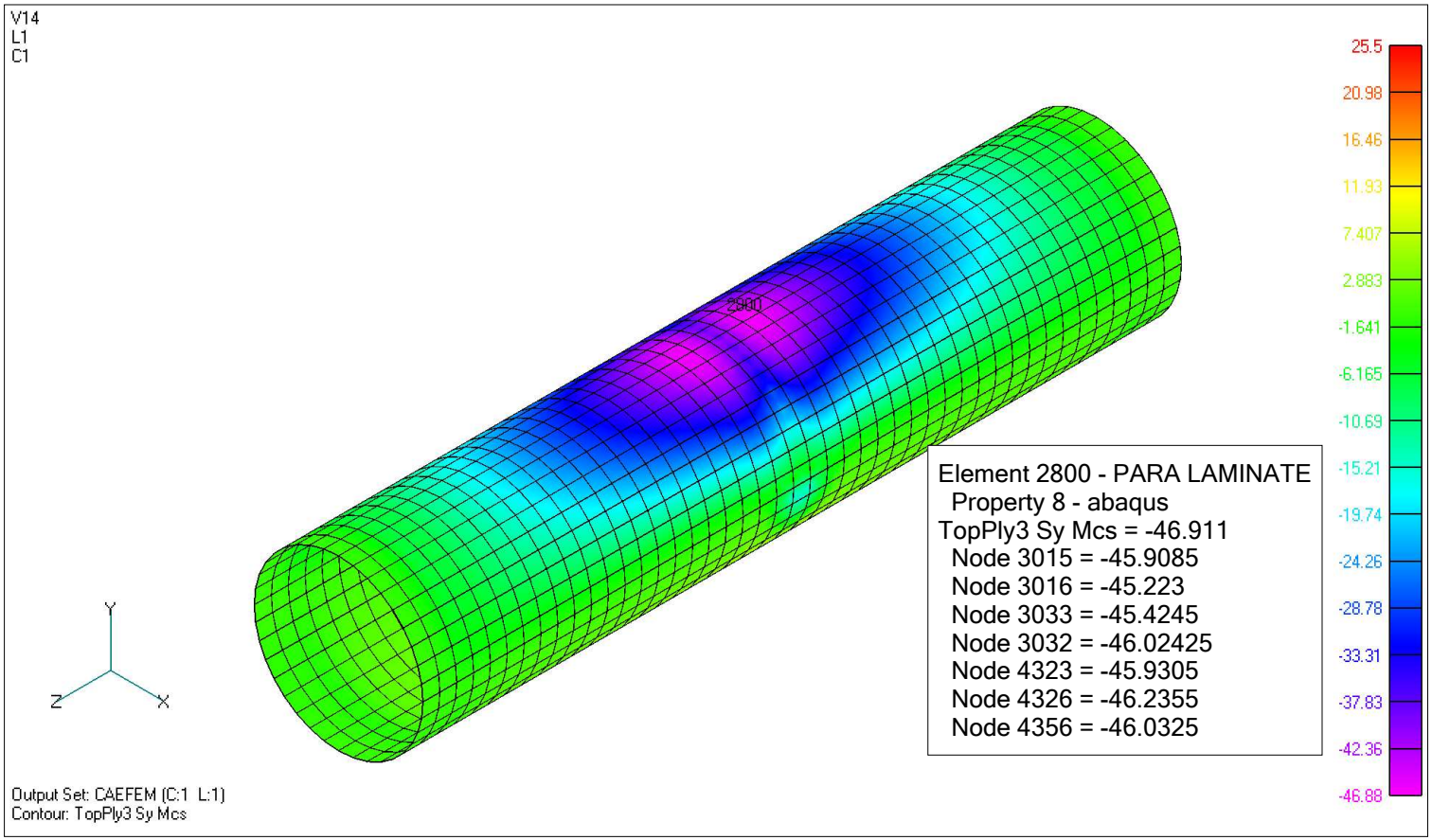

Fig. 70. Maximum stress σ_y ply 3 $[0/90]_4$

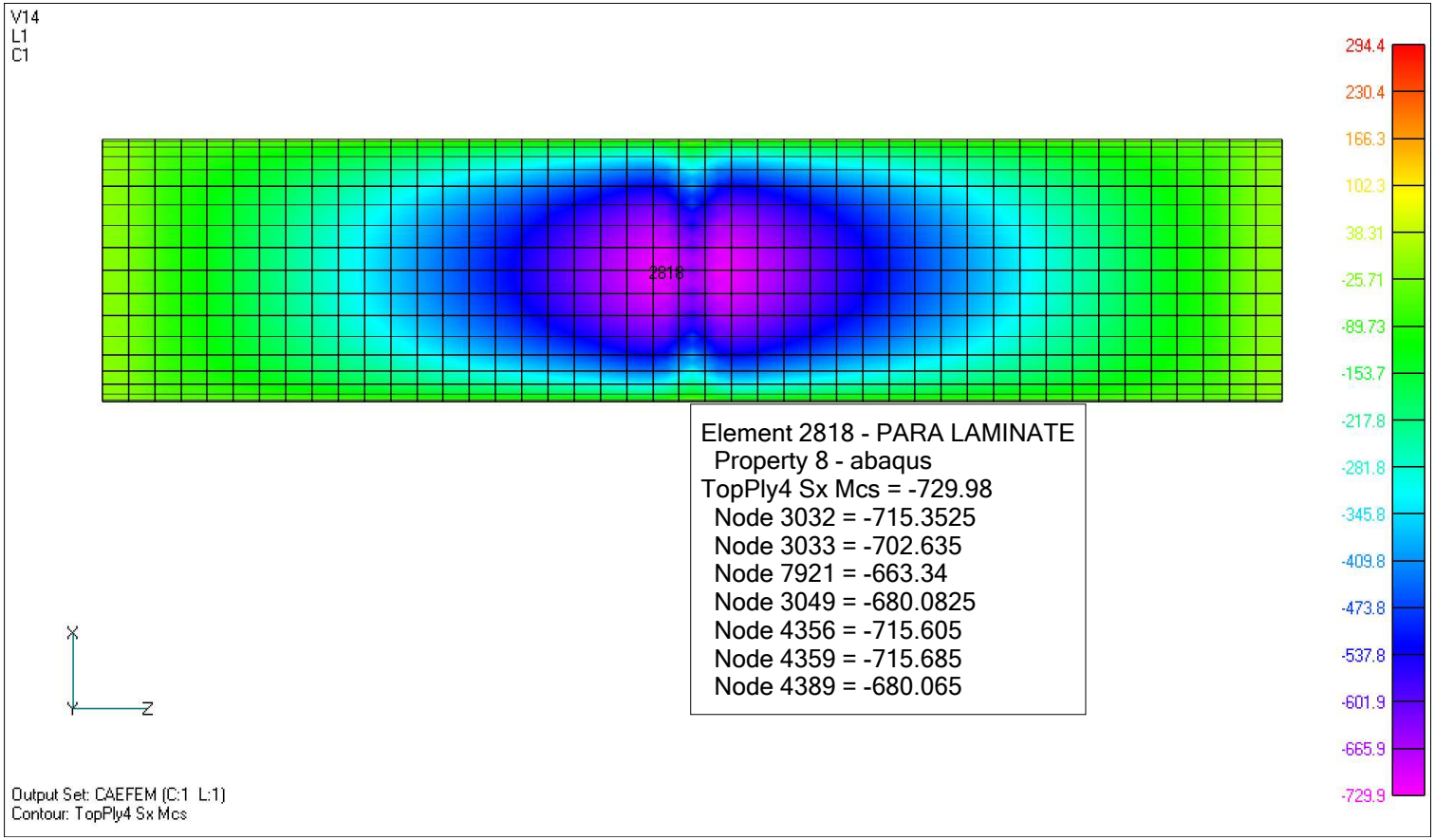

Fig. 71. Maximum stress σ_x ply 4 $[0/90]_4$

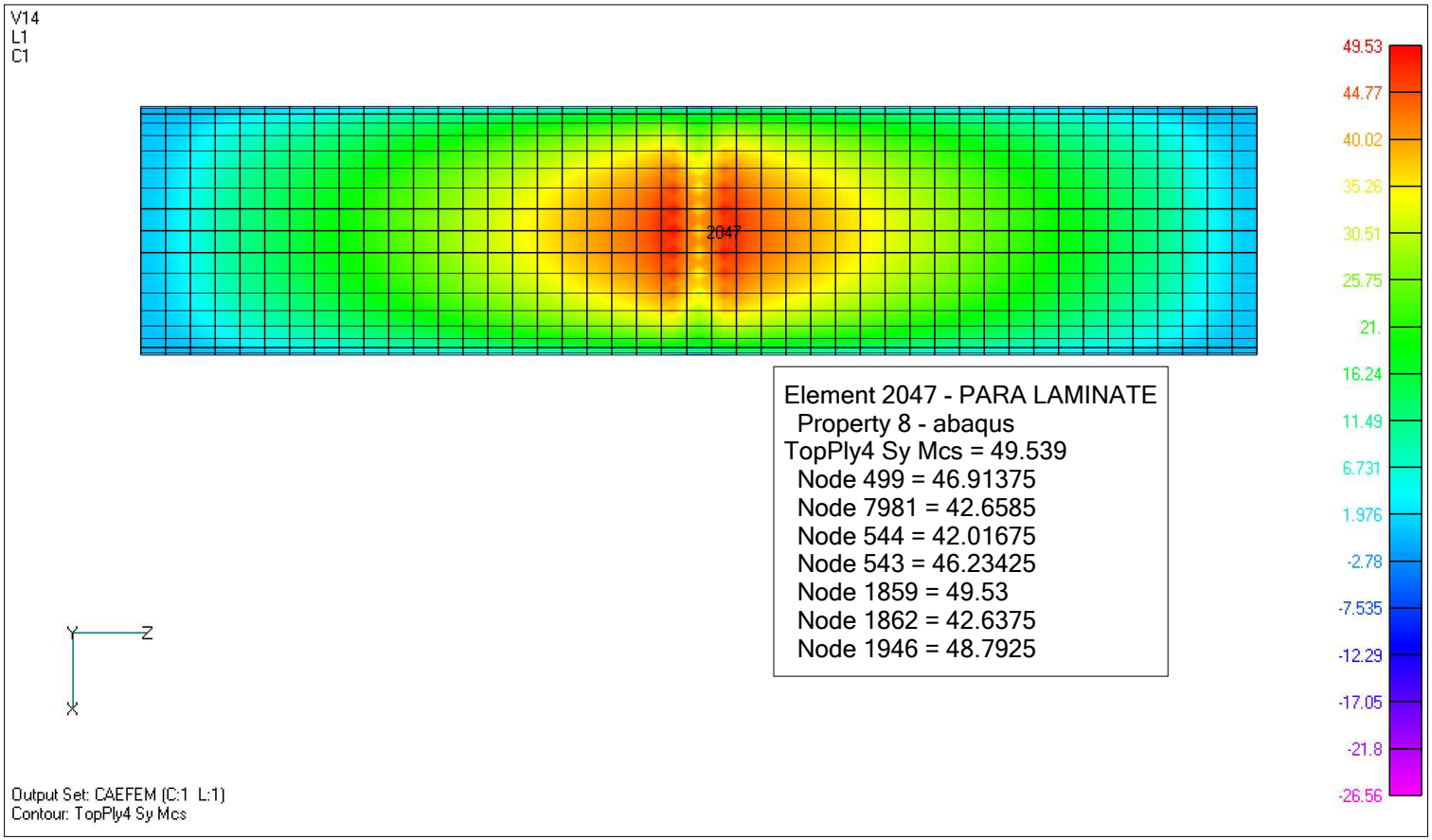

Fig. 72. Maximum stress σ_y ply 4 $[0/90]_4$

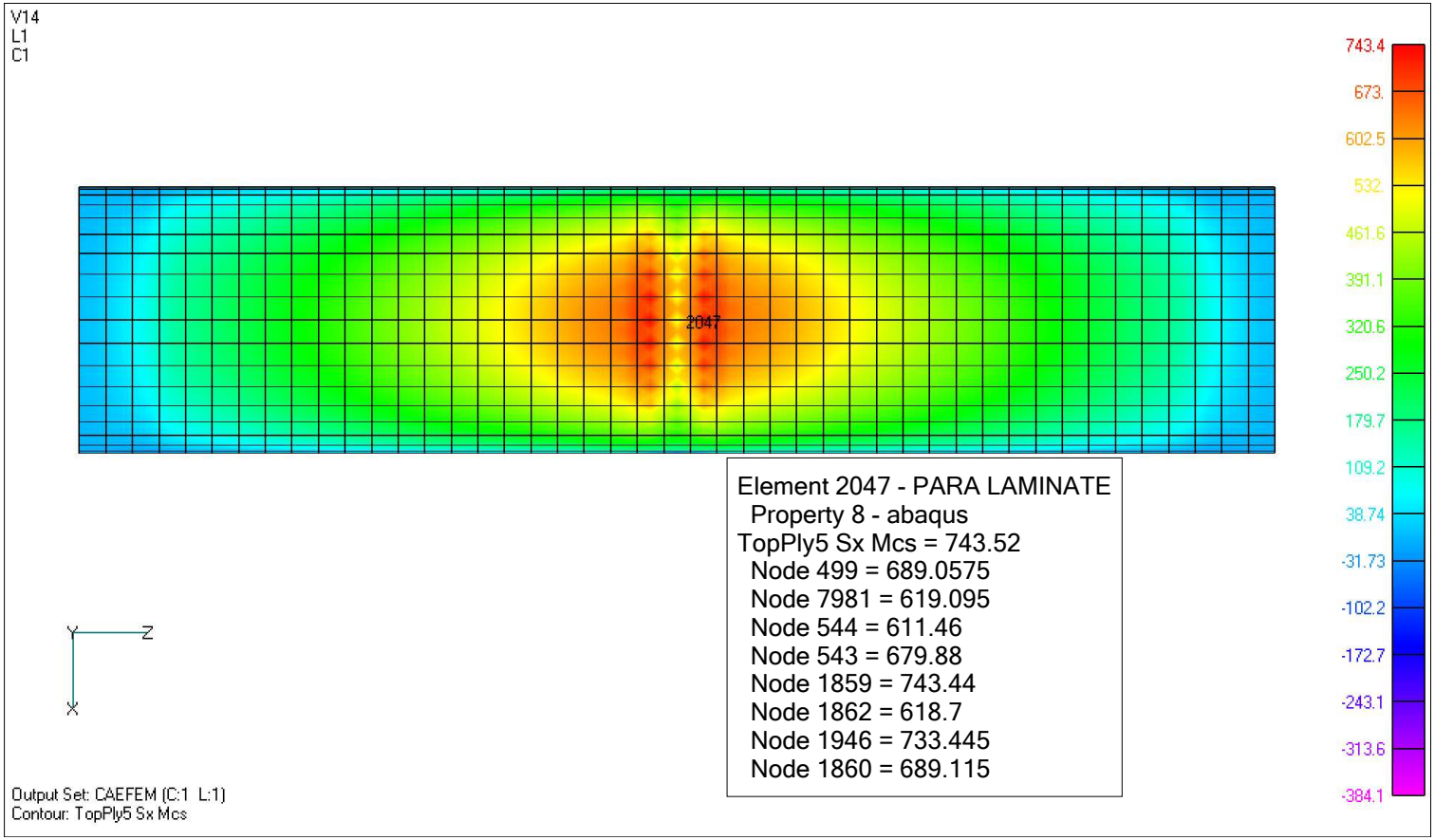

Fig. 73. Maximum stress σ_x ply 5 $[0/90]_4$

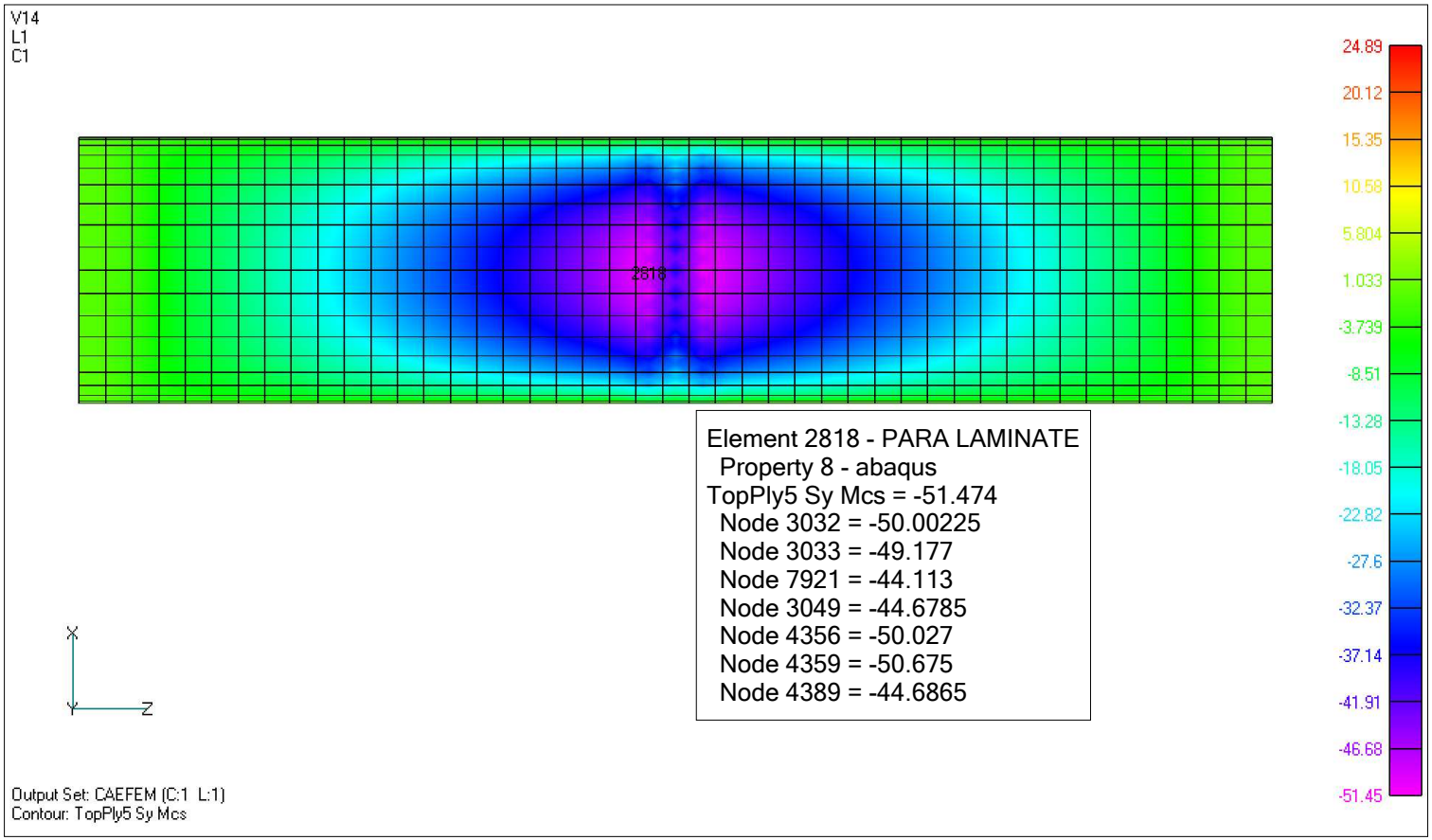

Fig. 74. Maximum stress σ_y ply 5 $[0/90]_4$

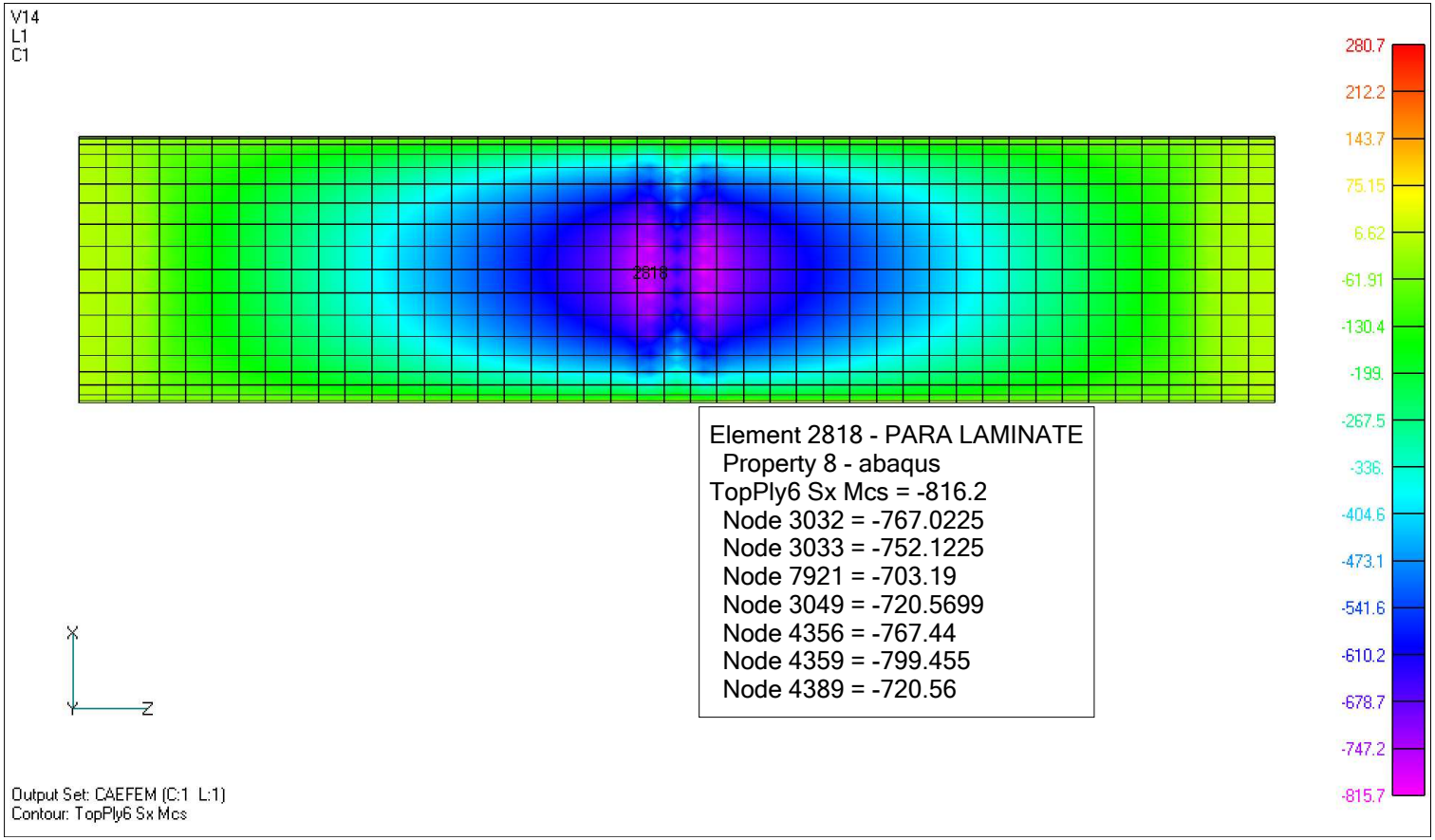

Fig. 75. Maximum stress σ_x ply 6 $[0/90]_4$

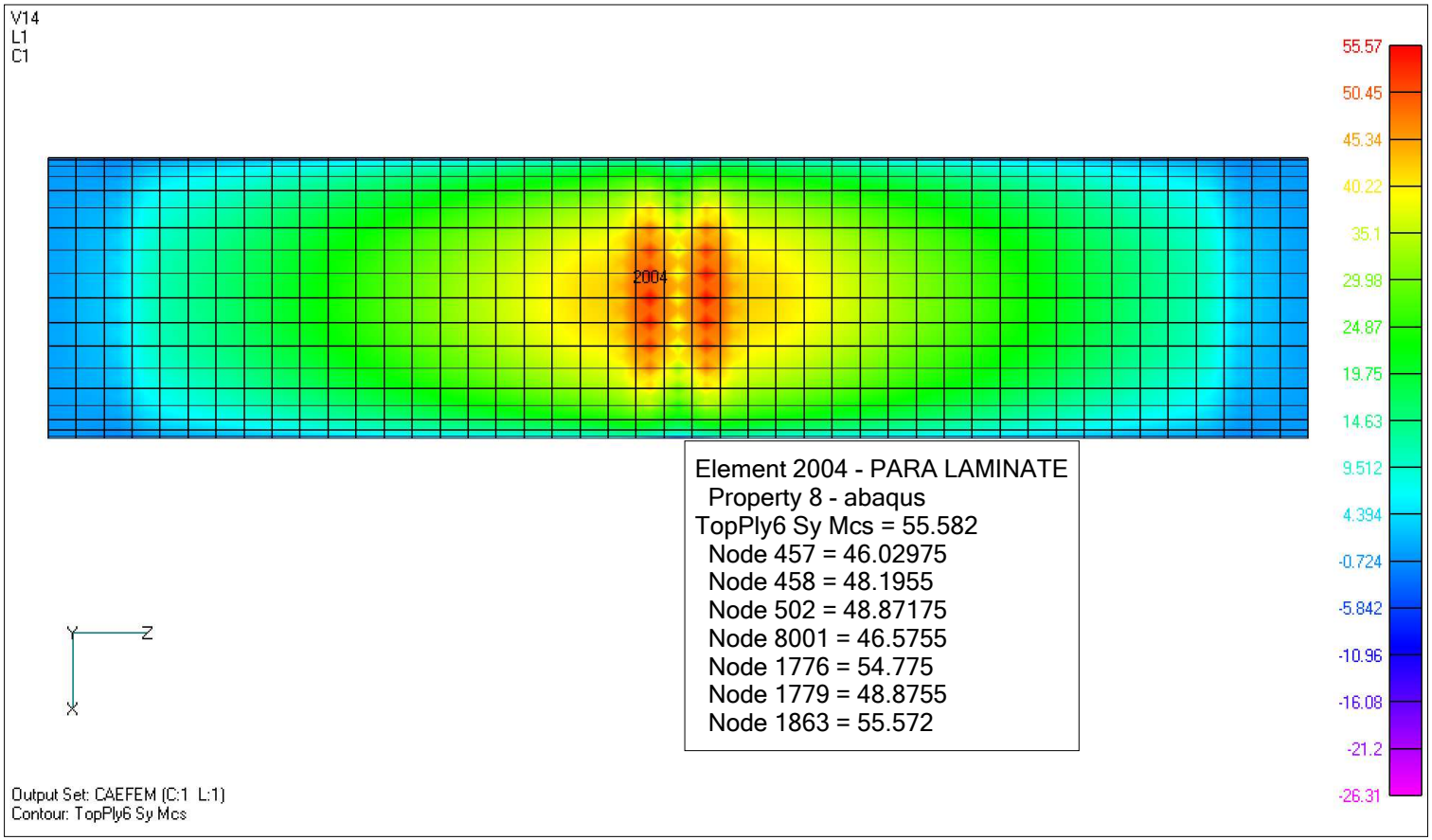

Fig. 76. Maximum stress σ_y ply 6 $[0/90]_4$

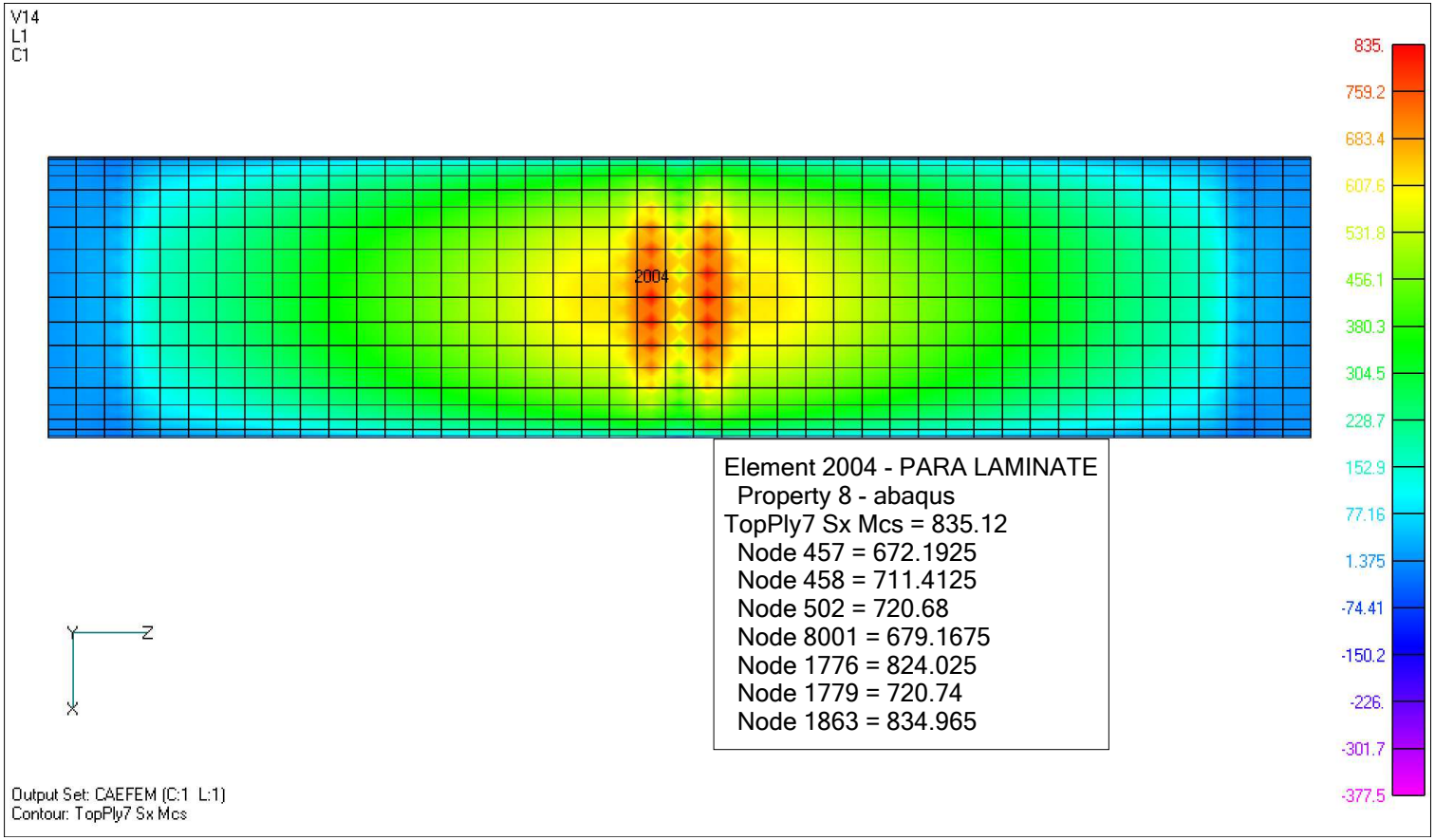

Fig. 77. Maximum stress σ_x ply 7 $[0/90]_4$

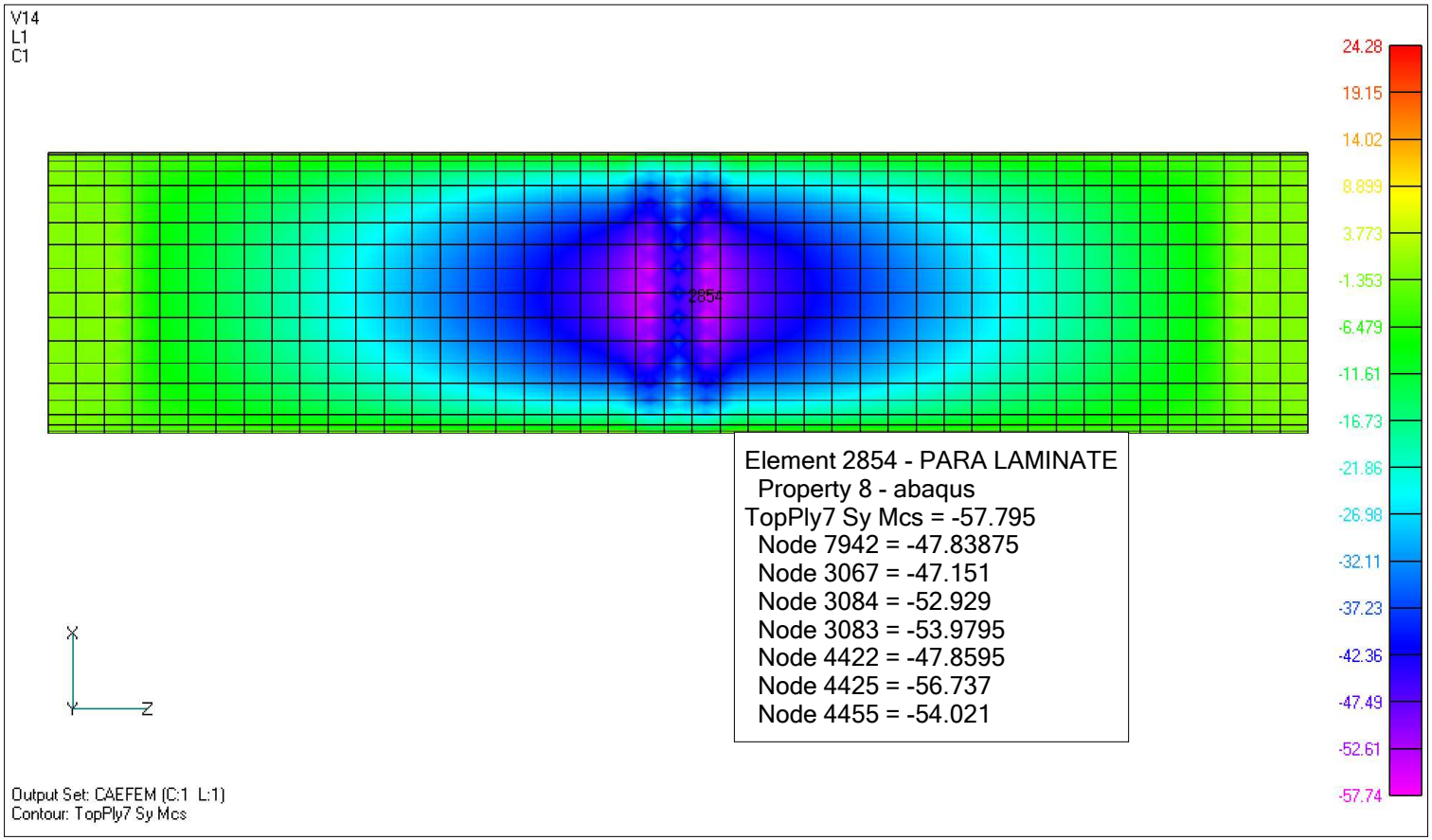

Fig. 78. Maximum stress σ_y ply 7 $[0/90]_4$

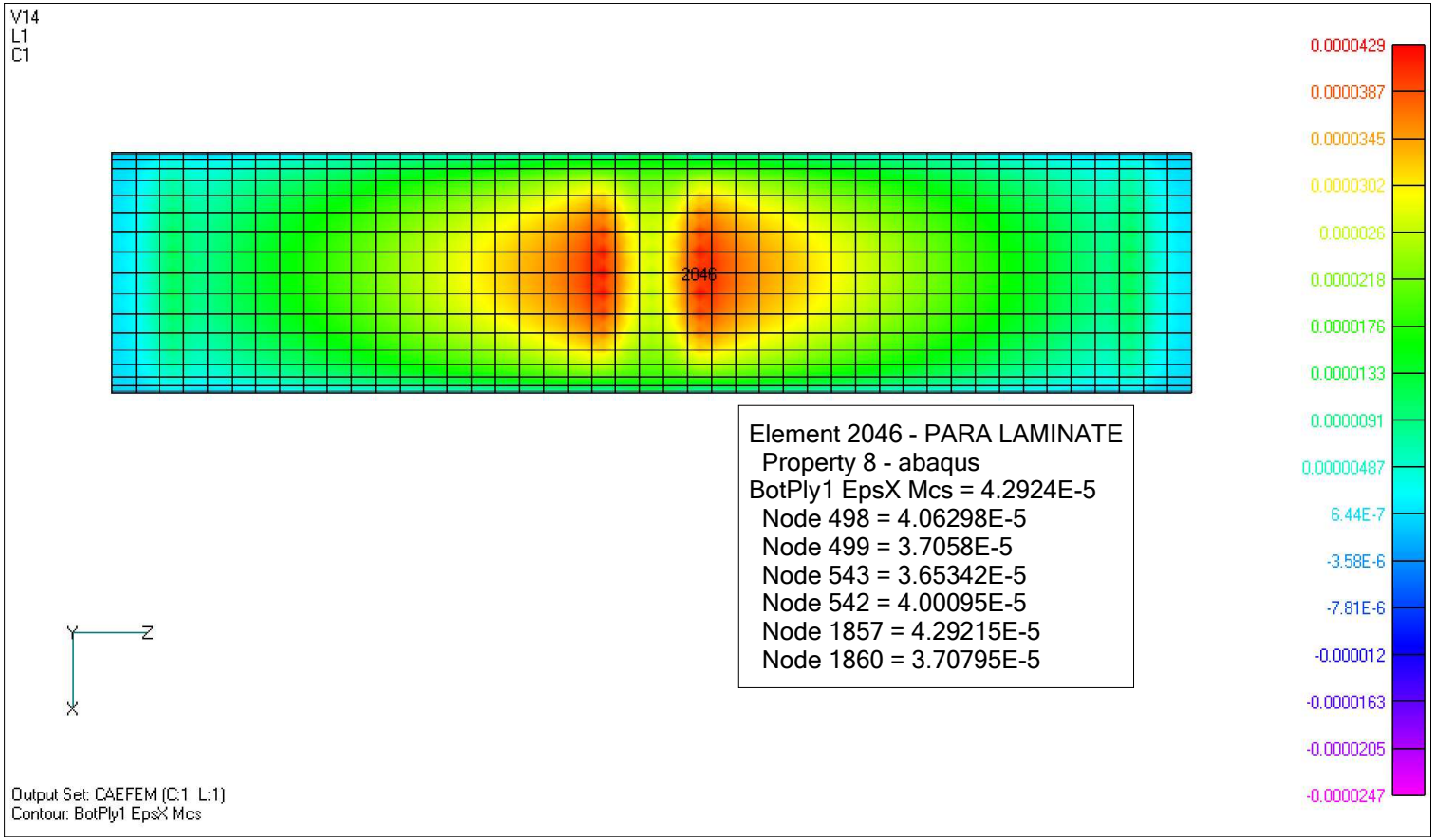

Fig. 79. Maximum strain ϵ_x ply 1 $[0/90]_4$

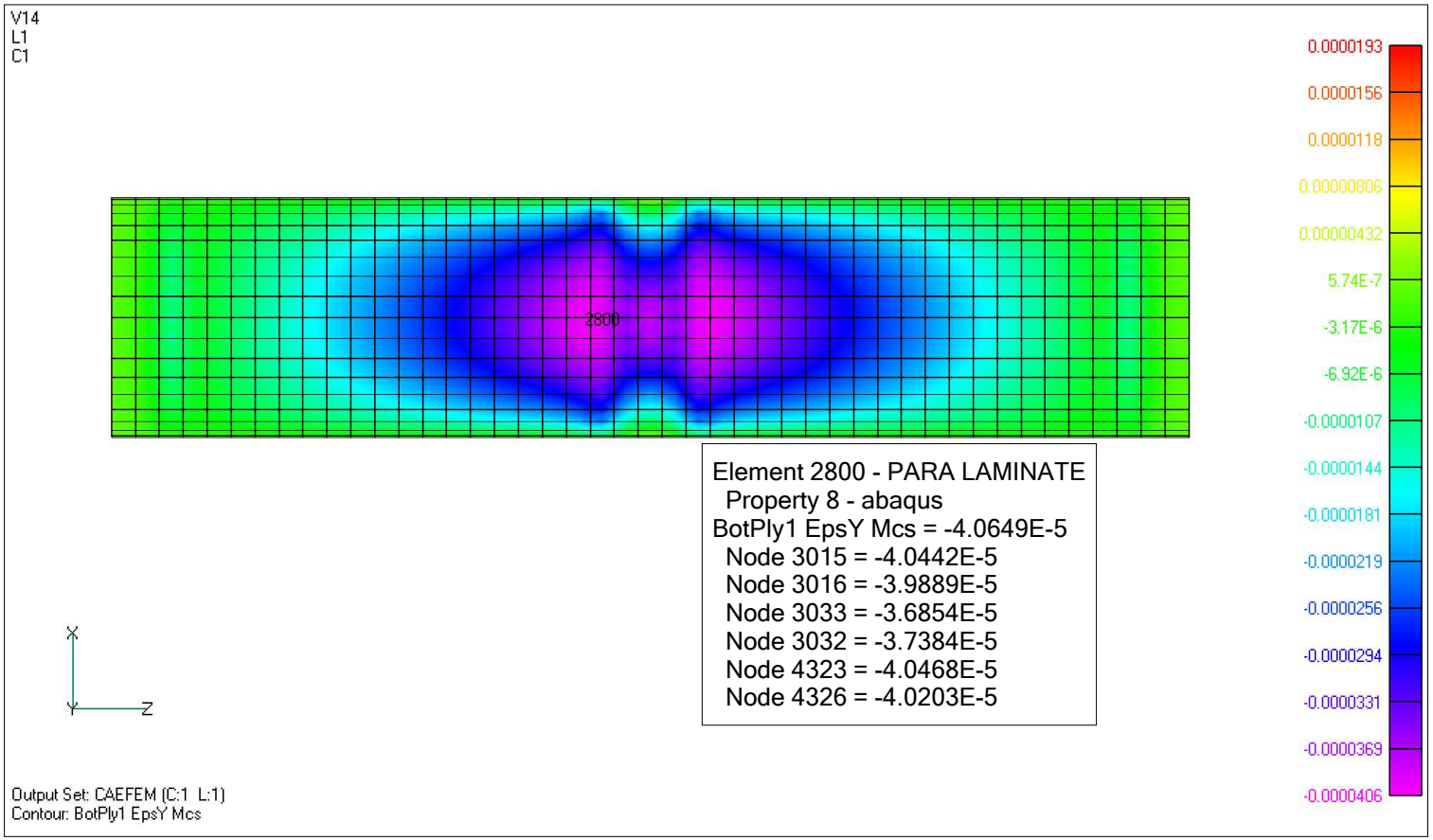

Fig. 80. Maximum strain ϵ_y ply 1 $[0/90]_4$

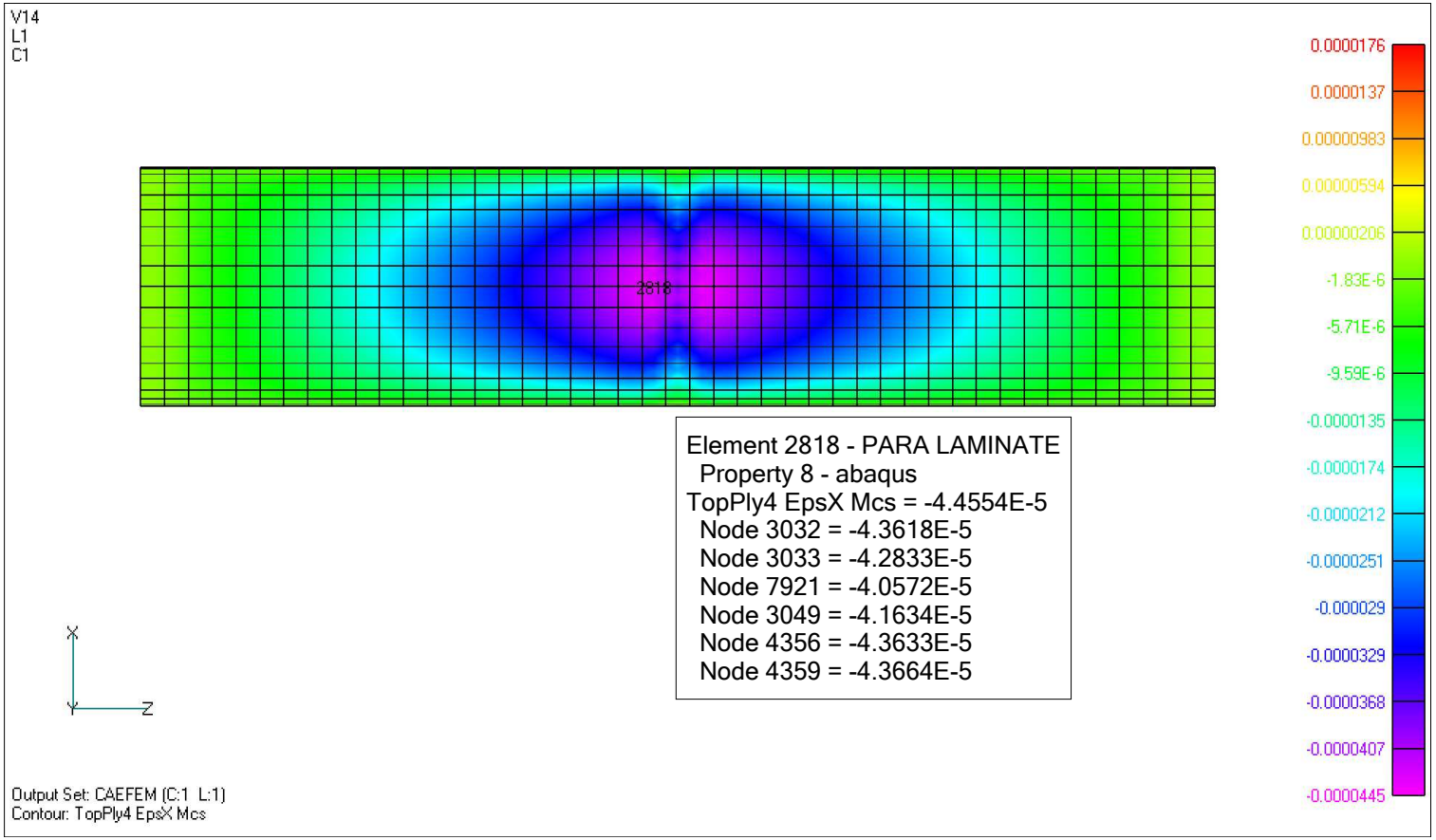

Fig. 81. Maximum strain ϵ_x ply 4 $[0/90]_4$

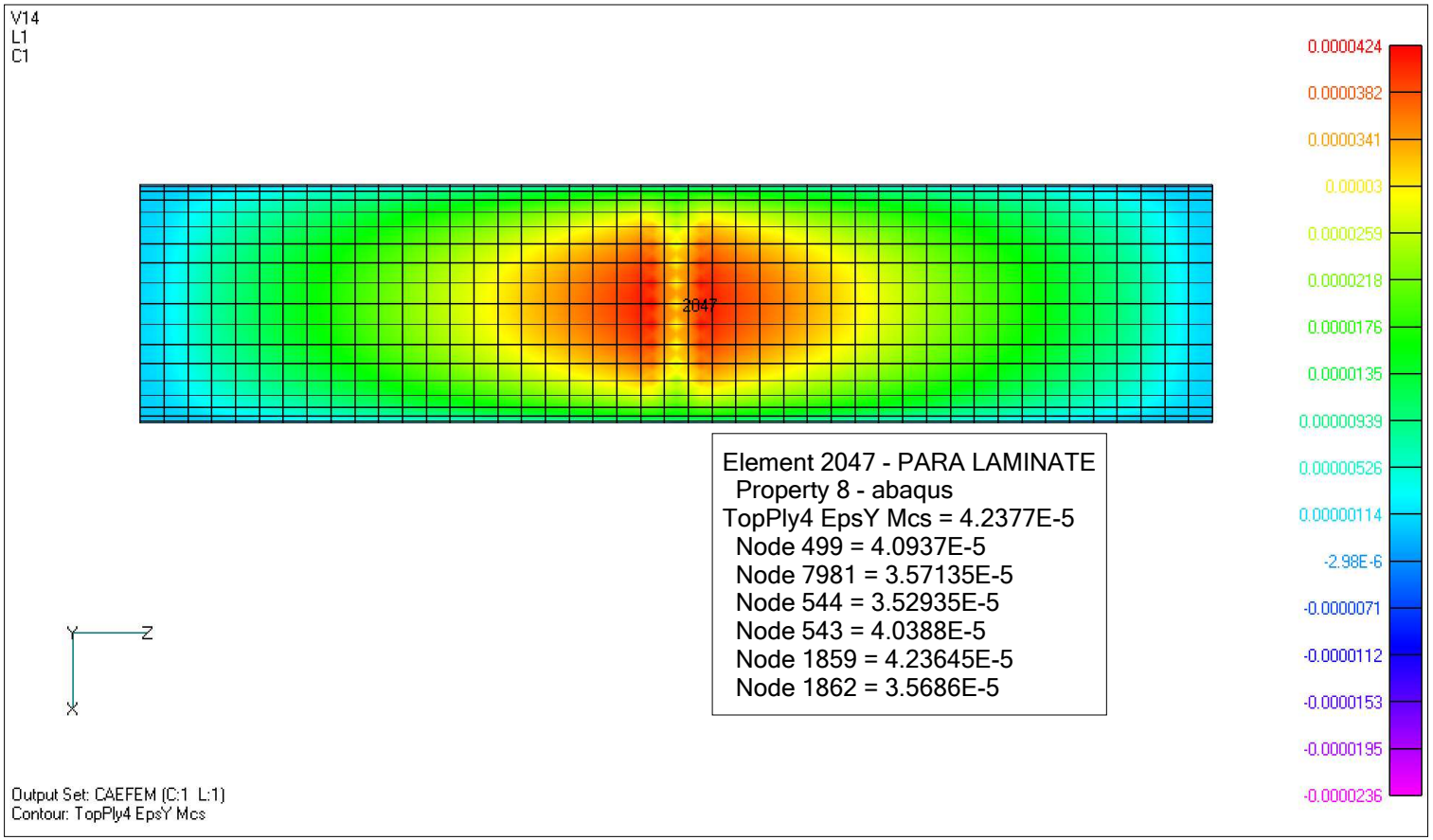

Fig. 82. Maximum strain ϵ_y ply 4 $[0/90]_4$

APPENDIX B

DETAIL DRAWINGS

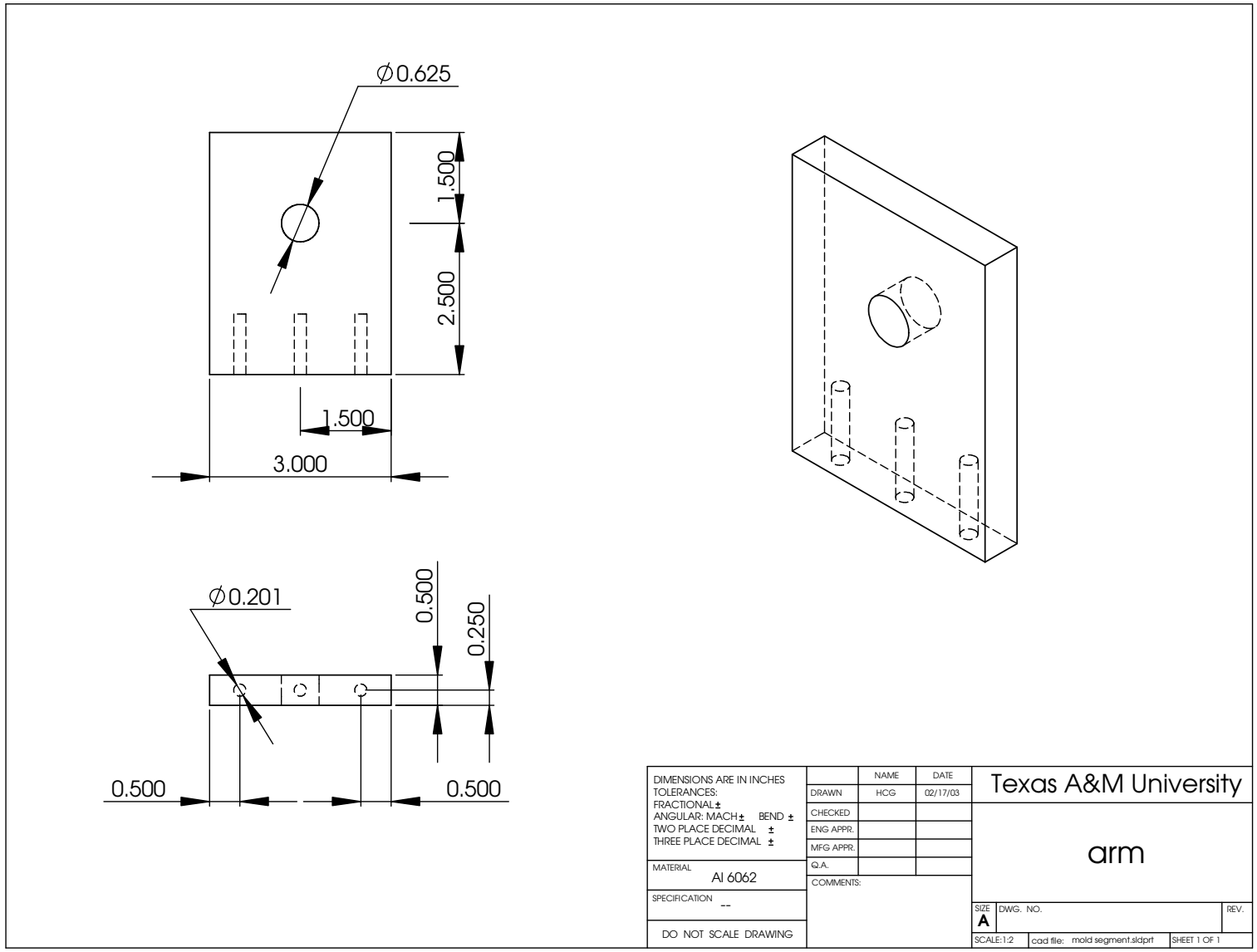

Fig. 83. Arm fixture

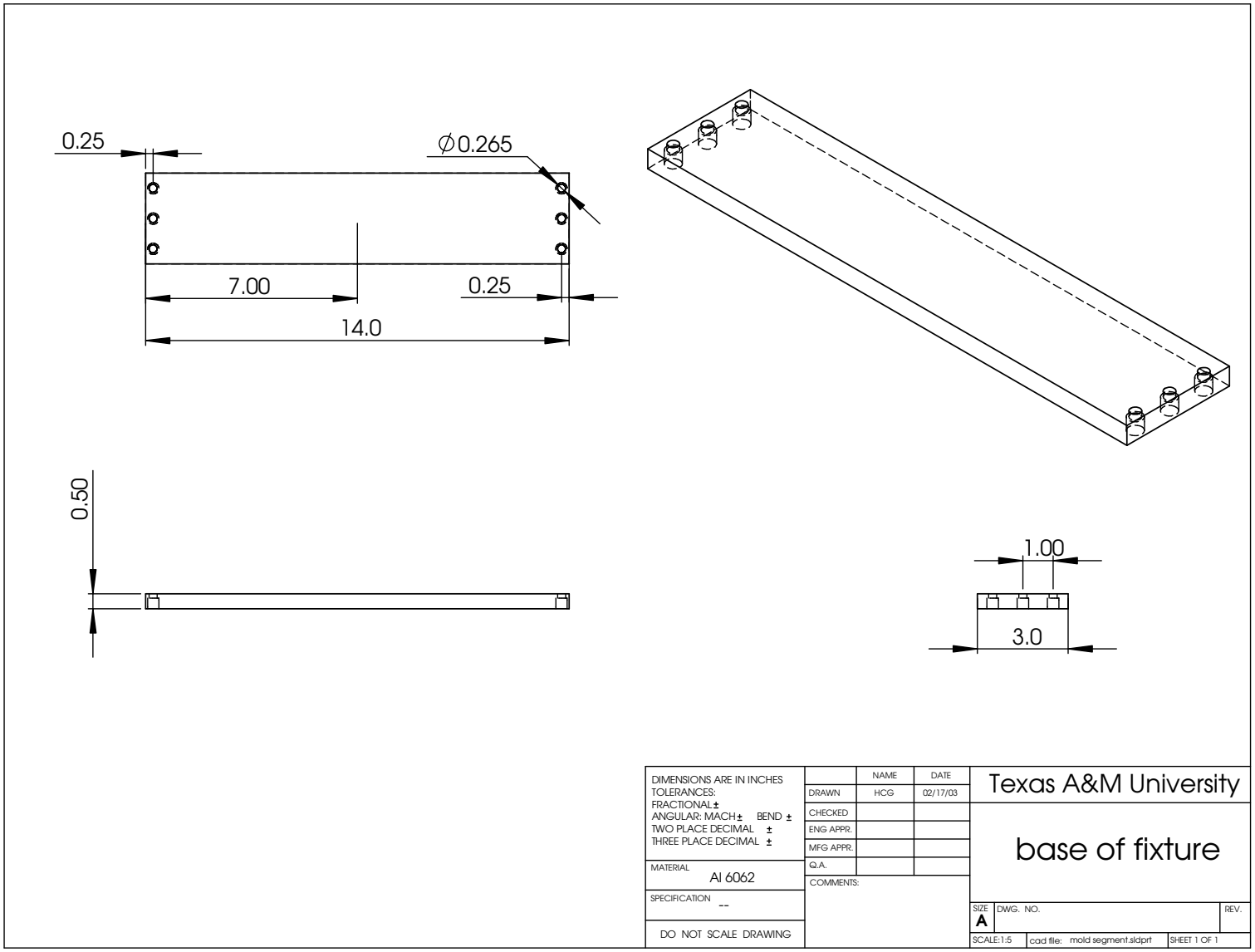

Fig. 84. Base of fixture

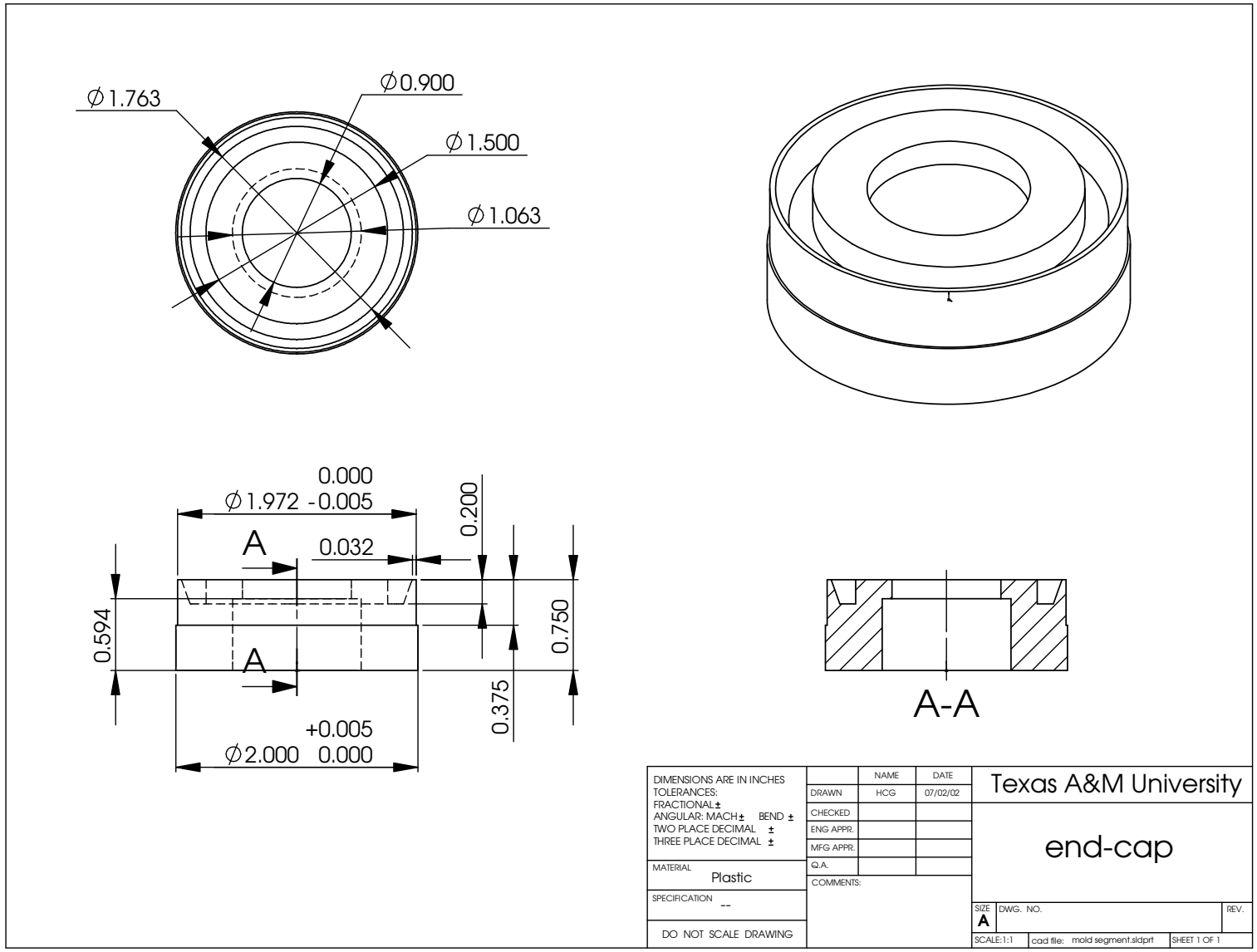

Fig. 85. End cap

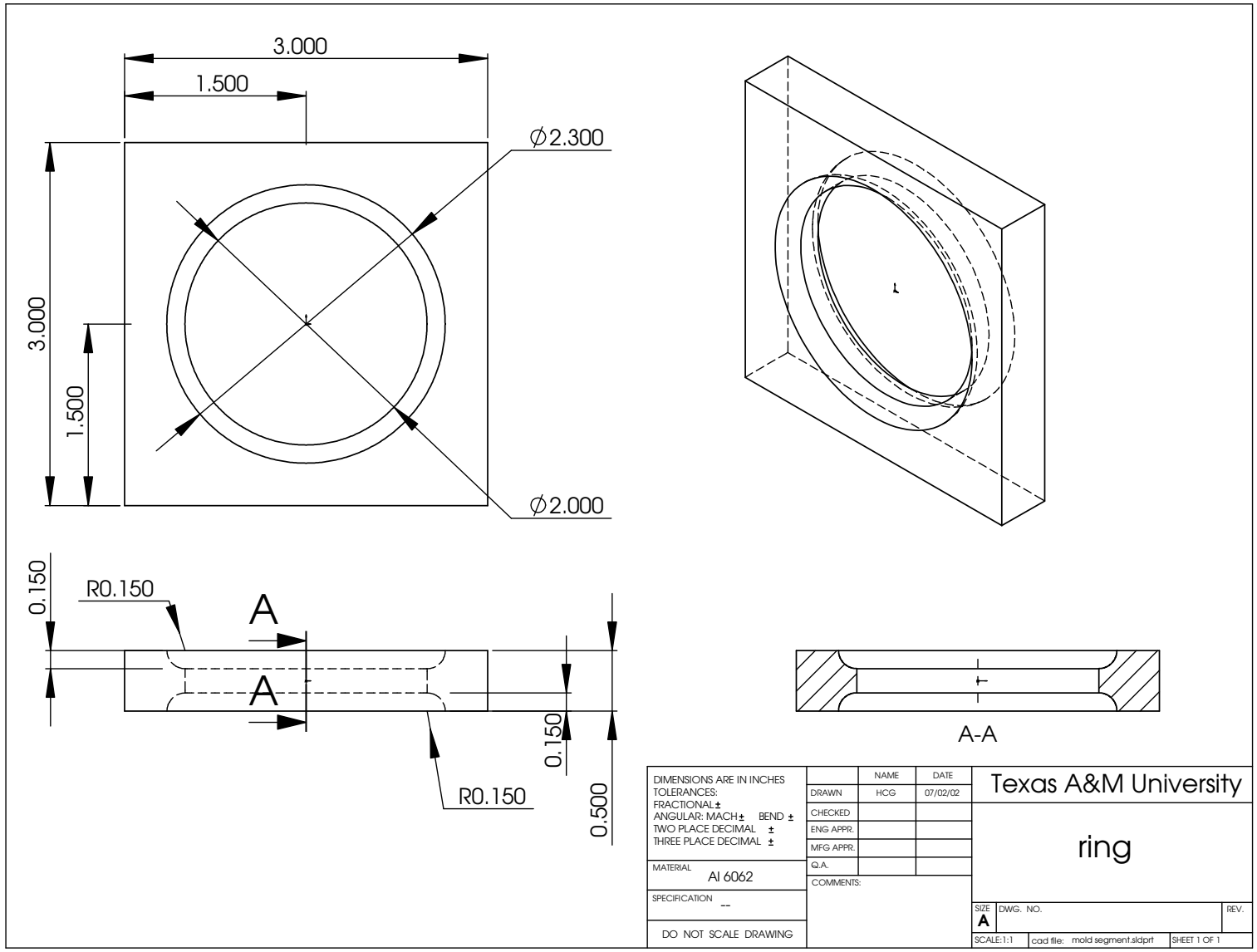

Fig. 86. Loading ring

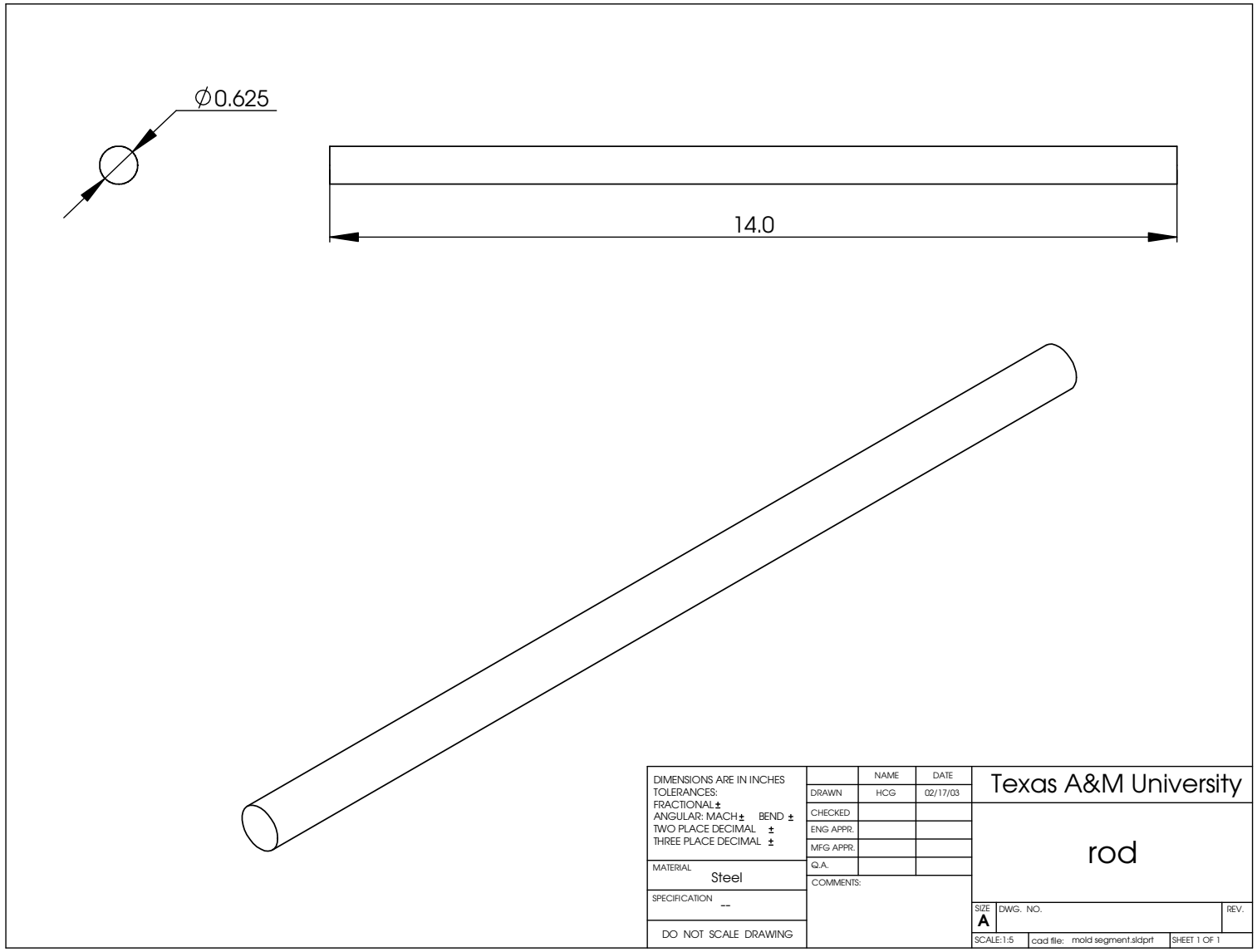
∅0.625
14.0
DIMENSIONS ARE IN INCHES
TOLERANCES:
FRACTIONAL ±
ANGULAR: MACH ± BEND ±
TWO PLACE DECIMAL ±
THREE PLACE DECIMAL ±
MATERIAL
Steel
SPECIFICATION --
DO NOT SCALE DRAWING
NAME
DATE
DRAWN
HCG
02/17/03
CHECKED
ENG APPR.
MFG APPR.
Q.A.
COMMENTS:
Texas A&M University
rod
SIZE
A
DWG. NO.
REV.
SCALE:1:5
cad file: mold segment.sldprt
SHEET 1 OF 1

Fig. 87. Rod

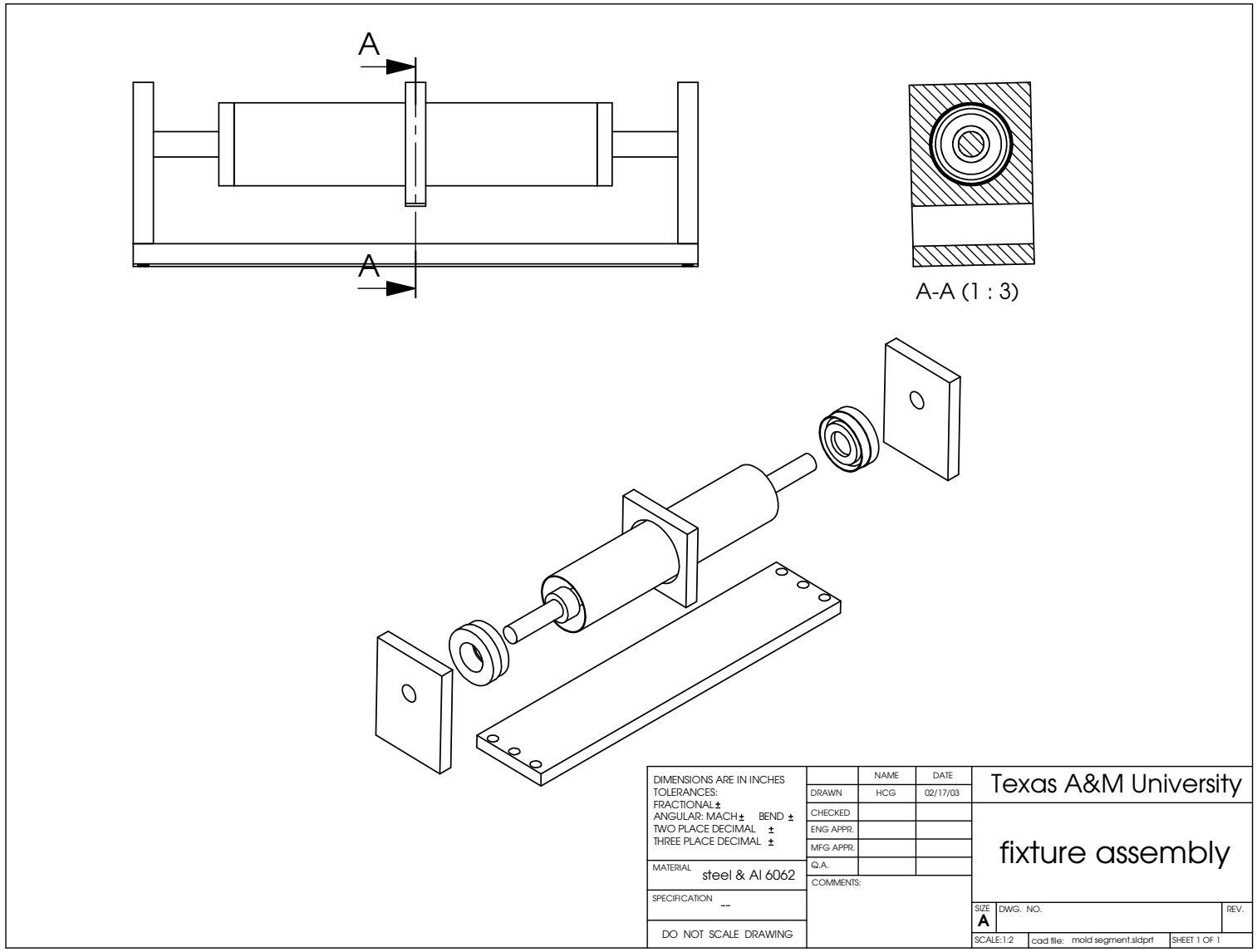

Fig. 88. Fixture assembly

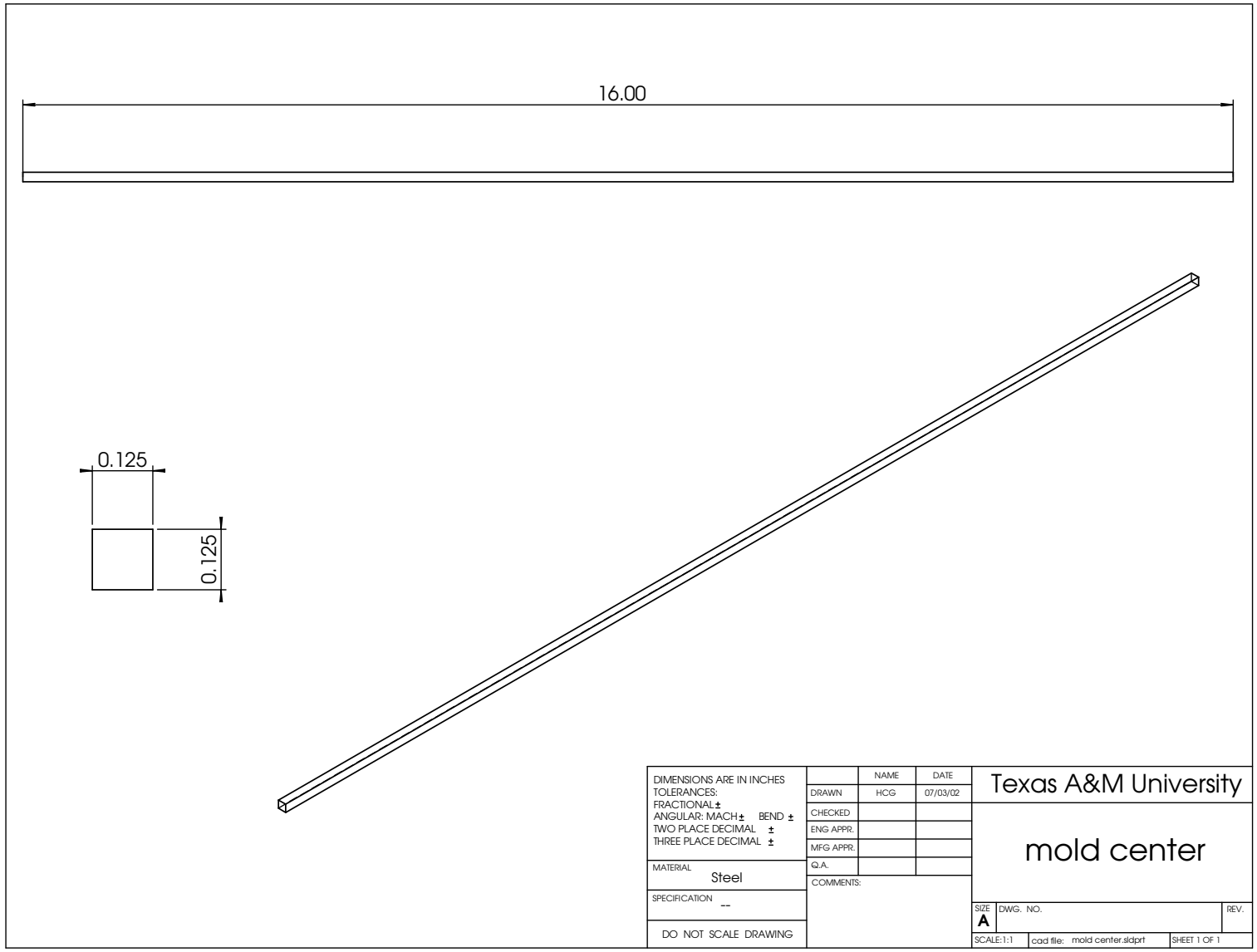

Fig. 89. Mold center

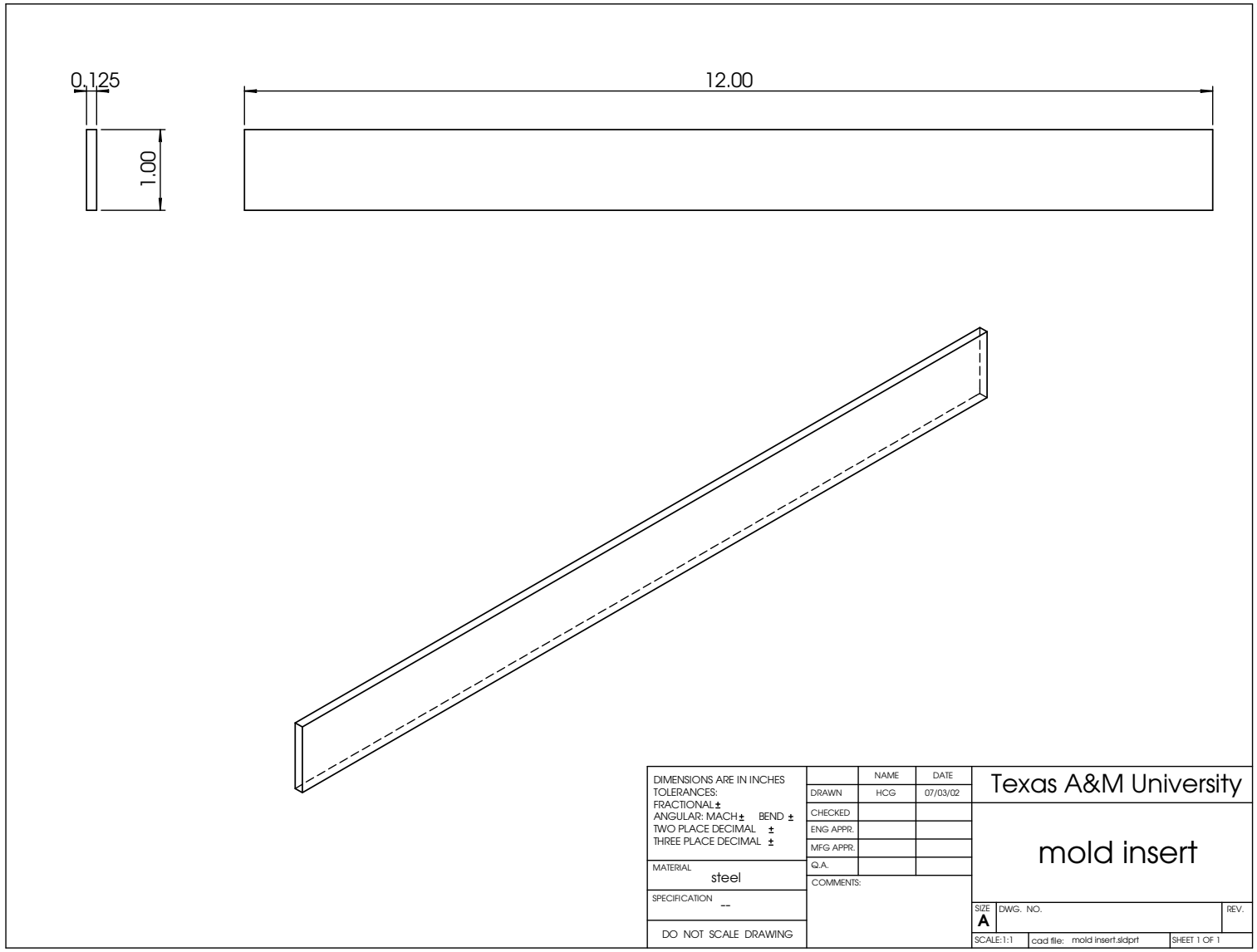

Fig. 90. Mold insert

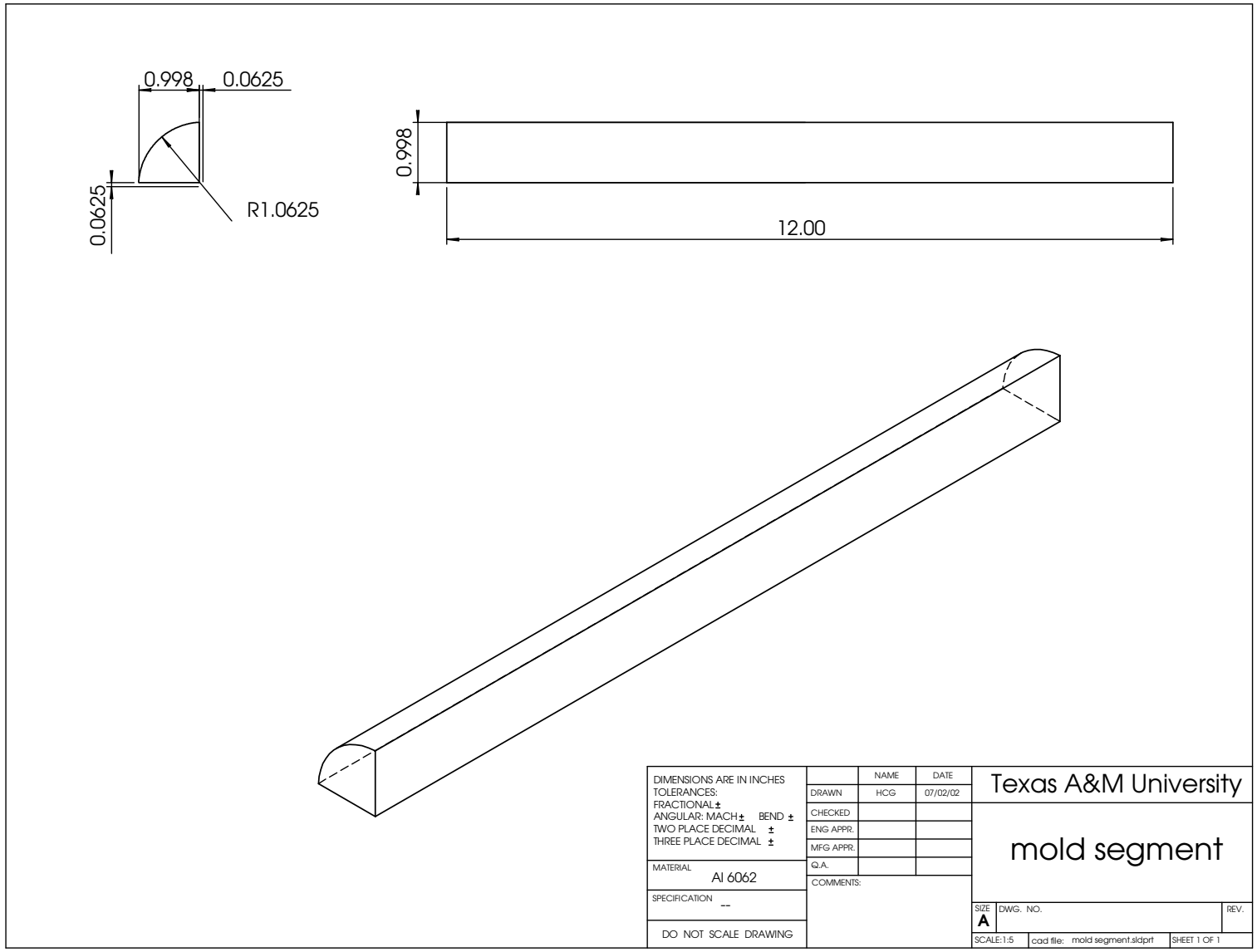

Fig. 91. Mold segment

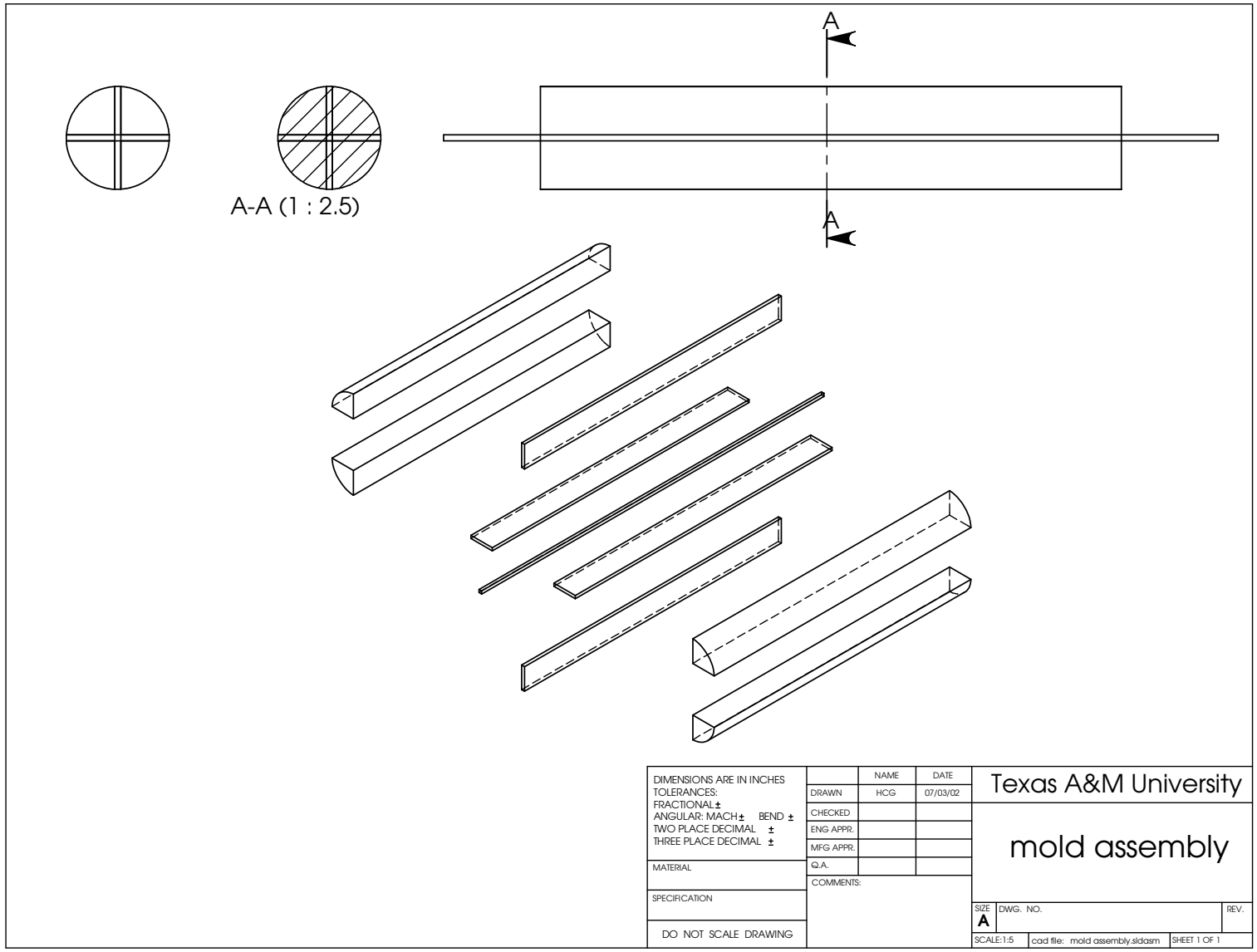

Fig. 92. Mold assembly

APPENDIX C

EXPERIMENT RAW DATA

MTS793	Time:	179.41626	Sec
Data Acquisition			
Time	Axial 1 Displacement	Axial 1 Strain	Axial 1 Force
Sec	in	in/in	N
1.0222168	-0.000155584	-0.000216586	0.12812579
2.0222168	-0.000227849	-0.000109162	-0.095695011
3.0222168	-0.000212114	-0.000128831	-1.1053841
4.0222168	-0.000203662	5.77E-05	-1.2428765
5.0222168	-0.000244517	-3.68E-05	-1.1903708
6.0222168	-0.000359205	-0.000254224	-1.7551488
7.0222168	-0.000303659	0.000184729	-2.4564614
8.0222168	-0.000313115	-5.20E-05	-2.640686
9.0222168	-0.000471247	0.000195465	-3.741667
10.022217	-0.000343633	-0.000136433	-4.4419937
11.022217	-0.000454415	-0.000157721	-5.3149228
12.022217	-0.000544042	-0.000138646	-5.9245629
13.022217	-0.000585369	4.09E-05	-6.2440071
14.022217	-0.000617014	-0.000204395	-7.5652018
15.022217	-0.000625425	-0.000390067	-8.6732197
16.022217	-0.000726966	-0.000318663	-8.7662134
17.022217	-0.000650534	5.26E-05	-7.8032727
18.022217	-0.000660246	-0.000496897	-9.2141342
19.022217	-0.000660379	-0.000128114	-9.9416142
20.022217	-0.00068598	-0.000298788	-9.8702183
21.022217	-0.000913765	-0.000306144	-11.987324
22.022217	-0.00078409	-3.57E-05	-12.685901
23.022217	-0.00095961	-0.000248877	-13.801992
24.022217	-0.000882775	-0.000183148	-14.557933
25.022217	-0.000853445	-0.000172043	-14.821318
26.022217	-0.000955768	-0.000253405	-16.343807
27.022217	-0.001070217	-7.02E-05	-18.12952
28.022217	-0.001070289	-0.000181591	-16.810936
29.022217	-0.001000588	-0.000296186	-17.714876
30.022217	-0.001104557	-0.000308725	-17.649422
31.022217	-0.00109464	-0.000420494	-19.91313
32.022217	-0.001119934	-0.000368246	-20.820217
33.022217	-0.001164273	-0.000162474	-21.557068
34.022217	-0.001241278	-0.00025238	-23.199358
35.022217	-0.001167285	-0.000157618	-25.498487
36.022217	-0.001239598	-0.000338271	-25.124928
37.022217	-0.001310214	-0.000285757	-25.551239
38.022217	-0.00139141	-9.29E-05	-26.332333
39.022217	-0.0014199	-0.000257728	-27.436371
40.022217	-0.001497871	-0.000195933	-28.91564

Fig. 93. Raw data reduction

APPENDIX D

STATISTICAL ANALYSIS

Table XXIV. The t Distribution

d.f.	$t_{.100}$	$t_{.050}$	$t_{.025}$	$t_{.010}$	$t_{.005}$
1	3.078	6.314	12.706	31.821	63.657
2	1.886	2.920	4.303	6.965	9.925
3	1.638	2.353	3.182	4.541	5.841
4	1.533	2.132	2.776	3.747	4.604
5	1.476	2.015	2.571	3.365	4.032
6	1.440	1.943	2.447	3.143	3.707
7	1.415	1.895	2.365	2.998	3.499
8	1.397	1.860	2.306	2.896	3.355
9	1.383	1.833	2.262	2.821	3.250
10	1.372	1.812	2.228	2.764	3.169
11	1.363	1.796	2.201	2.718	3.106
12	1.356	1.782	2.179	2.681	3.055
13	1.350	1.771	2.160	2.650	3.012
14	1.345	1.761	2.145	2.624	2.977
15	1.341	1.753	2.131	2.602	2.947
16	1.337	1.746	2.120	2.583	2.921
17	1.333	1.740	2.110	2.567	2.898
18	1.330	1.734	2.101	2.552	2.878
19	1.328	1.729	2.093	2.539	2.861
20	1.325	1.725	2.086	2.528	2.845
21	1.323	1.721	2.080	2.518	2.831
22	1.321	1.717	2.074	2.508	2.819
23	1.319	1.714	2.069	2.500	2.807

Table XXIV. (continued)

d.f.	$t_{.100}$	$t_{.050}$	$t_{.025}$	$t_{.010}$	$t_{.005}$
24	1.318	1.711	2.064	2.492	2.797
25	1.316	1.708	2.060	2.485	2.787
26	1.315	1.706	2.056	2.479	2.779
27	1.314	1.703	2.052	2.473	2.771
28	1.313	1.701	2.048	2.467	2.763
29	1.311	1.699	2.045	2.462	2.756
inf.	1.282	1.645	1.960	2.326	2.576

VITA

Hector Camerino Garcia Gonzalez is the son of Camerino Garcia Ortiz and Lidia Gonzalez B. Hector attended Instituto Politecnico Nacional (IPN) in Mexico City where he majored in aeronautical engineering. He graduated from IPN in October 2000. Upon completing his bachelor of science degree, Hector applied and was accepted to the Aerospace Engineering Program at Texas A&M University and worked on his thesis under the direction of Dr. Thomas C. Pollock. He found the structural analysis of composites to be an interesting field of study. Hector will continue with his education at Texas A&M University in the doctorate program in aerospace engineering.

The typist for this thesis was Hector C. Garcia Gonzalez..